Since 1955

Strojniški vestnik
Journal of Mechanical Engineering

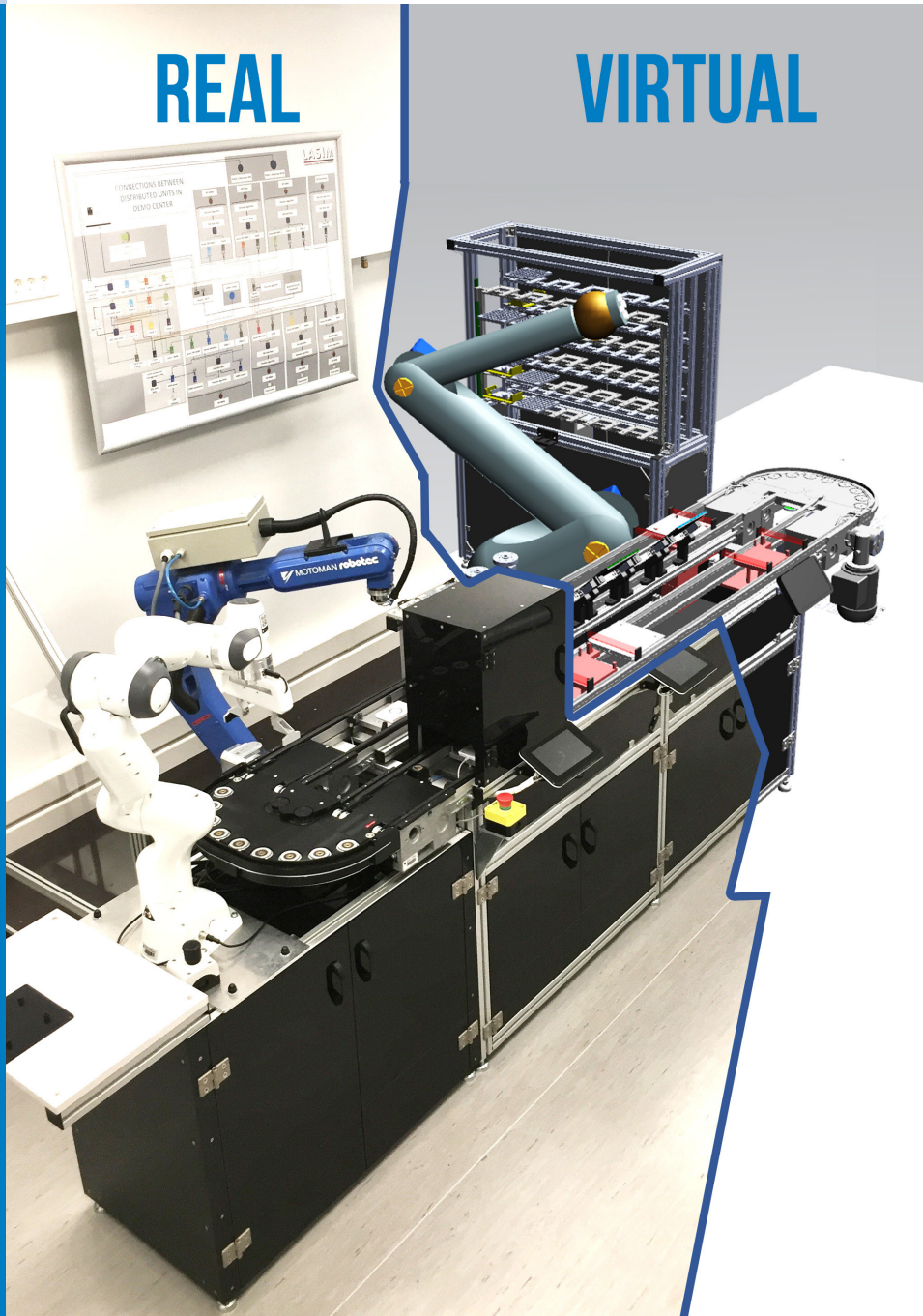

no. 6
year 2019
volume 65

Strojniški vestnik – Journal of Mechanical Engineering (SV-JME)

Aim and Scope

The international journal publishes original and (mini)review articles covering the concepts of materials science, mechanics, kinematics, thermodynamics, energy and environment, mechatronics and robotics, fluid mechanics, tribology, cybernetics, industrial engineering and structural analysis.

The journal follows new trends and progress proven practice in the mechanical engineering and also in the closely related sciences as are electrical, civil and process engineering, medicine, microbiology, ecology, agriculture, transport systems, aviation, and others, thus creating a unique forum for interdisciplinary or multidisciplinary dialogue.

The international conferences selected papers are welcome for publishing as a special issue of SV-JME with invited co-editor(s).

Editorial Office

University of Ljubljana, Faculty of Mechanical Engineering

SV-JME, Aškerčeva 6, SI-1000 Ljubljana, Slovenia

Phone: 386 (0)1 4771 137

Fax: 386 (0)1 2518 567

info@sv-jme.eu, http://www.sv-jme.eu

Print: Papirografika, printed in 300 copies

Founders and Publishers

University of Ljubljana, Faculty of Mechanical Engineering, Slovenia

University of Maribor, Faculty of Mechanical Engineering, Slovenia

Association of Mechanical Engineers of Slovenia

Chamber of Commerce and Industry of Slovenia, Metal Processing Industry Association

Cover:
Exact digital twin of all processes and logistics with embedded artificial intelligence enables agile real-time automatic control and optimisation of real system. Artificial intelligence is integrated in digital agents for control and optimisation of different distributed tasks. The digital twin is used with Virtual Reality for viewing predicted scenarios and also remote real-time viewing.

Image courtesy:
University of Ljubljana, Faculty of Mechanical Engineering, Laboratory LASIM, Slovenia

General information

Strojniški vestnik – Journal of Mechanical Engineering is published in 11 issues per year (July and August is a double issue).

Institutional prices include print & online access: institutional subscription price and foreign subscription €100,00 (the price of a single issue is €10,00); general public subscription and student subscription €50,00 (the price of a single issue is €5,00). Prices are exclusive of tax. Delivery is included in the price. The recipient is responsible for paying any import duties or taxes. Legal title passes to the customer on dispatch by our distributor. Single issues from current and recent volumes are available at the current single-issue price. To order the journal, please complete the form on our website. For submissions, subscriptions and all other information please visit: *http://www.sv-jme.eu.*

You can advertise on the inner and outer side of the back cover of the journal. The authors of the published papers are invited to send photos or pictures with short explanation for cover content.

We would like to thank the reviewers who have taken part in the peer-review process.

ISSN 0039-2480, ISSN 2536-2948 (online)

The journal is subsidized by Slovenian Research Agency.

Strojniški vestnik - Journal of Mechanical Engineering is available on *https://www.sv-jme.eu*.

Contents

Strojniški vestnik - Journal of Mechanical Engineering
volume 65, (2019), number 6
Ljubljana, June 2019
ISSN 0039-2480

Published monthly

Papers

Strojniški vestnik - Journal of Mechanical Engineering 65(2019)6, 329-342
DOI:10.5545/sv-jme.2019.5980
Original Scientific Paper
Received for review: 2019-01-04
Received revised form: 2019-04-14
Accepted for publication: 2019-05-07

Trajectory Tracking Study of Track Vehicles Based on Model Predictive Control

Lin Zhou – Guoqiang Wang* – Kangkang Sun – Xin Li
Jilin University, School of Mechanical and Aerospace Engineering, China

This paper proposes a model predictive control (MPC) algorithm for trajectory tracking of vehicles. Using MPC can reduce tracking errors and random disturbances in complex environments in time. According to the linear kinematics model of the vehicle, a kinematics trajectory tracking controller and an electromechanical coupling dynamics trajectory tracking controller are designed. The drive system of the electrically driven tracked vehicle is non-linear, and an electromagnetic system and mechanical system interact with each other. Taking the electromechanical coupling characteristics into consideration can ensure the matching of the electromechanical performance and the stability of the system during the trajectory tracking control. To verify the algorithm, kinematic simulations and dynamic simulations are performed. The simulation results show that the algorithm has good tracking ability. In addition, a set of test devices is designed to confirm the performance of the trajectory-tracking control algorithm in a real environment. Vision recognition is used to obtain vehicle deviation, and the Kalman filter is used to reduce signal interference. The result shows that the algorithm can meet trajectory tracking requirements.
Keywords: model predictive control, trajectory tracking, tracked vehicle, electromechanical coupling

Highlights
- *A kinematics model, a dynamic model, and an electromechanical coupling model of the tracked vehicle are established.*
- *The control system in trajectory tracking is designed based on model predictive control.*
- *The electromechanical coupling characteristic is added to the trajectory tracking control.*
- *The simulation and vehicle experiment results further validate the control algorithm.*

0 INTRODUCTION

A track vehicle has good passing ability, low grounding pressure, and high adhesion to the ground. It can work in harsh environments, such as soft land and wetlands. Especially in dangerous or narrow situations, a crawler travel mechanism is often used, such as mine-sweeping robots, fire-fighting robots, and deep-sea mining robots [1] and [2]. Automatic navigation or trajectory-tracking technology for track vehicles is necessary for these vehicles. [3] and [4] The automatic movement of the vehicle mainly refers to automatic control the vehicle to reach the designated target, according to the predetermined reference trajectory and the state of the vehicle and the environmental information [5]. Furthermore, trajectory tracking requires the controlled object to reach the specified reference point within a given time [6]. Vehicle mathematical model analysis plays a key role in solving the trajectory tracking control problem of unmanned track vehicles. However, track vehicles are complex nonlinear systems, and it is difficult to establish accurate mathematical models. At the same time, high-precision control problems need to consider many uncertain factors, which can lead to a high complexity of control problems.

Relevant scholars have used different control strategies to explore the trajectory tracking of unmanned track vehicles. Yeu et al. use a modified proportional-differential controller for the path tracking of soft road track vehicles [7]. Zou et al. use a backstepping method based on a modified proportional–integral–derivative (PID) computed-torque control for unmanned track vehicle tracking on hard ground [8]. Huang et al. use a PI path-tracking controller based on look-ahead point information for a differential-drive crawler-type robot [9]. Chen et al. [10] and Li et al. [11] use adaptive sliding mode control theory to control wheeled vehicles. Other scholars also have used other methods, such as fuzzy logic-based controllers [12], adaptive neural-fuzzy inference controllers [13] and slip-compensating control strategies [14]. In the methods commonly used for trajectory tracking control, PID control has poor control effect on nonlinear systems and structurally uncertain systems due to fixed control parameters. Optimal control and pure tracking control depend on specific mathematical models. Fuzzy control does not need to establish an accurate mathematical model, so it is suitable for nonlinear time-varying systems, but the choice of fuzzy rules is not systematic, and it is difficult to adjust online.

Model predictive control (MPC) is based on the system using rolling optimization techniques to solve constrained real-time problems. Predictive control has clear basic ideas and strong development

*Corr. Author's Address: Jilin University, School of Mechanical and Aerospace Engineering, China, linzhou17@mails.jlu.edu.cn

capabilities. It can be combined with various system models, control theory and optimization algorithms to form various control algorithms. MPC can overcome tracking errors and random disturbances in complex environments, and eliminate the uncertainty caused by model mismatch and external disturbances in time; it is also suitable for systems in which mathematical models are inaccurate and have constraints. Consequently, MPC is widely used in the motion control of smart cars, drones and mobile robots [15] and [16]. Shen et al. performed trajectory tracking control of autonomous underwater vehicle using Lyapunov-based model predictive control [17]. Falcone et al. applied MPC to an active front steering system in an autonomous vehicle [18]. Based on the vehicle dynamics model, Lee et al. [19] and Kim et al. [20] applied the MPC method to laterally control a vehicle and achieved good control results. Researchers studied the trajectory control method of a tractor-trailer system based on MPC, and the tests proved that the control method is effective [21] and [22]. Therefore, applying the model predictive control method to the electric drive track vehicles can achieve good control effects, but at this stage there is less research in this direction.

The electromechanical coupling system of the electrically driven track vehicle consists of an alternating current motor and a working machine. The electromagnetic system and the mechanical system interact with each other and form a complex nonlinear system. When the electromechanical performance is not suitable, the induction motor is likely to be blocked and cannot drive the crawler device. In severe cases, it may even burn out the motor [23]. Therefore, it is necessary to perform electromechanical coupling dynamics analysis when analysing and controlling a track vehicle. In the current research, many scholars have established kinematic and dynamic models of track vehicles and applied them to motion analysis [24] and [25]. However, there are few studies combining vehicle trajectory tracking control with electromechanical coupling dynamic analysis.

This paper establishes the kinematic model, the dynamic model, and the electromechanical coupling dynamic model of track vehicles. According to the kinematics model, it designs a trajectory tracking algorithm based on the model predictive control. In the simulation environment, the kinematics model and the electromechanical coupling dynamics model are tested under two conditions to verify the correctness of the control algorithm. To verify the effectiveness of the algorithm under real conditions, physical prototype tests of the track vehicle based on monocular vision and Kalman filter under different initial conditions are performed.

1 ELECTROMECHANICAL COUPLING MODEL OF A TRACK VEHICLE

1.1 Kinematics Model

When the track is steering in a plane without any slippage, as shown in Fig. 1, according to the triangular relationship:

$$\frac{v_R}{R \pm \frac{B}{2}} = \frac{v_L}{R \mp \frac{B}{2}}, \tag{1}$$

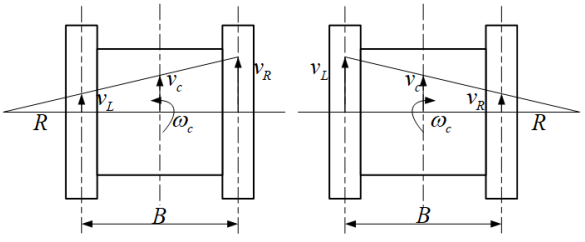

Fig. 1. *Track steering schematic diagram*

According to Eq. (1), the steering radius, the centre-of-mass velocity, and the steering angular velocity of the track can be obtained:

$$R = \frac{B}{2} \cdot \frac{v_R + v_L}{|v_R - v_L|}, \tag{2}$$

$$\mathrm{v}_c = \frac{v_R + v_L}{2}, \tag{3}$$

$$\omega_c = \frac{\mathrm{v}_c}{R} = \frac{v_R - v_L}{B}. \tag{4}$$

To obtain the plane motion equation of the track vehicle, the ground coordinate system OXY is established, as shown in Fig. 2.

When v_r or v_l is consistent with the vehicle's heading direction, it takes a positive sign; otherwise, it is negative. According to Fig. 2, the differential equation of motion of the track vehicle is as follows:

$$\begin{cases} \dot{x} = v_c \cdot \cos\varphi = \dfrac{v_R + v_L}{2} \cdot \cos\varphi \\ \dot{y} = v_c \cdot \sin\varphi = \dfrac{v_R + v_L}{2} \cdot \cos\varphi \\ \dot{\varphi} = \omega_c = \dfrac{v_R - v_L}{B} \end{cases}. \tag{5}$$

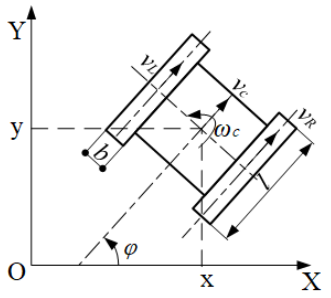

Fig. 2. *Plane motion analysis*

Take $\mathbf{x}=(x,y,z)^T$ as the state vector and $\mathbf{u}=(v_R,v_L)^T$ as the input vector. Eq. (5) can be rewritten as a state equation in matrix form:

$$\begin{bmatrix}\dot{x}\\ \dot{y}\\ \dot{\varphi}\end{bmatrix}=\begin{bmatrix}\frac{1}{2}\cos\varphi & \frac{1}{2}\cos\varphi\\ \frac{1}{2}\sin\varphi & \frac{1}{2}\sin\varphi\\ \frac{1}{B} & -\frac{1}{B}\end{bmatrix}\cdot\begin{bmatrix}v_R\\ v_L\end{bmatrix}. \tag{6}$$

1.2 Dynamic Model

When the track vehicle is moving at low speed in the plane, the external forces include running resistance, steering resistance, and driving force. Since the centrifugal force is negligible at low speed, the analysis of the available force on the track is shown in Fig. 3.

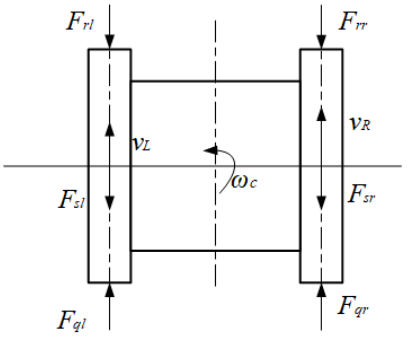

Fig. 3. *Force analysis*

According to the differential equation of rigid body plane motion, the dynamic equation of the track vehicle can be written:

$$\begin{cases}\delta m\dot{v}_c=F_{qr}+F_{ql}-F_{rr}-F_{rl}\\ J_c\dot{\omega}_c=\frac{B}{2}(F_{qr}-F_{ql})-\frac{B}{2}(F_{rr}-F_{rl})-\frac{B}{2}(F_{sr}-F_{sl})\end{cases}. \tag{7}$$

The driving force on both sides can be obtained with Eq. (7):

$$\begin{cases}F_{qr}=\frac{\delta m\dot{v}_C}{2}+\frac{J_C\dot{\omega}_C}{B}+F_{rr}+F_{sr}\\ F_{ql}=\frac{\delta m\dot{v}_C}{2}-\frac{J_C\dot{\omega}_C}{B}+F_{rl}+F_{sl}\end{cases}. \tag{8}$$

The load torque of the motor shafts on both sides can be written:

$$\begin{cases}T_{Lr}=F_{qr}\frac{r}{i\eta}\\ T_{Ll}=F_{ql}\frac{r}{i\eta}\end{cases}. \tag{9}$$

Introduce the motor's general drag equation:

$$J_\omega\dot{\omega}=T_{em}-T_L-f_\omega\omega. \tag{10}$$

Joint Eqs. (7) to (10):

$$\begin{cases}J\dot{\omega}_R=T_{emR}-\frac{r}{i\eta}\left(\frac{\delta m\dot{v}_c}{2}+\frac{J_c\dot{\omega}_c}{B}+F_{rr}+F_{sr}\right)-f_\omega\omega_R\\ J\dot{\omega}_L=T_{emL}-\frac{r}{i\eta}\left(\frac{\delta m\dot{v}_c}{2}-\frac{J_c\dot{\omega}_c}{B}+F_{rl}+F_{sl}\right)-f_\omega\omega_L\end{cases}. \tag{11}$$

Bring Eqs. (3) and (4) into Eq. (11) and calculate:

$$\begin{cases}\dot{\omega}_R=-tf_\omega\omega_R-uf_\omega\omega_L+tT_{emR}-t\frac{r}{i\eta}F_{rr}\\ \qquad -t\frac{r}{i\eta}F_{sr}+uT_{emL}-u\frac{r}{i\eta}F_{rl}-u\frac{r}{i\eta}F_{sl}\\ \dot{\omega}_L=-uf_\omega\omega_R-tf_\omega\omega_L+uT_{emL}-u\frac{r}{i\eta}F_{rr}\\ \qquad -u\frac{r}{i\eta}F_{sr}+tT_{emL}-t\frac{r}{i\eta}F_{rl}-t\frac{r}{i\eta}F_{sl}\end{cases}. \tag{12}$$

The components of t and u in Eq. (12) are expressed as follows:

$$\begin{cases}t=\frac{1}{2}\left(\frac{1}{J+\frac{\delta mr^2}{2i^2}}+\frac{1}{J+\frac{2J_cr^2}{B^2i^2}}\right)\\ u=\frac{1}{2}\left(\frac{1}{J+\frac{\delta mr^2}{2i^2}}-\frac{1}{J+\frac{2J_cr^2}{B^2i^2}}\right)\end{cases}. \tag{13}$$

Take $\mathbf{x}=(\omega_R,\omega_L,x,y,\varphi)^T$ as the state vector, $\mathbf{u}=(T_{emR}i/r,F_{rr},F_{sr},T_{emL}i/r,F_{rl},F_{sl})^T$ as the input. Joint Eqs. (6) and (12) can obtain the complete dynamics equation, and the writing matrix form is as follows:

$$\dot{\mathbf{x}}=A_t\mathbf{x}+B_t\mathbf{u}, \tag{14}$$

where

$$A_t=\begin{bmatrix} -tf & -uf & \\ -uf & -tf & \\ \frac{r}{2i}\cos\theta & \frac{r}{2i}\cos\theta & \mathbf{0}_{5\times3} \\ \frac{r}{2i}\sin\theta & \frac{r}{2i}\sin\theta & \\ \frac{r}{Bi} & -\frac{r}{Bi} & \end{bmatrix},$$

$$B_t=\frac{r}{i\eta}\begin{bmatrix} t & -t & -t & u & -u & -u \\ u & -u & -u & t & -t & -t \\ & & & \mathbf{0}_{3\times5} & & \end{bmatrix}. \quad (15)$$

1.3 Electromechanical Coupling Model

To establish the electromechanical coupling model of the track vehicle, a basic dynamic equation of the motor should first be obtained. Take the current, the rotor angle, and the rotor mechanical angular velocity as state variables, and taking the applied voltage of the winding and the load torque on the shaft as the input vector, which are $\mathbf{x}=(\mathbf{i},\omega_m,\theta)^T$ and $\mathbf{v}=(\mathbf{u},T_L)^T$. The equation for the induction motor in the ABC coordinate system is:

$$\begin{cases} \dfrac{d\mathbf{i}}{dt}=-\mathbf{L}^{-1}\left(\mathbf{R}+\dfrac{\partial\mathbf{L}}{\partial\theta}\dot{\theta}\right)\mathbf{i}+\mathbf{L}^{-1}\mathbf{u} \\ \dfrac{d\omega_m}{dt}=\dfrac{p_0}{2J}\mathbf{i}^T\dfrac{\partial\mathbf{L}}{\partial\theta}\mathbf{i}-\dfrac{f_\omega}{J}\omega_m-\dfrac{T_L}{J}. \\ \dfrac{d\theta}{dt}=p_0\omega_m \end{cases} \quad (16)$$

Since the Eq. (16) is a differential equation with time-varying coefficients, the solution is complicated. If a certain degree of decoupling is achieved with coordinate changes, the equation of state can be simplified. The equation of the motor in the $\alpha\beta-dq$ system can be expressed as:

$$\begin{cases} \dfrac{d\mathbf{i}}{dt}=-\mathbf{L}^{-1}\left(\mathbf{R}+\mathbf{G}\dot{\theta}\right)\mathbf{i}+\mathbf{L}^{-1}\mathbf{u} \\ \dfrac{d\omega_m}{dt}=\dfrac{p_0}{J}\mathbf{i}^T\mathbf{G}\mathbf{i}-\dfrac{f_\omega}{J}\omega_m-\dfrac{T_L}{J} \\ \dfrac{d\theta}{dt}=p_0\omega_m \end{cases}. \quad (17)$$

In Eq. (17), both $\mathbf{L}^{-1}$ and $\mathbf{G}$ are constant arrays, which is easy to solve. Combining dynamic Eq. (14) of the track vehicle with Eq. (17), the equation for the electromechanical coupling of the track vehicle can be obtained. Take $\mathbf{x}=(i_{s\alpha R},i_{s\beta R},i_{rdR},i_{rqR},\omega_R,\theta_R,i_{s\alpha L},i_{s\beta L},i_{rdL},i_{rqL},\omega_L,\theta_L,x,y,\varphi)^T$ as the state vector and take $\mathbf{u}=(u_{s\alpha R},u_{s\beta R},u_{rdR},u_{rqR},F_{rr},F_{sr},u_{s\alpha L},u_{s\beta L},u_{rdL},u_{rqL},F_{rl},F_{sl})^T$ as the input vector. The induction motor rotor is always short-circuited, so $u_{rdR}=u_{rqR}=u_{rdL}=u_{rqL}=0$. Then the track vehicle electromechanical coupling equation is as follows:

$$\dot{\mathbf{x}}=A\mathbf{x}+B\mathbf{v}, \quad (18)$$

where

$$A=\begin{bmatrix} -\mathbf{L}^{-1}\left(\mathbf{R}+\mathbf{G}\dot{\theta}_R\right) & \mathbf{0}_{4\times1} & \mathbf{0}_{4\times1} & & \mathbf{0}_{4\times6} & & \\ tp_0\mathbf{i}_R^T\mathbf{G} & -tf_\omega & 0 & up_0\mathbf{i}_L^T\mathbf{G} & -uf_\omega & 0 & \\ \mathbf{0}_{1\times4} & p_0 & 0 & & \mathbf{0}_{1\times6} & & \\ \hline & \mathbf{0}_{4\times6} & & -\mathbf{L}^{-1}\left(\mathbf{R}+\mathbf{G}\dot{\theta}_L\right) & \mathbf{0}_{4\times1} & \mathbf{0}_{4\times1} & \\ up_0\mathbf{i}_R^T & -uf_\omega & 0 & tp_0\mathbf{i}_L^T\mathbf{G} & -tf_\omega & 0 & \mathbf{0}_{15\times3} \\ & \mathbf{0}_{1\times6} & & \mathbf{0}_{1\times4} & p_0 & 0 & \\ \hline & \frac{r}{2i}\mathrm{c}\varphi & & & \frac{r}{2i}\mathrm{c}\varphi & & \\ \mathbf{0}_{3\times4} & \frac{r}{2i}\mathrm{s}\varphi & \mathbf{0}_{3\times1} & \mathbf{0}_{3\times4} & \frac{r}{2i}\mathrm{s}\varphi & \mathbf{0}_{3\times1} & \\ & \frac{r}{Bi} & & & -\frac{r}{Bi} & & \end{bmatrix}, \quad (19)$$

$$B=\begin{bmatrix} \mathbf{L}^{-1} & -t\frac{r}{i\eta} & -t\frac{r}{i\eta} & -u\frac{r}{i\eta} & -u\frac{r}{i\eta} \\ \hline & & & \mathbf{L}^{-1} & \\ \hline & -u\frac{r}{i\eta} & -u\frac{r}{i\eta} & -t\frac{r}{i\eta} & -t\frac{r}{i\eta} \end{bmatrix} \quad (20)$$

2 MODEL PREDICTIVE CONTROL ALGORITHM

The discrete-time state-space model of a linear system can be expressed as:

$$\begin{cases} \mathbf{x}(k+1)=\mathbf{A}\mathbf{x}(k)+\mathbf{B}\mathbf{u}(k) \\ \mathbf{y}(k)=\mathbf{C}\mathbf{x}(k) \end{cases}. \quad (21)$$

If the state $\mathbf{x}$ is measurable and the system is undisturbed, set the prediction time domain to P and the control time domain to M (where $P\geq M$). At the sampling instant k, the system control input is $u(k)$. Let the control variable changes only in the future M steps $k,k+1,\ldots,k+M-1$, and remain unchanged outside the control time domain, then the future P steps $k+1,k+2,\ldots,k+P-1$ are as follow:

$$\mathbf{X}(k+j)=\mathbf{A}_x\mathbf{x}(k)+\mathbf{B}_x\mathbf{U}(k), \quad (22)$$

where:

$$\mathbf{X}(k+j)=\begin{bmatrix}\mathbf{x}(k+1)\\ \vdots\\ \mathbf{x}(k+M)\\ \vdots\\ \mathbf{x}(k+P)\end{bmatrix},\ \mathbf{U}(k)=\begin{bmatrix}\mathbf{u}(k)\\ \mathbf{u}(k+1)\\ \mathbf{u}(k+2)\\ \vdots\\ \mathbf{u}(k+M-1)\end{bmatrix},$$

$$\mathbf{A}_x=\begin{bmatrix}\mathbf{A}\\ \vdots\\ \mathbf{A}^M\\ \vdots\\ \mathbf{A}^P\end{bmatrix},\ \mathbf{B}_x=\begin{bmatrix}\mathbf{B} & 0 & \cdots & 0\\ \vdots & \vdots & \cdots & \vdots\\ \mathbf{A}^{M-1}\mathbf{B} & \mathbf{A}^{M-2}\mathbf{B} & \cdots & \mathbf{B}\\ \vdots & \vdots & \ddots & \vdots\\ \mathbf{A}^{P-1}\mathbf{B} & \mathbf{A}^{P-2}\mathbf{B} & \cdots & \sum_{i=0}^{P-M}\mathbf{A}^i\mathbf{B}\end{bmatrix}. \quad (23)$$

For the track vehicle kinematics model Eq. (6), it can be written as a general form:

$$\dot{\mathbf{x}}=\mathbf{f}(\mathbf{x},\mathbf{u}). \quad (24)$$

Using linear systems can make it easy to check local stability and accelerate the simulation. Since the kinematic model is simple in form, and the coefficient matrix elements are constants, the kinematic model should be linearized. Assuming that the target trajectory is the running trajectory of the reference vehicle, and the state quantity and the control amount of the reference vehicle at any time are given, then the target trajectory can be tracked by the deviation between the controlled vehicle and the reference vehicle. Every point on the target trajectory satisfies Eq. (6):

$$\dot{\mathbf{x}}_r=\mathbf{f}(\mathbf{x}_r,\mathbf{u}_r) \quad (25)$$

In Eq. (25), $\mathbf{x}_r=(x_r,y_r,z_r)^T$ is the reference state variable, and $\mathbf{u}_r=(v_{rr},v_{lr})^T$ is the reference manipulated variable. Expanding the above equation with a Taylor series at the reference track point and only retaining one degree term:

$$\dot{\mathbf{x}}_r=\mathbf{f}(\mathbf{x}_r,\mathbf{u}_r)+\left.\frac{\partial\mathbf{f}(\mathbf{x},\mathbf{u})}{\partial\mathbf{x}}\right|_{\substack{x=x_r\\u=u_r}}(\mathbf{x}-\mathbf{x}_r)+$$

$$+\left.\frac{\partial\mathbf{f}(\mathbf{x},\mathbf{u})}{\partial\mathbf{x}}\right|_{\substack{x=x_r\\u=u_r}}(\mathbf{u}-\mathbf{u}_r). \quad (26)$$

Shortened as:

$$\dot{\mathbf{x}}_r=\mathbf{f}(\mathbf{x}_r,\mathbf{u}_r)+\mathbf{f}_{x,r}(\mathbf{x}-\mathbf{x}_r)+\mathbf{f}_{u,r}(\mathbf{u}-\mathbf{u}_r). \quad (27)$$

In Eq. (27), $\mathbf{f}_{x,r}$ and $\mathbf{f}_{u,r}$ are the Jacobian matrices of $\mathbf{f}$ relative to $\mathbf{x}$ and $\mathbf{u}$, respectively. Subtracting Eq. (24) and Eq. (27), we obtain:

$$\dot{\tilde{\mathbf{x}}}=\mathbf{A}(t)\tilde{\mathbf{x}}+\mathbf{B}(t)\tilde{\mathbf{u}}. \quad (28)$$

In Eq. (28), $\tilde{\mathbf{x}}=\mathbf{x}-\mathbf{x}_r$ and $\tilde{\mathbf{u}}=\mathbf{u}-\mathbf{u}_r$ are deviation vectors; $\mathbf{A}(t)=\mathbf{f}_{x,r}$, $\mathbf{B}(t)=\mathbf{f}_{u,r}$.

The above Eq. (28) is a continuous time system, which needs to be discretized to obtain the general predictive control form as Eq. (21).

Discretize it with the forward difference:

$$\tilde{\mathbf{x}}(k+1)=\mathbf{A}(k)\tilde{\mathbf{x}}(k)+\mathbf{B}(k)\tilde{\mathbf{u}}(k), \quad (29)$$

where,

$$\mathbf{A}(k)=\mathbf{I}+T\mathbf{A}(t)=\begin{bmatrix}1 & 0 & -\frac{1}{2}(v_R+v_L)\sin\varphi\cdot T\\ 0 & 1 & -\frac{1}{2}(v_R+v_L)\cos\varphi\cdot T\\ 0 & 0 & 1\end{bmatrix}, \quad (30)$$

$$\mathbf{B}(k)=T\mathbf{B}(t)=T\begin{bmatrix}\frac{\cos\varphi}{2} & \frac{\cos\varphi}{2}\\ \frac{\sin\varphi}{2} & \frac{\sin\varphi}{2}\\ \frac{1}{B} & -\frac{1}{B}\end{bmatrix}. \quad (31)$$

Predictive control needs to solve an optimization problem in each sampling time, so a performance index function needs to be set in advance. By controlling the amount of optimization, we can obtain the maximum or minimum. The performance index function usually uses a quadratic function, and the normal control objective is to make the output predicted value as close as possible to the target value. The trajectory tracking control involved in this paper belongs to the output optimal control problem, and its performance function can be expressed as:

$$J=\mathbf{X}^T(k+j)\mathbf{Q}\mathbf{X}(k+j)+\mathbf{U}^T(k)R\mathbf{U}(k). \quad (32)$$

State-weighting matrix $\mathbf{Q}$ is a diagonal matrix, $\mathbf{Q}=diag(q_1,q_2,\ldots,q_p)$. Each element q_i represents the importance of tracking errors at different times; control weighting matrix $\mathbf{R}$ is also generally taken as a diagonal matrix. It achieves a certain degree of suppression of the fluctuation of the control variable and improves the stability of the system to some extent.

Since the performance index function is a quadratic function, it can be represented as a quadratic programming problem to solve. Write Eq. (32) as the standard form of quadratic programming:

$$J=\frac{1}{2}\mathbf{U}^T(k)H(k)\mathbf{U}(k)+\mathbf{f}^T(k)\mathbf{U}(k)+d(k),$$

$$\text{s.t.}\quad \mathbf{U}_{\min}(k)\le\mathbf{U}(k)\le\mathbf{U}_{\max}(k), \quad (33)$$

where:

$$H(k)=2(\mathbf{B}^T(k)\mathbf{QB}(k)+\mathbf{R}_x),$$
$$\mathbf{f}(k)=2\mathbf{B}^T(k)\mathbf{QA}(k)\tilde{\mathbf{x}}(k|k),$$
$$d(k)=\tilde{\mathbf{x}}^T(k|k)\mathbf{A}^T(k)\mathbf{QA}(k)\tilde{\mathbf{x}}(k|k). \quad (34)$$

H is a Hessian matrix, symmetrical and positive definite, and describing the quadratic part of the objective function; vector **f** describes the linear part of the objective function; d is an unrelated item to $\mathbf{U}(k)$ and does not affect the optimization result.

Therefore, the optimization control problem can be described as finding a control sequence $\mathbf{U}^*(k)$, so that:

$$\mathbf{U}^*(k)=\arg\min_{U(k)} J. \quad (35)$$

After obtaining the optimal sequence, executing the first control amount:

$$\mathbf{u}(k)=(1,0,\ldots,0)\mathbf{U}^*(k). \quad (36)$$

The optimization shown in Eq. (35) is an unconstrained optimization. The fluctuation of prediction output and the control input can be suppressed to some extent by the weighting matrix **Q** and **R**. However, the control variable cannot be precisely constrained. In the actual process, if the amplitude of the applied control signal or its increment too large, it can cause a significant impact on the system and even affect the stability of the system. Therefore, for Eq. (33), the boundary constraint of the control variable needs to be considered.

$$\begin{cases}\mathbf{U}_{\min}(k)=\mathbf{U}_{\min}-\mathbf{U}_r\\ \mathbf{U}_{\max}(k)=\mathbf{U}_{\max}-\mathbf{U}_r\end{cases}, \quad (37)$$

where $\mathbf{U}_{\min}$ and $\mathbf{U}_{\max}$ are control variable constraints and $\mathbf{U}_r=\left[u_r(k),\ldots,u_r(k+N-1)\right]^T$ is the reference control sequence.

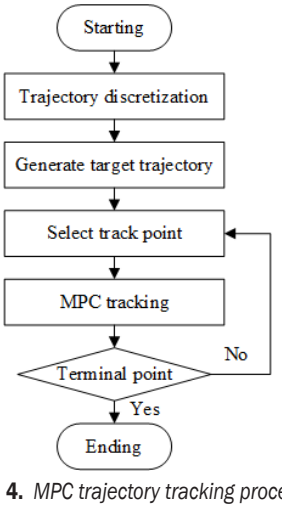

Fig. 4. *MPC trajectory tracking process*

Using the solution algorithm to solve Eq. (33) in each control cycle and obtain a control sequence $\mathbf{U}^*(k)=\left\{u^k(k),u^k(k+1),\ldots,u^k(k+N-1)\right\}$. Applying the first control variable $\mathbf{u}^k(k)$ of the control sequence to the system. Repeat this step to achieve track vehicle trajectory tracking. The process of MPC trajectory tracking control is shown in Fig. 4.

3 NUMERICAL SIMULATION

To verify the performance of the control algorithm, the trajectory tracking ability simulation is carried out under the conditions of kinematics and dynamics.

3.1 Kinematic Trajectory Tracking Simulation

To perform kinematics tracking simulation, this paper established a kinematics model of the vehicle in MATLAB and built a controller in Simulink. At present, the MPC controller is based on the present position and uses the model to simulate several kinds of outputs, and the optimizer finds the optimal one. After obtaining the optimal control sequence, the controller applies the first step to the vehicle. Then, it calculates the position at the next moment using Eq. (6) and uses it as the starting point for the new optimization. It repeats at this process until the control is completed.

3.1.1 Straight Linear Conditions

When the track vehicle is in line tracking, the reference trajectory equation is set to:

$$\begin{cases}x(t)=0.15t\\ y(t)=1\\ \varphi(t)=0\end{cases}. \quad (38)$$

The reference manipulated variable:

$$v_{rr}(t)=v_{rl}(t)=0.15. \quad (39)$$

In the simulation process, the sampling time is $T=1$ s, the prediction time domain is $N=10$, and the simulation time is 50 s. State-weighting matrix $\mathbf{q}_i=diag(1,1,0.1)\times e^{i/10}$, $\mathbf{Q}=diag(q_1,q,...,q_n)$, control-weighting matrix $\mathbf{R}=0.1\mathbf{I}$, the initial condition is $\mathbf{x}=(0,0,0)^T$. Use the quadprog function in MATLAB to solve the quadratic programming problem and selecting "interior point convex" as the optimization method. The simulation results are shown in Fig. 5.

It can be seen from Fig. 5 that the MPC control method enables the vehicle to overcome the influence of the initial deviation when tracking in a straight

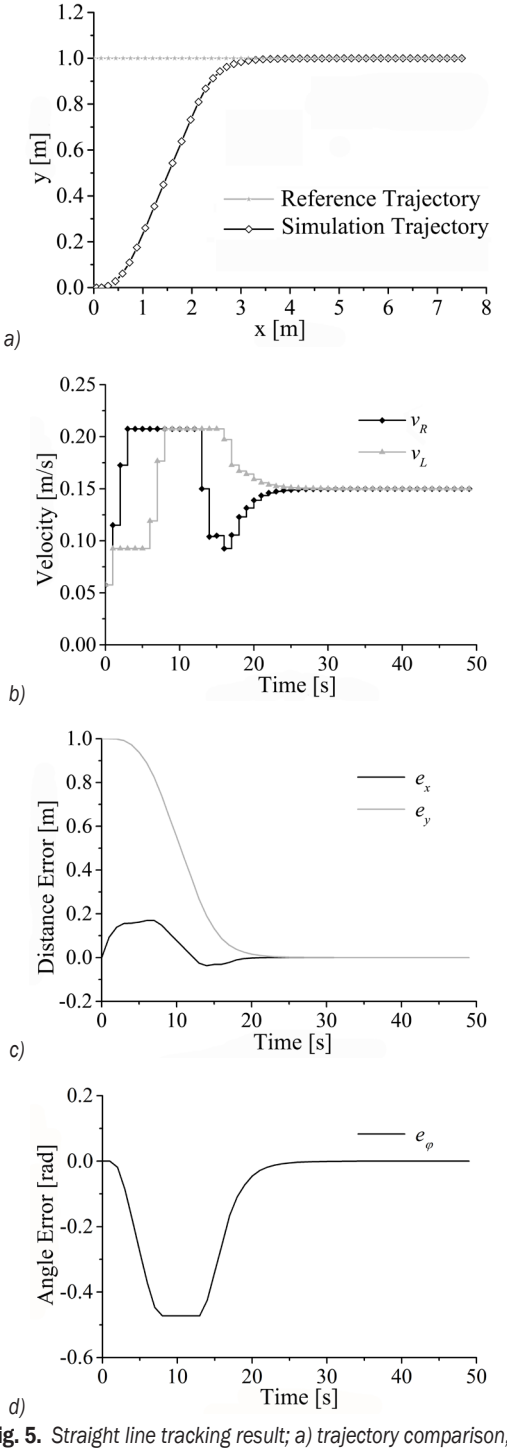

Fig. 5. *Straight line tracking result; a) trajectory comparison, b) velocity fluctuation, c) distance error, and d) angle error*

line, and to achieve accurate tracking in about 25 s, which has a fast convergence speed. After reaching the desired velocity, the vehicle remains stable, the vehicle tracking process is not over-adjusted, and the error remains at zero after tracking.

3.1.2 Spiral Conditions

Assuming that the reference vehicle is travelling at a constant velocity on the target spiral trajectory, the spiral trajectory equation is set to:

$$\begin{cases} s = v_c t \\ x = \int_0^t \cos\dfrac{5\pi}{144} s^2 ds\,. \\ y = \int_0^t \cos\dfrac{5\pi}{144} s^2 ds \end{cases} \tag{40}$$

The reference control variable set as:

$$\begin{cases} c = \dfrac{5\pi}{144} s \\ \omega = v_c c \\ v_r = v_c + \dfrac{\omega B}{2}\,. \\ v_t = v_c - \dfrac{\omega B}{2} \end{cases} \tag{41}$$

In Eq. (41), v_c=0.12 m/s is the reference vehicle's centre-of-mass velocity. The simulation time is 100 s, and the sampling time and the prediction time domain are the same as the line-tracking settings. The simulation results are shown in Fig. 6.

As shown in Fig. 6, the spiral tracking also shows good results. At the beginning of the simulation, there is an angular error of 0.8 rad between the heading of the controlled vehicle and the target heading. With the real-time adjustment of the velocity and heading of the controlled vehicle, the distance error and the angle error are rapidly reduced, and accurate tracking is achieved at 35 s. Although a certain amount of angular overshoot occurs during the tracking process, the overshoot is only about 15 % of the maximum angular error, and the error remains at 0 after accurate tracking.

3.2 Electromechanical Coupling Dynamics Simulation

The complete electromechanical coupling dynamics model is the 15-step nonlinear differential Eq. (20), which requires a numerical method to be solves. To ensure the real-time performance of the system, the prediction model of this section still uses the linear kinematics model. At each sampling instant k, obtain the optimal control sequence $\mathbf{U}^*(k)=\{u(k),u(k+1),...,u(k+n-1)\}$. According to the first item $u(k)$, the left and right motor speed n_{pl}, n_{pr} can be calculated. Calculate the load torque of the two sides of the electric motor according to

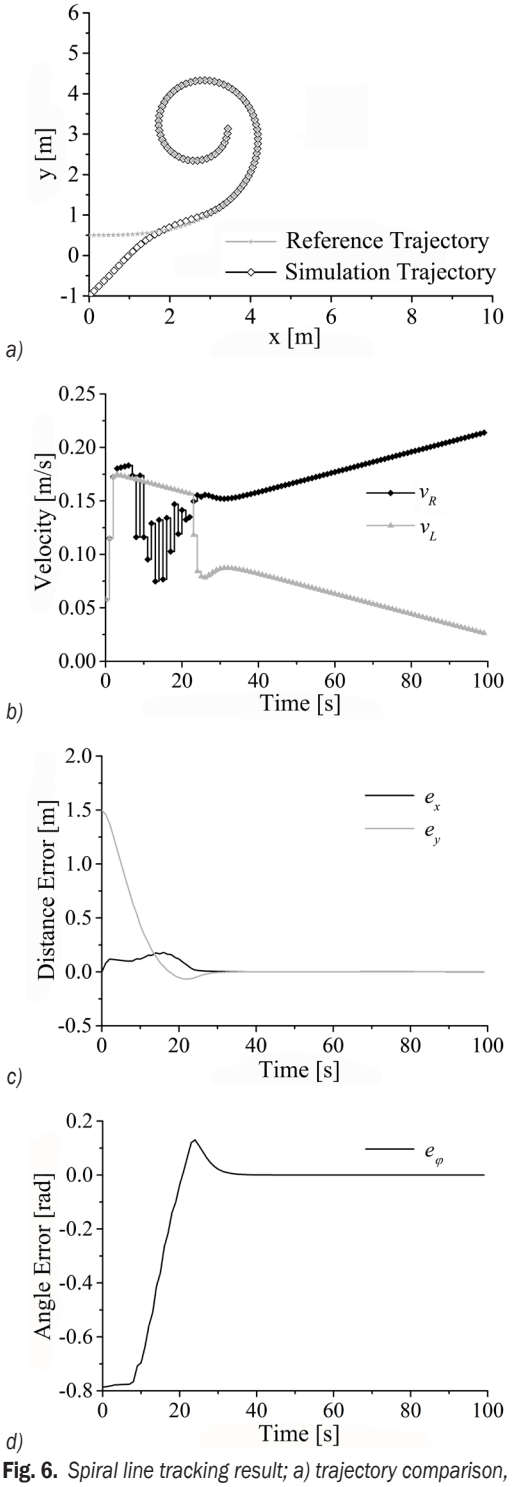

Fig. 6. *Spiral line tracking result; a) trajectory comparison, b) velocity fluctuation, c) distance error, and d) angle error*

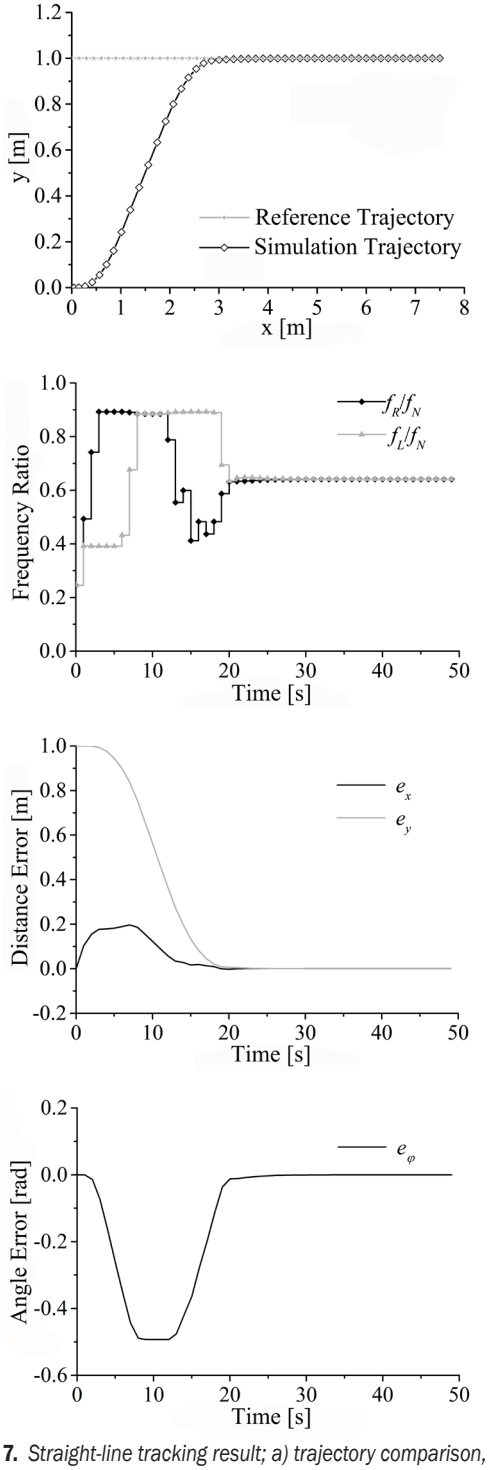

Fig. 7. *Straight-line tracking result; a) trajectory comparison, b) velocity fluctuation, c) distance error, and d) angle error*

the motor speed, and find the voltage and frequency on both sides, taking the voltage and frequency as the current optimal control amount. According to the electromechanical coupling dynamics Eq. (18), calculate the crawler position of the next sampling moment and use it as the next optimization starting point.

In the following straight-line tracking and spiral tracking, the simulation parameters are the same as the settings in Section 3.1, and the actual trajectory is calculated using the electromechanical coupling dynamics model.

3.2.1 Straight Linear Conditions

It can be seen from Fig. 7 that the MPC control method can overcome the influence of the initial y direction deviation under the condition of electromechanical coupling dynamics. The purpose of tracking the target trajectory is achieved by adjusting the voltage and frequency of the motors on both sides. In the trajectory tracking process, the distance error between the controlled vehicle and the target line in the y direction is continuously reduced, and the distance error in the x direction is increased first and then decreased. After 20 s, both errors are reduced to 0, and the vehicle achieves accurate tracking. After that, the vehicle remained stable, and the distance error and the angle error were kept at 0.

3.2.2 Spiral Conditions

As shown in Fig. 8, in the spiral trajectory tracking condition, the MPC control method can make the vehicle overcome the influence of the initial distance error and angle error under dynamic conditions. During the tracking process, the voltage and frequency control amount of the right motor has a certain fluctuation, and the left changes smoothly. After 32 s, the tracking is basically realized. The angular error has a certain overshoot during the tracking process, but the distance error and the angle error keep at 0 after the accurate tracking.

Based on the above dynamic simulation results and kinematic simulation results, the state-space based model predictive control algorithm can realize the trajectory tracking of the linearized track vehicle model under different path curves and different initial deviation conditions. The trajectory tracking result is good, which can meet the requirements of trajectory tracking control of unmanned track vehicles. Adding the motor characteristics into the trajectory tracking control can ensure the performance matching and safety of the motor and the track vehicle during the operation.

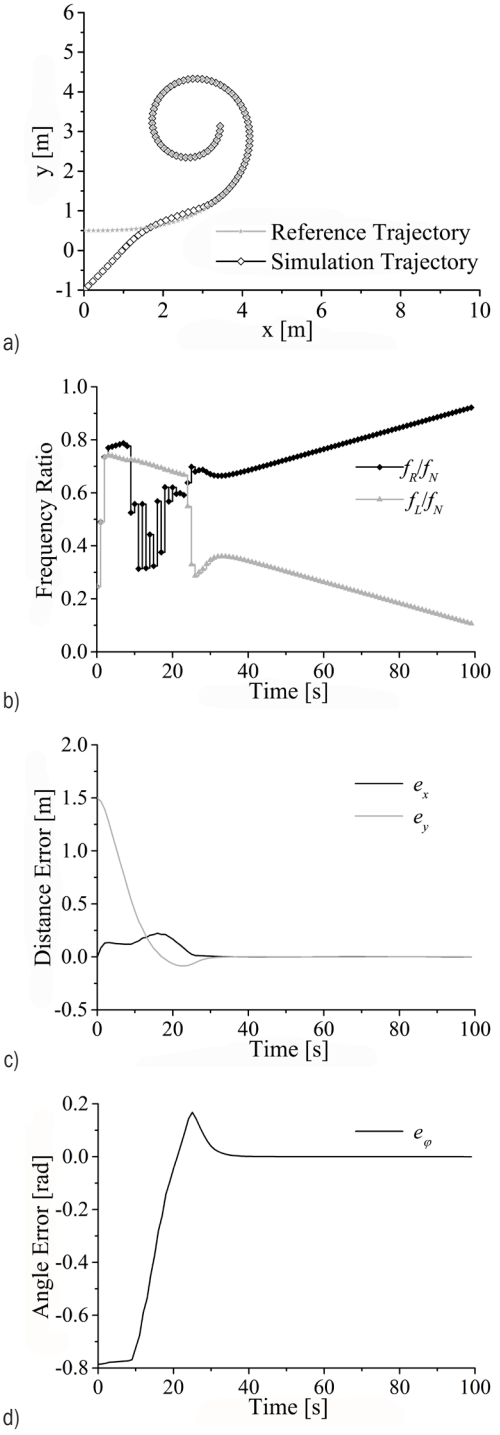

Fig. 8. *Spiral-line tracking result; a) trajectory comparison, b) velocity fluctuation, c) distance error, and d) angle error*

4 EXPERIMENTAL VERIFICATION

To verify the performance of the trajectory tracking control system in a real environment, in this section, we designed a set of the proportional model test device. Set different predetermined trajectories and use visual recognition to obtain lateral vehicle deviation and angular deviation. The Kalman filter

is used for reducing signal interference, and the trajectory tracking predictive control algorithm is used to control and verify the performance of the control system.

4.1 Track Test Device

The experiment devices are shown in Fig. 9, including the crawler, stepper motor, driver, camera, etc. The crawler's parameters are shown in Table 1. The stepper motor model is 42BYG34-401A, and the camera resolution is 1920×1080.

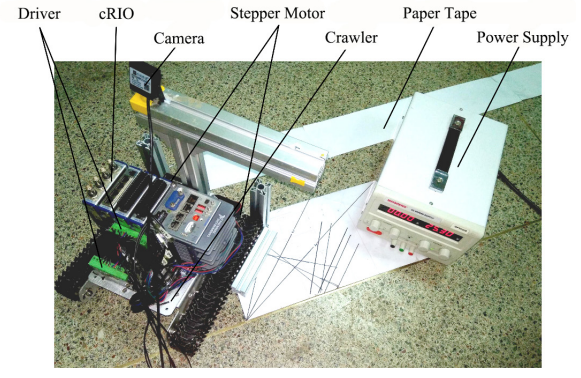

Fig. 9. *Track test device*

Table 1. *Parameters of the crawler*

Name	Value [mm]
Center distance	220
Track shoe width	40
Total length	280
Drive wheel circumference	124
Track grounding length	140
Total height	90

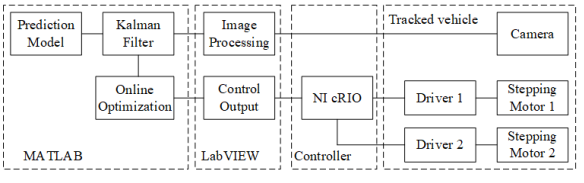

Fig. 10. *Predictive control system structure*

The predictive control system uses the camera to capture the target trajectory of the ground mark. After processing with LabVIEW, use MATLAB and combine the track vehicle kinematics model and Kalman filter to calculate the current lateral deviation and angular deviation. Use MATLAB to give the control amount. LabVIEW inputs the control amount to the controller NI cRIO through the serial port, and cRIO converts it into the corresponding electric signal input to the stepper motor, which drives the track forward. The structure of the control system is shown in Fig. 10.

4.2 Monocular Visual Deviation Calculation

The experiment uses monocular visual to ranging. During the crawler's movement, the camera shoots the ground mark at the regular time. LabVIEW converts the image into a black and white binary image and fits the target trajectory line, as shown in Fig. 11.

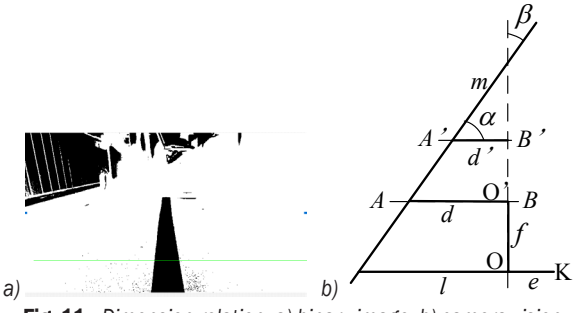

Fig. 11. *Dimension relation; a) binary image, b) camera vision*

In the camera's vision, a horizontal line is preset corresponding to a virtual line on the ground, as shown by the green line (line $A'B'$) and line AB in Fig. 11. Point K is the position of the crawler, point O is the position of the camera, and line m is the reference trajectory which is pre-paved on the ground by the paper tape. By measuring the angle between the straight line $A'B'$ and fitted line m, and the distance d' between the vertical line and the line m on $A'B'$, the lateral deviation l and angular deviation β can be obtained with the principle of similar triangles. The calculation method is as follows:

$$\begin{cases} \alpha = \dfrac{\pi}{2} - \beta \\ d = d' \cdot \dfrac{AB}{A'B'} \\ l = \dfrac{d\tan\alpha + f}{\tan\alpha} + e \end{cases} . \tag{42}$$

In Eq. (42), d' is the fitting pixel distance and d is the virtual deviation; AB is the distance of the line pixel; f is the distance between line AB and the centre of the track, and e is the lateral deviation of the camera installation position from the centre of the track.

4.3 Algorithm Based on Kalman Filter

During the movement of the track vehicle, it is difficult to obtain accurate system state variables due

to vibration errors, straight-line fitting errors, and the random noise of the camera. Using a Kalman filter, the optimal weighting matrix can be calculated by iteration. Then by weighting the measurement and the predicted state, the optimal state estimation can be obtained. Using the linearized kinematics model for predictive control, the state equation of the system can be written as:

$$\begin{cases} \mathbf{x}_k = \mathbf{A}_k \mathbf{x}_{k-1} + \mathbf{B}_k \mathbf{u}_{k-1} \\ \mathbf{y}_k = \mathbf{C}\mathbf{x}_k \end{cases}, \tag{43}$$

where $\mathbf{y}_k$ is the output, and $\mathbf{C}=diag(0,1,1)$. Assume the system have input noise $\mathbf{w}_{k-1}$ and observation noise $\mathbf{v}_k$, then the system state equation is:

$$\begin{cases} \mathbf{x}_k = \mathbf{A}_k \mathbf{x}_{k-1} + \mathbf{B}_k \mathbf{u}_{k-1} + \mathbf{w}_{k-1} \\ \mathbf{y}_k = \mathbf{C}\mathbf{x}_k + \mathbf{v}_k \end{cases}. \tag{44}$$

The Kalman filter uses the recursive method to find the estimated value of the state quantity under the minimum mean square error. The recursive equation is:

$$\begin{cases} \mathbf{P}'_k = \mathbf{A}_k \mathbf{P}_{k-1} \mathbf{A}_k^T + \mathbf{Q}_{k-1} \\ \mathbf{H}_k = \mathbf{P}'_k \mathbf{C}_k^T (\mathbf{C}_k \mathbf{P}'_k \mathbf{C}_k^T + \mathbf{R}_k)^{-1} \\ \hat{\mathbf{x}}_k = \mathbf{A}_k \hat{\mathbf{x}}_{k-1} + \mathbf{B}_k \mathbf{u}_{k-1} + \mathbf{H}_k (\mathbf{y}_k - \mathbf{C}_k \mathbf{A}_k \hat{\mathbf{x}}_{k-1}) \\ \mathbf{P}_k = (\mathbf{I} - \mathbf{H}_k \mathbf{C}_k) \mathbf{P}'_k \end{cases}, \tag{45}$$

where $\mathbf{Q}_{k-1}$ and $\mathbf{R}_k$ are the variance matrix of the input noise $\mathbf{w}_{k-1}$ and the observation noise $\mathbf{v}_k$, respectively; $\mathbf{H}_k$ is the gain matrix and essentially a weighting matrix; $\mathbf{P}'_k$ and $\mathbf{P}_k$ are the covariance matrix of the uncorrected and corrected state variable error estimates respectively.

4.4 Experiment Analysis

To verify the predictive control performance, the trajectory-tracking experiments are carried out under uniform linear motion condition with different target vehicle velocities and different initial poses. According to the previous algorithm, write the corresponding MATLAB and LabVIEW program.

Fig. 12 shows the 30 s trajectory tracking control result of the track vehicle at the reference vehicle velocity of 0.03 m/s, the initial lateral error of –0.3 m and initial angular error of $\pi/3$. Figs. 12a and b show the lateral deviation curve and angular deviation curve under this condition. Due to the vehicle vibration, ground interference, and camera error, the tracking error has some fluctuations. After the Kalman filter, a smooth error curve can be obtained. At the beginning of the vehicle motion, the initial pose error is large because the initial pose is inconsistent with the initial target pose. After 20 s, the system realizes the accurate trajectory tracking, and then the lateral deviation and angular deviation are basically zero.

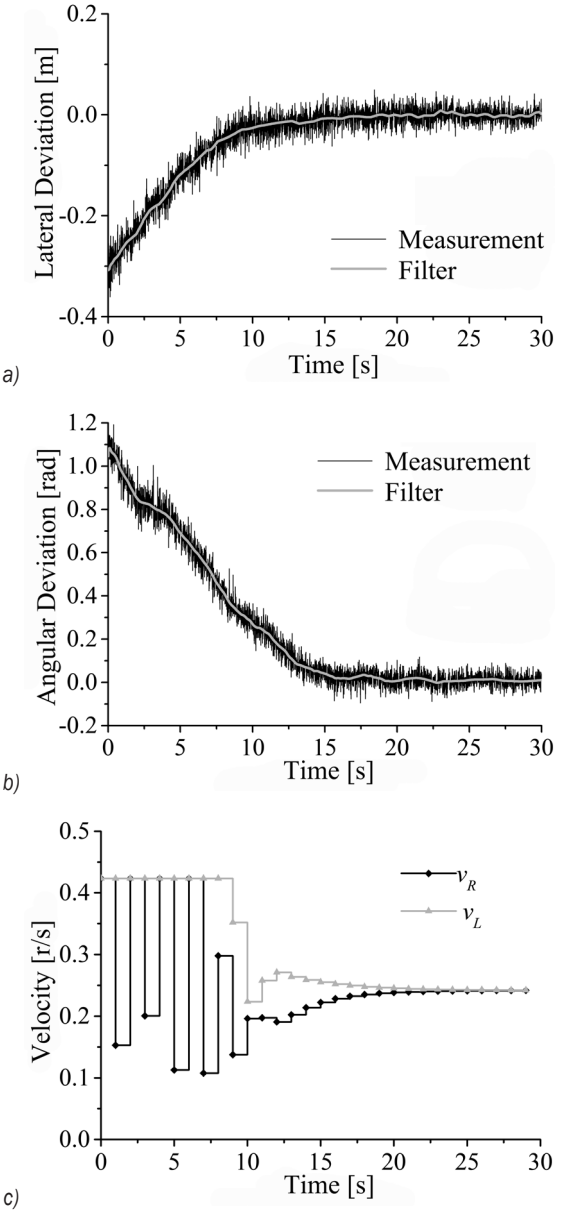

Fig. 12. *Straight line tracking result I, a) lateral deviation, b) angular deviation, and c) velocity fluctuation*

Fig. 13 shows the trajectory tracking control result of the track vehicle at the reference vehicle velocity of 0.06 m/s, initial lateral error of –0.5 m and initial angle error of $\pi/4$. It can be seen from the figure that the system overcomes the initial lateral angular deviation at about 15 s and realizes the accurate trajectory

tracking. After that, the deviation remains zero. It can be seen from Fig. 12 and Fig. 13 that the predictive controller based on monocular vision and the Kalman filter algorithm can realize accurate trajectory tracking and has good stability.

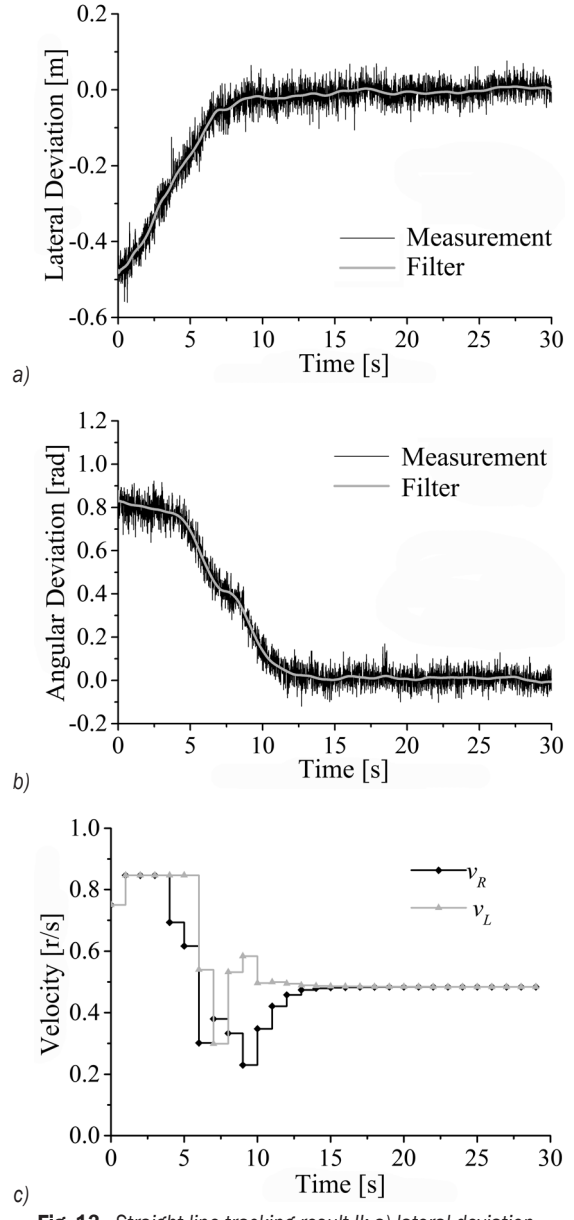

Fig. 13. *Straight line tracking result II; a) lateral deviation, b) angular deviation, and c) velocity fluctuation*

5 CONCLUSION

For the trajectory tracking control of track vehicles, this paper proposes a model predictive control algorithm based on state-space model. The algorithm uses the linear kinematics model of the track vehicle, and discretizes the state equation for predictive control of the vehicle.

First, this paper establishes the kinematics model of the track vehicle, and combines the vehicle dynamics model and the dynamic model of the induction motor to establish the electromechanical coupling dynamics model of the track vehicle. Based on the linear kinematics model of the track vehicle, the kinematic and dynamic trajectory-tracking prediction controllers are designed. The controller performs rolling optimization at each sampling time according to the lateral deviation and angular deviation between the vehicle trajectory and the target trajectory, and adjusts the vehicle heading and velocity in real time.

The kinematics and dynamics simulation experiments are designed using the proposed control algorithm, and are performed in a straight path and a spiral path. In the kinematic simulation, the crawler's velocity of both sides to track the target trajectory are adjusted. The dynamic simulation is tested for trajectory tracking by adjusting the voltage and frequency of the motor on both sides. The different lateral and angle deviations are set before the simulations start. The simulation results are as same as expected, showing that the algorithm can make the controlled vehicle overcome initial deviation and track the target trajectory in a short time, and maintain stable with no overshoot after tracking.

To verify the control effect of the algorithm in real vehicles, the proportional model of the track vehicle is used for control tests. A predictive control trajectory tracking system for real vehicles is designed based on monocular vision and Kalman filter. The tests are carried out under different target velocities and different initial poses. The results show that the algorithm can realize the trajectory tracking of a real vehicle prototype, and the effects can meet the trajectory-tracking requirements.

6 ACKNOWLEDGEMENTS

The research work financed with the National Natural Science Foundation of China (Grant No. 51775225) and key scientific and technological coal-based research projects in Shanxi (Grant No. MJ2014-02).

7 NOMENCLATURES

v_R, v_L	velocity on both sides, [m/s]
R	turning radius, [m]
B	track centre distance, [m]
v_c	centroid speed, [m/s]
ω_c	centroid angular velocity, [rad/s]

φ	angle between v_c and the X axis, [-]
b	width of the track shoes, [m]
l	track grounding length, [m]
m	vehicle mass, [kg]
F_{qr}, F_{ql}	driving forces on both sides, [N]
F_{rr}, F_{rl}	running resistance on both sides, [N]
F_{sr}, F_{sl}	steering resistance on both sides, [N]
J_c	moment of inertia, [kg·m^2]
δ	rotational mass factor, [-]
J_ω	total moment of inertia, [kg·m^2]
ω	motor shaft speed, [r/s]
T_{em}	motor electromagnetic torque, [N·m]
T_L	motor load torque, [N·m]
f_ω	rotational drag coefficient, [kg·m^2/s]
η	transmission system efficiency, [-]
J	moment of inertia of the motor shaft, [kg·m^2]
r	radius of the drive wheel, [m]
i	transmission ratio, [-]
$\mathbf{L}$	inductance matrix of the motor, [-]
$\mathbf{R}$	resistance matrix of the motor, [-]
p_0	number of pole pairs, [-]
$\mathbf{G}$	rotational inductance matrix, [-]
$\mathbf{i}$	current vector, [A]
$\mathbf{u}$	voltage vector, [V]
$\mathbf{x}(k)$	state vector, [-]
$\mathbf{u}(k)$	control input, [-]
$\mathbf{y}(k)$	control output, [-]
$\mathbf{A}$	state matrix, [-]
$\mathbf{B}$	control matrix, [-]
$\mathbf{C}$	output matrix, [-]

8 REFERENCES

[1] Marquardt, J.G., Alvarez, J., Von Ellenrieder, K.D. (2014). Characterization and system identification of an unmanned amphibious tracked vehicle. *IEEE Journal of Oceanic Engineering*, vol. 39, no. 4, p. 641-661, **DOI:10.1109/JOE.2013.2280074**.

[2] Stojković, V., Mikulić, D. (2002).The impact of a fixed kinematic turning radius of a tracked vehicle on the engine power required in a turn. *Strojniški vestnik - Journal of Mechanical Engineering*, vol. 48, no. 8, p. 459-466.

[3] Beetz, A., Schwieger, V. (2013). Automatic lateral control of a model dozer. *Journal of Applied Geodesy*, vol. 7, no. 4, p. 257-269, **DOI:10.1515/jag-2013-0003**.

[4] Cook, J.T., Ray, L.E., Lever, J.H. (2016). Dynamics model for mobility optimization and control of off-road tractor convoys. *Proceedings of the American Control Conference*, p. 6875-6880, **DOI:10.1109/ACC.2016.7526755**.

[5] Alvarez, J., Bertaska, I.R., Von Ellenrieder, K. (2013). Nonlinear control of an unmanned amphibious vehicle. ASME Dynamic Systems and Control Conference, p. V003T34A005, **DOI:10.1115/DSCC2013-4039**.

[6] Luo, L. (2015). Adaptive cruise control design with consideration of humans' driving psychology. *Proceedings of the 11th World Congress on Intelligent Control and Automation*, p. 2973-2978, **DOI:10.1109/WCICA.2014.7053202**.

[7] Yeu, T.K., Hong, S., Kim, H.W., Choi, J.S. (2005). Path tracking control of tracked vehicle on soft cohesive soil. *Proceedings of the ISOPE Ocean Mining Symposium*, p. 168-174.

[8] Zou, T., Angeles, J., Hassani, F. (2018). Dynamic modeling and trajectory tracking control of unmanned tracked vehicles. *Robotics and Autonomous Systems*, vol. 110, p. 102-111, **DOI:10.1016/j.robot.2018.09.008**.

[9] Huang, P., Zhang, Z., Luo, X., Zhang, J., Huang, P. (2018). Path tracking control of a differential-drive tracked robot based on look-ahead distance. *IFAC-PapersOnLine*, vol. 51, no. 17, p. 112-117, **DOI:10.1016/j.ifacol.2018.08.072**.

[10] Chen, C.-Y., Li, T.-H.S., Yeh, Y.-C., Chang, C.-C. (2009). Design and implementation of an adaptive sliding-mode dynamic controller for wheeled mobile robots. *Mechatronics*, vol. 19, no. 2, p. 156-166, **DOI:10.1016/j.mechatronics.2008.09.004**.

[11] Yandong, L., Zongyi, W., Ling, Z., Tao, L. (2011). Sliding mode control of mobile robots based on recurrent fuzzy-neural network. *Journal of Jilin University (Engineering and Technology Edition)*, vol. 41, no. 6, p. 1731-1737, **DOI:10.13229/j.cnki.jdxbgxb2011.06.022**. (in Chinese)

[12] Jeon, C.W., Kim, H.-J., Han, X.Z., Kim, J.-H. (2017). Fuzzy logic-based steering controller for an autonomous head - Feed combine harvester. *ASABE Annual International Meeting*, **DOI:10.13031/aim.201700927**.

[13] Dai, Y., Zhu, X., Zhou, H., Mao, Z., Wu, W. (2018). Trajectory tracking control for seafloor tracked vehicle by adaptive neural-fuzzy inference system algorithm. *International Journal of Computers, Communications and Control*, vol. 13, no. 4, p. 465-476, **DOI:10.15837/ijccc.2018.4.3267**.

[14] Endo, D., Okada, Y., Nagatani, K., Yoshida, K. (2007). Path following control for tracked vehicles based on slip-compensating odometry. *IEEE International Conference on Intelligent Robots and Systems*, p. 2871-2876, **DOI:10.1109/IROS.2007.4399228**.

[15] Lenain, R., Thuilot, B., Cariou, C., Martinet, P. (2007). Adaptive and predictive path tracking control for off-road mobile robots. *European Journal of Control*, vol. 13, no. 4, p. 419-439, **DOI:10.3166/ejc.13.419-439**.

[16] Bahadorian, M., Savkovic, B., Eaton, R., Hesketh, T. (2011). Toward a robust model predictive controller applied to mobile vehicle trajectory tracking control. *IFAC Proceedings Volumes (IFAC-PapersOnline)*, vol. 44, no. 1, p. 13552-13557, **DOI:10.3182/20110828-6-IT-1002.01786**.

[17] Shen, C., Shi, Y., Buckham, B. (2018). Trajectory tracking control of an autonomous underwater vehicle using Lyapunov-based model predictive control. *IEEE Transactions on Industrial Electronics*, vol. 65, no. 7, p. 5796-5805, **DOI:10.1109/TIE.2017.2779442**.

[18] Falcone, P., Borrelli, F., Asgari, J., Tseng, H.E., Hrovat, D. (2007). Predictive active steering control for autonomous vehicle systems. *IEEE Transactions on Control Systems Technology*, vol. 15, no. 3, p. 566-580, **DOI:10.1109/TCST.2007.894653**.

[19] Lee, S.H., Lee, Y.O., Son, Y., Chung, C.C. (2011). Proximate model predictive control strategy for autonomous vehicle lateral control. *11th International Conference on Control,*

Automation and Systems, p. 590-595, **DOI:10.1109/acc.2012.6315465**.

[20] Kim, B.-A., Lee, S.-H., Lee, Y.O., Chung, C.C. (2012). Comparative study of approximate, proximate, and fast model predictive control with applications to autonomous vehicles. *12th International Conference on Control. Automation and Systems*, p. 479-484.

[21] Backman, J., Oksanen, T., Visala, A. (2010). Nonlinear model predictive trajectory control in tractor-trailer system for parallel guidance in agricultural field operations. *IFAC Proceedings Volumes*, vol. 43, no. 26, p. 133-138, **DOI:10.3182/20101206-3-JP-3009.00023**.

[22] Kayacan, E., Ramon, H., Saeys, W. (2017). Robust trajectory tracking error model-based predictive control for unmanned ground vehicles. *IEEE/ASME Transactions on Mechatronics*, vol. 21, no. 2, p. 806-814, **DOI:10.1109/TMECH.2015.2492984**.

[23] Guanyu, Z., Guoqiang, W., Huanyu, Z. (2017). Simulation analysis of electromechanical performance of crawler of mobile crushing station. *Journal of the Brazilian Society of Mechanical Sciences and Engineering*, vol. 39, no. 12, p. 4943-4954, **DOI:10.1007/s40430-017-0907-5**.

[24] Kitano, M., Kuma. M. (1977). An analysis of horizontal plane motion of tracked vehicles. *Journal of Terramechanics*, vol. 14, no. 4, p. 211-225, **DOI:10.1016/0022-4898(77)90035-0**.

[25] Wang, X., Taghia, J., Katupitiya, J. (2016). Robust model predictive control for path tracking of a tracked vehicle with a steerable trailer in the presence of slip. *IFAC-PapersOnLine*, vol. 49, no 16, p. 469-474, **DOI:10.1016/j.ifacol.2016.10.085**.

Strojniški vestnik - Journal of Mechanical Engineering 65(2019)6, 343-350
DOI:10.5545/sv-jme.2019.6004
Original Scientific Paper
Received for review: 2019-01-15
Received revised form: 2019-05-10
Accepted for publication: 2019-05-31

Residual Stress-induced Distortions in Laser Powder Bed Additive Manufacturing of Nickel-based Superalloys

Özgür Poyraz[1,*] - Melih Cemal Kuşhan[2]
[1]TEI, Tusaş Engine Industries Inc., Turkey
[2]Eskişehir Osmangazi University, Faculty of Engineering, Department of Mechanical Engineering, Turkey

One of the significant process limits of laser powder bed additive manufacturing technologies is residual stresses and distortions induced by heating the fine metal powder to the melting point and sudden cooling to the initial temperature. While this phenomenon applies to most types of metal alloys, it becomes more important in nickel-based superalloys, which have low thermal conductivity and high-quality requirements for aerospace utilization. Together with the mechanical integrity and geometric problems in the final product, residual stress-induced distortions carry the potential risk of interrupting the job process above a certain distortion limit as a result of part-to-re-coater rubbing. Process simulations performed in a computer environment are of critical importance to predict and to prevent this risk. However, simulation models need to be verified through experiments, and they need to be cost-effective in terms of simulation times. This paper presents a comprehensive study to introduce a fast thermo-mechanical simulation model, together with experiments on nickel-based superalloy demonstrators. It also contributes to the scientific knowledge base with novel coupon design, manufacturing and evaluation methodology for distortion studies.
Keywords: additive manufacturing, finite element analysis, laser powder bed fusion, thermo-mechanical simulations

Highlights
- *A fast thermo-mechanical finite element model was introduced for the analysis of distortions and residual stresses in laser powder bed additive manufacturing.*
- *Novel benchmark coupons were designed for the benchmarking of residual stress-induced distortions considering circumferential effects.*
- *The thermo-mechanical finite element model was employed for the simulation of benchmark coupons.*
- *Experiments were conducted for an Inconel 718 nickel-based superalloy using a laser powder bed fusion additive manufacturing system*
- *Results were evaluated via a coordinate measuring machine equipped with a laser scanner head.*
- *Successful convergence was achieved with the experimental results.*

0 INTRODUCTION

Laser powder bed fusion (LPBF) is a powder bed additive manufacturing (AM) process used for the production of three dimensional (3D) parts from a wide range of powder materials; it is known with different commercial names, such as selective laser melting (SLM), selective laser sintering (SLS) or direct metal laser sintering (DMLS) [1]. It expands its sectorial utilization by offering good mechanical properties, design freedom [2], easy transition from design to manufacturing, post-processing ability, and low material consumption [3]. Regardless of the various advantages offered by LPBF, remaining challenges such as surface quality [3], residual stresses, distortions [4], or the use of support structures prevent the wider acceptance of this process.

LPBF AM uses a laser beam to selectively melt the metal powders by scanning cross sections on the surface of a powder bed layer by layer into an object that has a desired 3D shape based on a computer-aided design (CAD) model [5]. After each cross-section is scanned through a mirror system and solidifies with the help of blowing inert gas, the powder bed is lowered by one layer of thickness, a new layer of material is spread on top with a re-coater, and the process is repeated until the part is complete [4]. In this respect, heat transfer mechanisms include phase change, conduction, convection, and radiation (Fig. 1). As a result of the above-mentioned phenomenon, occurring thermal gradients cause cyclic thermal expansions, which exceed the elastic strain of the material and generate plastic strains, especially at high temperatures. These cumulated strains can generate internal stresses (also known as residual stresses) in the part [6] and cause distortions, which may lead failure by cracking [7] or layer delamination [8].

To eliminate the risk of cyclic thermal expansions and the resultant problems of residual stresses and distortions, several measures can be taken. In this regard, to check residual stresses, inspection techniques can be employed such as neutron diffractometry [9] or X-ray diffraction [10], and distortions with dimensional measurement systems [11] can be used. However, due to the rapid nature of additive manufacturing, these techniques are not

*Corr. Author's Address: TEI, Tusaş Engine Industries Inc., 26210 Eskişehir, Turkey, ozgur.poyraz@tei.com.tr

available for in-process control but are commonly used for the final product. Most of the time, detected problems of residual stresses and distortions [12] are overcome on the final product using additional operations, such as stress relieving and/or machining adding extra costs on the product. Moreover, in certain cases, these additional operations may not be useful owing to high stresses or large distortions. On the other side, they are still insufficient to eliminate in-process risks, such as delamination, cracking, or job interruption, due to part-to-re-coater rubbing.

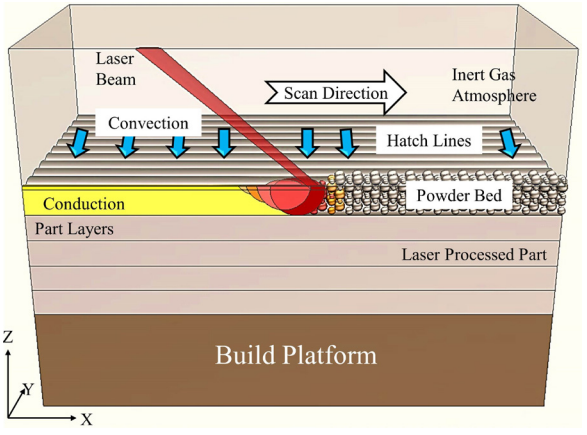

Fig. 1. *Heat transfer mechanisms occur as the result of the process* [4]

For these reasons, computer-based numerical simulation tools or methods are developed and used to predict residual stresses and distortions. Within the literature, studies on LPBF AM simulations mainly focus on numerical modelling to understand the process itself and the effect of process parameters on the quality of the produced parts.

The state-of-the-art in this field includes different studies and applications on various problems. Accordingly, thermal models coupled with mechanical ones can be used to numerically simulate LPBF processes to understand the effect of different process parameters [13]. The results of these simulations may include the shape and size of the melt pool, temperature distribution, as well as residual stresses and deformations [14]. While this approach is useful for meso-scale process simulations, it may be computationally expensive for macro-scale ones [15]. To overcome this computational expense, several researchers have employed diverse approaches. In the beginning phases of additive manufacturing simulations, researchers focused on reducing the mesh count and thus the computation time by using the element birth-and-death technique provided by the general-purpose finite element method (FEM) software packages such as ABAQUS [16] and ANSYS [17]. However, due to the lack of a recordable time reduction in the simulation times, there was a tendency towards other methods in the following periods. The applied plastic strain method is one of the most commonly used methods, using high-resolution models of the transient thermo-mechanical analysis, it calculates plastic strain tensor components with equivalent plastic strain and maps the obtained plastic strains on the complete part [18].

This study deals with this challenge by introducing a fast thermo-mechanical finite element model. Together with the proposed model, experimental studies were also conducted on complex parts made of nickel-based superalloys. In this regard, innovative circumferential coupon designs were employed to promote a comprehensive understanding of residual stress induced distortion phenomenon. Verification of the simulation model was accomplished using experimental values.

The rest of the paper is organized as follows: In the next section, details of the thermo-mechanical model were presented among with the coupon geometry designs, necessary material properties and boundary conditions for finite element analysis. The following section explains the experimental procedure in terms of manufacturing and inspection steps. Findings are discussed in the subsequent section with the comparison of modelling results versus experiments. The last section summarizes the paper and emphasizes the potential work to be done.

1 METHODS

1.1 Coupon Designs

Various types of coupon designs can be utilized to understand the residual stress-induced distortions as a result of LPBF AM. Due to the longer computation times, previous studies used simplistic coupon designs of prismatic shapes to have a constant cross-section along the part [19]. In a few studies, which employs complex geometry, it can be seen that unidirectional cantilever beams are used with arrayed combs to allow distortions [20]. Although these provide useful information about the distortions as a result of LPBF AM and process parameters, they are not sufficient to reflect different aspects such as the multi-directional differences of distortions due to re-coater movement and/or inert gas blowing. Multi-directional situations were also considered in other previous research,

but they still lack the evaluation of asymmetry as a significant issue [21].

In the context of this research, innovative coupon geometries were designed with two configurations. These are circumferentially arrayed cantilever beams with 120° between each beam. The first configuration (C1) employs combs on all beams for investigating the symmetrical situation in terms of distortion results. The second configuration (C2) employs combs on two beams and one of the beams as a full solid without any comb. This is to see the effect of asymmetry on the geometry and also unbalanced material volumes on the parts to effect residual stress-induced distortions. The external dimensions of both coupons were kept equivalent for a fair benchmark, and these dimensions were also kept as low as possible for minimum material consumption. Each coupon has an outer diameter of 70 mm and each beam has outer dimensions of 35 mm × 10 mm × 7 mm. Combs have a thickness of 1 mm and a height of 4.5 mm. A 1 mm gap is present between each comb. Fig. 2 shows the coupons with external dimensions.

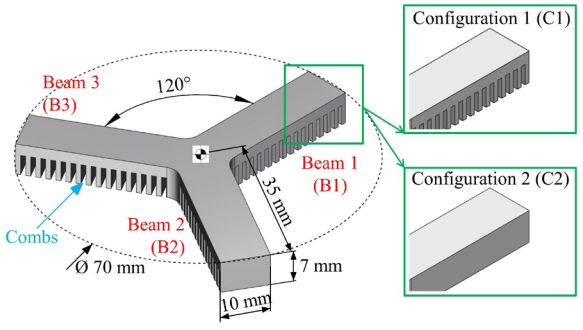

Fig. 2. *Circumferential coupons and dimensions*

1.2 Materials and Properties

Among various LPBF processed superalloys, Inconel 718 was chosen for the material; it has major elements of nickel (52.5 %), chromium (19 %), iron (balance), and niobium (5.12 %). It possesses both oxidation resistance and high strength at elevated temperatures. Moreover, different forms of Inconel 718 are easily producible with conventional and non-conventional processes, such as machining, welding, and additive manufacturing [22]. Inconel 718, which is preferred in different sectors with its many advantages in terms of design and production, is used in the highest ratio for aircraft engines. An example of this is the PW4000 engine from Pratt & Whitney [22]. The total ratio of nickel alloys used in the example engine, which provides power to the commercial platforms such as Boeing 747, Boeing 767, and Airbus 300, is 39 %, and the total utilization rate of Inconel 718 in these nickel alloys is 57 %.

In this study, EOS Nickel Alloy IN718 was considered for the part material, and all the necessary material properties (physical, thermal, mechanical) for modelling were calculated with JMatPro® software. According to the proposed methodology, which is explained in the following section, the fast thermo-mechanical model predicts the distortions in the solid phase and uses material properties below melting temperatures.

The physical phenomena of the process were taken into account, and elasto-plastic behaviour was assumed for the material. Within the elastic region, linear elasticity calculations were conducted using the elastic modulus and Poisson ratio. For the plastic region, von Mises yield criteria were followed, and the temperature dependence of yield strength was adopted. Moreover, the bilinear hardening rule was included using the tangent modulus. Essential properties are given in Table 1 for three different temperature levels. The temperatures between this range and below melting point were extrapolated using polynomial curve fitting of second order.

Table 1. *Material properties of as-built IN718*

Material property [°C]	20	400	600
Density [kg/m³]	8195	8100	8000
Thermal conductivity [W/(m·K)]	11.25	13.45	15.55
Specific heat capacity [J/(kg·K)]	415	495	580
Thermal expansion $\times 10^{-6}$ [1/K]	13.0	14.8	16.6
Elastic modulus [GPa]	172	156	143
Poisson ratio [-]	0.29	0.28	0.27
Yield strength [MPa]	707	512	260
Tangent modulus [MPa]	920	785	603

1.3 Modelling

To overcome the challenge of computationally expensive LPBF AM modelling, a fast thermo-mechanical finite element model was introduced based on previous studies [13] and [15]. The model was developed using COMSOL Multiphysics FEM software as a result of a series of studies. In the scope of initial studies, a meso-scale model based on a moving heat source with Gaussian distribution was adopted just for thermal simulations [13] and for IN718 material was verified through microstructural investigations on the melt pool dimensions [15]. The convergence of less than 10 % was achieved with the meso-scale model (Fig. 3).

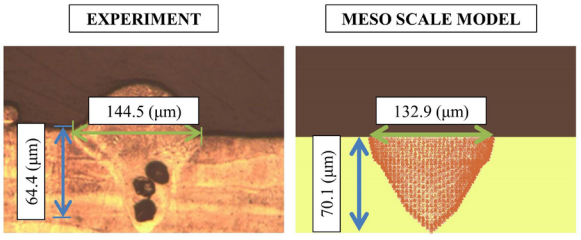

Fig. 3. *Results of previously developed meso-scale model* **[15]**

Later, comprehensive parametric analyses were conducted, and the model was accelerated to be used in macro-scale problems having real part geometries **[15]**. In this regard, the meso-scale model was utilized for various scanning strategies such as band, island, and spiral scanning. Average energy input per unit area and temperature distribution were extracted from the results of these studies. Equivalent energy input was applied to whole layers as a surface heat source simultaneously during the build process by multiplying the energy input per unit area value with the area value of each layer (Fig. 4). The time for the application of the energy input was calculated through dividing surface area value of each layer by the hatch distance multiplied with laser scanning speed (Fig. 4).

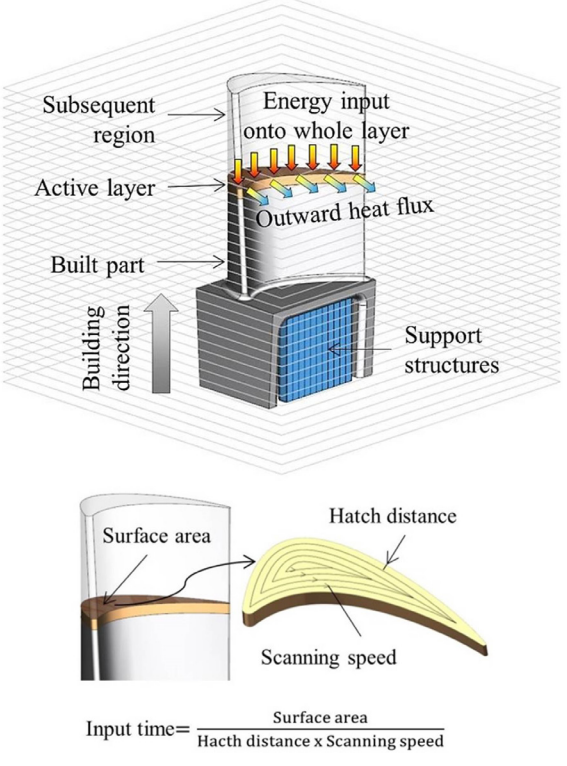

Fig. 4. *Fast thermo-mechanical model and input time calculation*

Temperature rise due to high loading was reported to be between 5 °C to 30 °C in the literature **[23]**. Since there is low-level loading in AM due to low strain rates and the temperature levels in AM process are extremely high, such as over 1000 °C comparing to 5 °C to 30 °C, the effect of deformation on temperature change was neglected. A one-way or weakly coupled thermo-mechanical model was developed, and multiphysics simulations were conducted accordingly. In this type of modelling strategy, the temperature distribution as the result of energy input and heat transfer was mapped simultaneously and transiently to structural mechanics in the same FEM software.

1.4 Boundary Conditions

The designed coupon geometries among with the calculated material properties were used for the modelling study, employing the developed fast thermo-mechanical model.

For the thermal boundary conditions, the initial condition at time $t = 0$ was set to 20 °C, and the bottom surface temperature of the part geometry was set to 80 °C to simulate the actual condition of build platform pre-heating step. As indicated in the modelling section, equivalent energy input was applied to whole layers as a surface heat source and a convective heat flux condition with a heat transfer co-efficient of 0.0178 W/(m^2·K) **[24]** was also applied to simulate the effect of argon flow inside the build chamber. The thermal insulation condition was applied for the side surfaces of the part geometry. The reason for this that the side faces of the part geometry are surrounded by powder material, and its thermal conductivity is extremely low **[13]** and can be neglected comparing it to solid material.

A fixed constraint was assigned to bottom surfaces of the coupon parts. Layer addition was also taken into account with the moving mesh algorithm of the layer plane. For this purpose, the part geometry was modelled at full height, and the block envelope for the geometry was also generated. A predefined Boolean operation (subtract) of block envelope from part geometry was assigned, and the block envelope was transiently transformed with a step function to consider 0.04 mm layer thickness as a step movement interval and also the layer time as explained in the modelling section. In the final step of simulations, the fixed constraint was deactivated to reflect the real situation of part separation from the build platform.

Mesh size was utilized as the result of mesh sensitivity analyses to allow proper heat dissipation through layer plane and through the side faces. In this

regard, constant mesh distribution was maintained on the layer plane to facilitate a minimum of two mesh elements for related geometry width and a minimum of five mesh elements for geometry length. Mesh elements on side faces were maintained with a geometric sequence distribution function to re-mesh the part and update a fine mesh size beneath the layer plane and coarsen the elements close to the part bottom for each layer addition. With this aim, the layer plane surface of the part was meshed with fixed sized triangular elements, and the rest of the geometry was swept with tetrahedral elements. The size of the tetrahedral elements was limited to a minimum value of 0.25 mm and a maximum value of 5 mm. An element growth ratio of 1.25 was defined to regulate the mesh growth from the minimum to maximum value in each build stage (Fig. 5).

The adaptive solver algorithm feature of the software package was used to transfer nodal history variables for each re-meshing step. For this case of a transient situation, the solution at a certain time interval (of a certain part layer) to the partial differential equation problem on the previous mesh was mapped to the new mesh of the following time interval step. This cycle continued automatically until the end of the simulations.

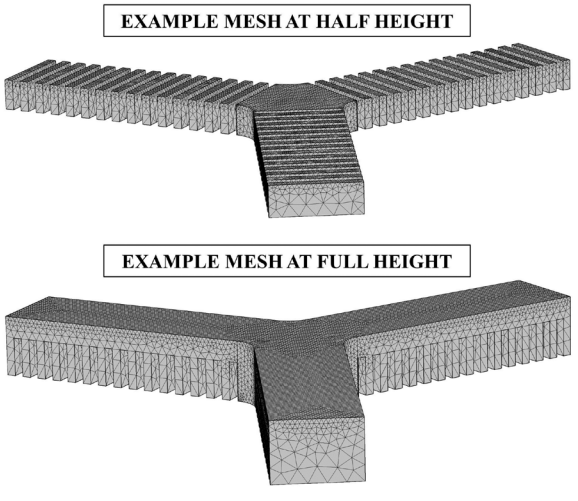

Fig. 5. *Mesh examples in different part heights*

1.5 Computations

The computational studies were conducted in a notebook computer with a central processing unit that had two physical cores and four logical cores with hyper-threading option by a clock speed of 2.40 GHz. Moreover, the computer featured 16 GB of random access memory to facilitate random storing of intermediate simulation data resulting because of the transient iterative solver.

Benchmark studies were conducted by using the above-explained hardware. First, the full layer of the part geometry was simulated using the meso-scale model, and the computation time was 3 hours and 16 minutes. Later, the meso-scale model was used for energy input calibration on a reference unit geometry, ending in 21 minutes. Finally, the simulation for the whole part geometry was conducted in 1 hour 7 minutes. With the proposed fast modelling strategy, the overall computation time was the sum of the calibration, and the whole part simulation and the value was 1 hour 28 minutes. The whole part simulation with the meso-scale model was not conducted, since it could be seen from the one layer simulation that it would take hundreds of hours. From this benchmark, it is obvious that the introduced fast thermo-mechanical model represents considerable benefits in terms of computational expense.

2 EXPERIMENTAL

2.1 Part Manufacturing

The designed coupons are manufactured in EOS M290 machine of EOS IN718 metal powder. To eliminate any collision or rubbing of coupon parts with the powder re-coater, one of the arms of the coupon was aligned with the X-axis and then rotated 5°.

Laser scanning strategies were adjusted for a proper comparison between the modelling and experimental studies, considering the fact that simulation was conducted with an accelerated thermo-mechanical model that simultaneously applies equivalent energy input to whole layer surface. In this respect, parallel scanning was chosen as the scanning strategy, and the angles of the scanning paths were rotated by a certain degree in each layer so that the

Table 2. *Process parameters for IN718*

Parameter	Value
Laser power	285 W
Laser scanning speed	960 mm/s
Hatch distance	0.11 mm
Layer thickness	0.040 mm
Stripe width	10.0 mm
Stripe overlap	0.12 mm
Hatching	X & Y
Strategy	Alternating
Angle	67°

heat distribution did not intensify anywhere through the building process.

Essential LPBF processing parameters are given in Table 2.

2.2 Part Measurement

Part measurements were conducted after the parts were removed from the building platform by cutting with an electric discharge machine. The distorted parts as a result of relieving residual stresses after removal from building platform were measured with a Nikon Altera coordinate measuring machine equipped with a non-contact laser scanner (Fig. 6). For a detailed evaluation, many points were obtained during measurement, and the resultant point cloud was exported in stereolithography (STL) file format.

Fig. 6. *Part measurement with a non-contact laser scanner*

3 RESULTS AND DISCUSSIONS

The results of the study were evaluated and discussed from two different perspectives. In the first perspective, modelling and experimental results were compared with each other to understand the convergence of the proposed modelling methodology. In the second perspective, experimental results were discussed for a better understanding of the process and the use of proposed coupon designs for residual stress induced distortion evaluation.

Finite element analyses were performed for the proposed model following to assignment of part geometry, material properties and boundary conditions, and outputs were obtained as part deformation (Fig. 7). Deformed part geometry was also exported in STL file format compatible to measurement results. Both STL files (one from measurement results and one from modelling) were imported to single CAD software for comparison purposes, and both geometries were aligned from their top faces.

The comparison was made using the height (Z value) references of edges at the end of each beam. Modelling and measurement results are presented in Table 3. In Table 3, the convergence ratio was calculated as the ratio of the measurement to the modelling difference divided by measurement value.

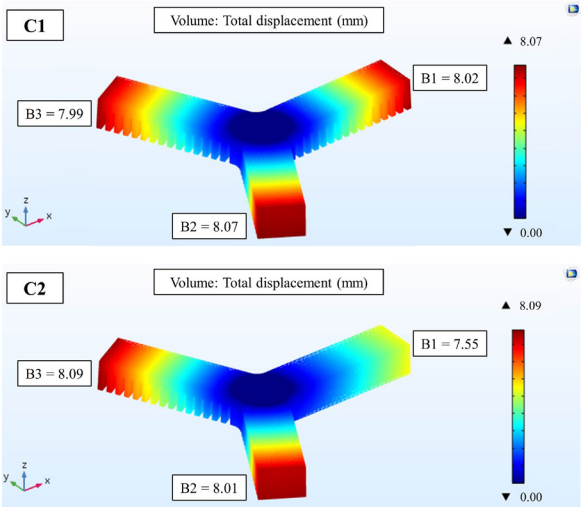

Fig. 7. *Example of the simulation results and reference edge numbers of coupons*

Table 3. *Comparison of modelling and experimental results*

Reference edge	Modelling [mm]	Measurement [mm]	Convergence ratio [%]
C1-B1	8.02	8.34	3.8
C1-B2	8.07	8.31	2.8
C1-B3	7.99	8.27	3.3
C2-B1	7.55	8.06	6.3
C2-B2	8.01	8.38	4.4
C2-B3	8.09	8.41	3.9

As can be seen from Table 3, the convergence between the modelling and measurement results is better than 10 %, based on the overall height of the edges of both coupons. The success of the convergence was obtained as the result of the proposed modelling method, since the modelling method considers equivalent energy input similar to the real situation utilized by parallel scanning with alternating angles. The proposed modelling method can also be used for the processes utilizing island (chessboard) or spiral scanning strategies [3]. Nevertheless, convergence in fixed-angle parallel or zigzag scans is not expected

to be as successful due to the remarkable thermal gradients between X and Y directions [19].

The experiments with the use of proposed coupon designs have also revealed noteworthy results. It can be observed from the results of coupon C1 that all deformation values in reference edges of B1, B2 and B3 are considerably close to each other, within a few microns. In contrast, it is evident from the results of coupon C2 that the distortion results of the reference edge B1 of the full beam is noticeably lower than B2 and B3, with 0.3 mm between each.

According to the extracted deduction from this study, it can be said that the effect of variables such as gas blow or powder re-coating direction is low in terms of distortion values of the same geometries in different layout positions and/or angles. In contrast, the difference in distortion values of geometries with varying features is high. In light of this information, it is recommended to reinforce the specific geometrical features in cases in which the residual stress-induced distortion problems are experienced and cannot be solved by the different positioning of the part.

5 CONCLUSIONS

One of the process limits of LPBF AM is residual stress induced distortions to expose mechanical integrity and geometric problems in the final product. Compared to other metallic materials, this problem becomes more important for nickel-based superalloys having low thermal conductivity and high quality requirements for aerospace utilization. The lack of in-process measurement techniques, difficulty in overcoming resultant problems and the risk of job failures show the importance of employing computer-based numerical simulation tools or methods to predict residual stresses and distortions.

This study introduced a fast thermo-mechanical finite element model together with experiments conducted on complex parts made of nickel-based superalloys, in this case, Inconel 718. Unlike previous studies in the literature, innovative distortion coupon designs were also presented to facilitate a comprehensive understanding of circumferential effects during process.

The introduced thermo-mechanical model provided a computationally feasible method and showed good convergence results, better than 10 % for the case of strategy to rotate scanning vectors with an alternating angle. Via the equivalent energy input principle, the proposed method can also be used for the processes utilizing island or spiral scanning strategies.

The experimental results revealed that geometrical difference are mostly dominant in comparison to circumferential effects such as gas blow or powder re-coater on residual stresses and residual stress induced distortions.

Future studies may include detailed measurement of residual stresses using x-ray diffraction techniques, research on other nickel-based superalloys, parametric simulations on representative part geometries and consideration of other scanning strategies, such fixed-angle parallel or zigzag scans, by improving the modelling method.

6 ACKNOWLEDGEMENTS

The authors would like to thank TEI (Tusaş Engine Industries Inc.) for supporting this research.

7 REFERENCES

[1] Levy, G.N., Schindel, R., Kruth, J.P. (2003). Rapid manufacturing and rapid tooling with layer manufacturing (LM) technologies, state of the art and future perspective. *CIRP Annals-Manufacturing Technology*, vol. 52, no. 2, p. 589-609, **DOI:10.1016/S0007-8506(07)60206-6**.

[2] Thompson, M.K., Moroni, G., Vaneker, T., Fadel, G., Campbell, R.I., Gibson, I., Bernard, A., Schulz, J., Graf, P., Ahija, B., Martina, F. (2016). Design for additive manufacturing: trends, opportunities, considerations, and constraints. *CIRP Annals-Manufacturing Technology*, vol. 65, no. 2, p. 737-760, **DOI:10.1016/j.cirp.2016.05.004**.

[3] Poyraz, Ö., Kuşhan, M.C. (2018). Investigation of the effect of different process parameters for laser additive manufacturing of metals. *Journal of the Faculty of Engineering and Architecture of Gazi University*, vol. 33, no. 2, p. 729-742, **DOI:10.17341/gazimmfd.416479**.

[4] Kuşhan, M.C., Poyraz, Ö., Uzunonat Y., Orak, S. (2018). Systematical review on the numerical simulations of laser powder bed additive manufacturing. *Sigma Journal of Engineering and Natural Sciences*, vol. 36, no. 4, p.1197-1214.

[5] Guo, N., Leu, M.C. (2013). Additive manufacturing: technology, applications and research needs. Frontiers of Mechanical Engineering, vol. 8, no. 3, p. 215-243, **DOI:10.1007/s11465-013-0248-8**.

[6] Van Belle, L., Vansteenkiste, G., Boyer, J.C. (2012). Comparisons of numerical modelling of the Selective Laser Melting. *Key Engineering Materials*, vol. 504-506, p. 1067-1072, **DOI:10.4028/www.scientific.net/KEM.504-506.1067**.

[7] Mercelis, P., Kruth, J.P. (2006). Residual stresses in selective laser sintering and selective laser melting. *Rapid Prototyping Journal*, vol. 12, no. 5, p. 254-265, **DOI:10.1108/13552540610707013**.

[8] Nickel, A., Barnett, D., Link, G., Prinz, F. (1999). Residual stresses in layered manufacturing. *Proceedings of the solid Freeform Fabrication Symposium*, p. 239-246.

[9] Zaeh, M.F., Branner, G. (2010). Investigations on residual stresses and deformations in selective laser melting. *Production Engineering*, vol. 4, no. 1, p. 35-45, **DOI:10.1007/s11740-009-0192-y**.

[10] Vogel, M., Khan, M., Medina, J.I., Pinkerton, A., N'Dri, N., Megahed, M. (2012). A verified model of transient and residual stresses in Laser Direct Metal Deposition. *International Congress on Applications of Lasers and Electro-Optics*, p. 89-96, **DOI:10.2351/1.5062560**.

[11] Yang, Y.P., Jamshidinia, M., Boulware, P., Kelly, S.M. (2017). Prediction of microstructure, residual stress, and deformation in laser powder bed fusion process. *Computational Mechanics*, vol. 61, no. 5, p. 599-615, **DOI:10.1007/s00466-017-1528-7**.

[12] Piaget, A., Museau, M., Paris, H. (2017). Manufacturing space homogeneity in additive manufacturing – Electron beam melting case. *Strojniški vestnik - Journal of Mechanical Engineering*, vol. 63, no. 10, p. 553-558, **DOI:10.5545/sv-jme.2017.4365**.

[13] Kundakcıoğlu, E., Lazoglu, I., Poyraz, Ö., Yasa, E., Cizicioğlu, N. (2018). Thermal and molten pool model in selective laser melting process of Inconel 625. *The International Journal of Advanced Manufacturing Technology*, vol. 95, no. 9-12, p. 3977-3984, **DOI:10.1007/s00170-017-1489-1**.

[14] Andreotta, R., Ladani, L., Brindley, W. (2017). Finite element simulation of laser additive melting and solidification of Inconel 718 with experimentally tested thermal properties. *Finite Elements in Analysis and Design*, vol. 135, p. 36-43, **DOI:10.1016/j.finel.2017.07.002**.

[15] Poyraz, Ö. (2018) *Investigation of the Effects of Process Parameters for Laser Additive Manufacturing by Using Modeling and Simulation Methods*, PhD Thesis, Eskişehir Osmangazi University, Eskişehir.

[16] Ding, J., Colegrove, P., Mehnen, J., Ganguly, S., Sequeira Almeida, P.M., Wang, F., Williams, S. (2011). Thermo-mechanical analysis of Wire and Arc additive layer manufacturing process on large multi-layer parts. *Computational Materials Science*, vol. 50, no. 12, p. 3315-3322, **DOI:10.1016/j.commatsci.2011.06.023**.

[17] Zekovic, S., Dwivedi, R., Kovacevic, R. (2005). Thermo-structural finite element analysis of direct laser metal deposited thin-walled structures. *Proceedings SFF Symposium*, Austin.

[18] Keller, N., Ploshikhin, V. (2014). New method for fast predictions of residual stress and distortion of AM parts. *Solid Freeform Fabrication Symposium*, Austin p. 4-6.

[19] Shukla, M., Verma, V. (2014). Finite element simulation and analysis of laser metal deposition, *6th International Conference on Mechanical, Production and Automobile Engineering*, Cape Town.

[20] Neugebauer, F., Keller, N., Xu, H., Kober C., Ploshikhin, V. (2014). Simulation of selective laser melting using process specific layer based meshing. *Proceedings of Fraunhofer Direct Digital Manufacturing Conference*, Aachen.

[21] Sillars, S.A., Sutcliffe, C.J., Philo, A.M., Brown, S.G.R., Sienz, J., Lavery, N.P. (2018). The three-prong method: a novel assessment of residual stress in laser powder bed fusion. *Virtual and Physical Prototyping*, vol. 13, no. 1, p. 20-25, **DOI:10.1080/17452759.2017.1392682**.

[22] Paulonis, D.F., Schirra, J.J. (2001). Alloy 718 at Pratt & Whitney-Historıcal Perspectıve and Future Challenges. *TMS Superalloys 718. 625. 706 and Various Derivatives*, **DOI:10.7449/2001/Superalloys_2001_13_23**.

[23] Tao, J., Zhang, H., Zheng, Y., Chen, Z. (2018). Development of generalized interpolation material point method for simulating fully coupled thermomechanical failure evolution. *Computer Methods in Applied Mechanics and Engineering*, vol. 332, p. 325-342, **DOI:10.1016/j.cma.2017.12.014**.

[24] Lemmon, E.W., Jacobsen, R.T. (2004). Viscosity and thermal conductivity equations for nitrogen, oxygen, argon, and air. *International Journal of Thermophysics*, vol. 25, no. 1, p. 21-69, **DOI:10.1023/B:IJOT.0000022327.04529.f3**.

Strojniški vestnik - Journal of Mechanical Engineering 65(2019)6, 351-365

DOI:10.5545/sv-jme.2018.5944 Original Scientific Paper
Received for review: 2018-12-21
Received revised form: 2019-05-05
Accepted for publication: 2019-05-10

The Influence Rules of Cutter Parameters on the Contact Characteristics of Tooth Surfaces by Five Cut Processes and the Duplex Helical Method

Yu Zhang[1,*] – Hongzhi Yan[2] – Zhiyong Wang[1] – Qing Zhao[1]

[1] Central South University of Forestry and Technology, Institute of Modern Mechanical Transmission Engineering Technology, China

[2] Central South University, State Key Laboratory of High-Performance Complex Manufacturing, China

The principles of cutter parameters, such as the cutter tilt angle, the blade angle, and the cutter radius, are investigated in the five-cut process and the duplex helical method. The duplex helical method is an advanced and primary manufacturing method of face-milled spiral-bevel and hypoid gears, so it is necessary and urgent to understand its generalized theory. First, the different working principles of the cutter tilt mechanism in the two processing methods are analysed in detail, and the principal idea of the generalized theory for the duplex helical method is fully explored. Next, the influences of the blade angle and the cutter radius on the tooth surface meshing characteristics in the two processing methods are compared and analysed with the numerical analysis method; the results show that the relationships between the cutter parameters and the meshing characteristics are more regular and that the tooth-bending strength is higher in the duplex helical method, which provides a theoretical basis for effectively obtaining the optimal machine settings of spiral-bevel and hypoid gears.

Keywords: duplex helical method, spiral-bevel and hypoid gears, five-cut process, generalized theory, cutter parameter

Highlights

- *The different working principles of the cutter tilt mechanism in the two processing methods are analysed.*
- *The principal idea of the generalized theory for the duplex helical method is fully explored.*
- *The influences of the blade angles and the cutter radius on the meshing characteristics in the two processing methods are compared and analysed.*
- *The research work provides a theoretical basis for obtaining the optimal machine settings of spiral bevel and hypoid gears.*
- *The bending strength of the duplex helical method is significantly higher than that of the five-cut process.*

0 INTRODUCTION

At present, the machining technology of face-milling, spiral-bevel and hypoid gears has two major methods. One method is the traditional face-milling method called the 'five-cut process' or the 'fixed setting process', which is still widely used in developing countries, such as China [1] to [3]. The other method is called the 'duplex helical method' or the 'completing process', which has many advantages, such as higher machining efficiency, lower production cost, higher tooth strength, and dry cutting. Therefore, the five-cut process is gradually being replaced by the duplex helical method, and the duplex helical method will become an advanced and primary manufacturing method for face-milling, spiral-bevel and hypoid gears in China. However, there are significant differences and correlations between the generalized theories of the two methods.

The significant differences between the five-cut process and the duplex helical method are: (1) In the five-cut process, the convex and concave tooth surfaces of a pinion are separately cutting with two different head-cutters; the outside head-cutter processes the concave tooth surfaces, and the inside head-cutter cuts the convex tooth surfaces. The duplex helical method can cut both sides of the pinion or gear tooth slots completely, with a spread blade head-cutter, in one operation, from a solid blank. (2) There is a helical motion (does not exist in the five-cut process) in the duplex helical method to control bias on the pinion, which is a relative axial motion between the workpiece and the cutter, along the generating gear axis, during the generating roll. With either method, the cutter represents a tooth of an imaginary gear which rolls with the gear or the pinion being cut. Therefore, its shape and position determine the shape of the tooth surface, and the influences of its parameters on the tooth surface topography play an important role in revealing the generalized theories of the two methods.

The generalized theory of spiral bevel and hypoid gears manufactured with the five-cut process have been comprehensively presented by several gear scientists [4] to [6]. Gleason's most representative gear scientists establish the spatial geometry of Gleason

*Corr. Author's Address: Central South University of Forestry and Technology, Institute of Modern Mechanical Transmission Engineering Technology, Shaoshan South Road, No. 498, Changsha 410004, Hunan, China, zhyu@csuft.edu.cn

spiral bevel and hypoid gears, analyse the calculation approach of the tooth surface curvature, and introduce the generalized theory of the five-cut process [7] to [9]. The generalized theory and calculation method for the five-cut process are developed by Litvin et al. [10], Fuentes et al. [11], and Litvin and Fuentes [12], which is different from Gleason's technology. To avoid the root profile interference and the tooth edge contact, the blade geometry consists of four sections (tip, toprem, profile, and flankrem), as presented by Fan [13]. The application of the parabolic and Top-Rem profile blade are proposed by Litvin et al.[14] and Fuentes et al. [15] to avoid or reduce the areas of severe contact stresses and increase the endurance of spiral bevel gears. An optimal tooth modification for spiral bevel gears is introduced into the pinion tooth-surface by using a head-cutter with the bicircular profile and the optimal diameter to improve the load distribution and reduce the maximum tooth contact pressure and transmission errors [16] and [17]. Ma et al. [18] investigate the influences of the cutter diameter on the meshing performance of spiral bevel gears, such as the contact area, the contact pressure, the bending stress, the torsional stiffness, and the transmission error, with the finite element analysis methods.

Gleason invented the duplex helical method several decades earlier, but has not clearly published its generalized theory and only shows few formulas and calculating instructions [19]. To the best knowledge of the authors of this paper, little attention has been given to the generalized theory of the duplex helical method until now. The conversion between the specific machine-tool settings of a given hypoid generator and the neutral machine-tool settings of spiral bevel gears manufactured by the duplex helical method is investigated, and the parabolic blade profiles are applied to improve the tooth bearings described in [20]. A mathematical model of the general hypoid machine is proposed by Fong [21], this model includes several common modified motions, such as the modified generating roll ratio, the helical motion, and the cutter tilt, to simulate all face-milled spiral-bevel and hypoid gear-machining methods. A new methodology is presented to determine the basic machine settings of spiral bevel and hypoid gears manufactured by the duplex helical method in [22], and the effect of straight-lined and circular cutting-edge profiles on the meshing and contact of gear pair is analytically investigated to effectively improve meshing performance [23].

In summary, the differences and relations between the theories of the five-cut process and the duplex helical method, the primary idea and many other key scientific problems of the duplex helical method have not yet been solved. Therefore, on the basis of analysing the generalized theory of the five-cut process and the duplex helical method [22], this paper investigates the different working principles of the cutter tilt angle and the blade angle in the two methods and reveals the major idea of the duplex helical method. Furthermore, the influences of the cutter parameters on the contact characteristics of tooth surfaces in the two processing methods are studied, which provides a theoretical reference for the optimization of machining parameters.

1 DIFFERENT WORKING PRINCIPLES OF CUTTER TILT ANGLE

In this paper, the following definitions are made: the convex side of the gear and the concave side of pinion are the drive sides; the other mating surfaces are the coast sides.

In general, the meshing mode for all types of spiral-bevel and hypoid gears is local conjugate contact (or called 'point contact'). To receive the length crowning between the mating flanks of a bevel gearset, the length curvatures (the curvature is inverse to the radius) of the convex flanks have to be larger than the length curvature of the concave flanks, that is, a pair of tooth surfaces with meshing must have a curvature difference. In addition, the normal vector of the two mating flanks at the reference point should be the same, or the two mating flanks should have equal spiral angle and pressure angle at the reference point. The cutter point radius is a good measure for the tooth length curvature in the five-cut process. To obtain a suitable curvature for a pair of the mating tooth surfaces, an inside cutter point radius for the convex flank must be smaller than an outside cutter point radius for the concave flank. The blade angle in the five-cut process is very similar to the pressure angle of the tooth. If there are some small differences, then they are related to the basic setting adjustments which are done in order to fine-tune the rolling performance. With equal pressure angles, the inside blade (IB) radius at the blade reference point (not at the tip) has to be larger than the outside blade (OB) radius at the reference point, as shown in Fig. 1. In this case, the IB and OB for pinion obviously cannot be mounted on one spread blade head-cutter, which cannot be used in the duplex helical method.

In the duplex helical method, the cutter physically requires a smaller inside point radius and a larger OB radius to be able to mount the IB and OB of the pinion on a head-cutter. Comparing the cutter radii in the two

methods, it can be seen that this is actually equivalent to result in the correct tooth thickness and a very large amount of the length crowning on both sides of the pinion. When machining spiral bevel and hypoid gears, by changing the blade angle simultaneously with the cutter tilt, the large "natural" length crowning can be reduced to the desirable crowning. This is the primary idea of the generalized theory for the duplex helical method. That is, a suitable curvature radius (the curvature radius is the distance from the blade reference point to the cutter axis, perpendicular to the cutting edge) at the reference point can be changed by adjusting the blade angles and the cutter tilt angles, so that the proper length curvature can be obtained on both sides of the pinion.

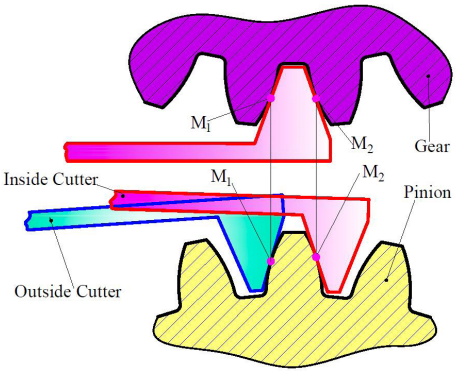

Fig. 1. *Corresponding relationship among cutter radii of gear and pinion*

In the following, how the blade angle and the cutter tilt angle affect the length curvature in the five-cut process and the duplex helical method, respectively and how they meet the required meshing conditions will be analysed. In the five-cut process, the blade angles are very similar to the pressure angles of the gear tooth, especially when the gear is cut with the non-generated method (formate). The pressure angle of the gear at the reference point must be equal to the pressure angle of the mating pinion at the reference point to make the pair of tooth surfaces mesh correctly; the relative position of the gear and pinion cutters can be represented in Fig. 2 at the reference point.

In the five-cut process, the gear cutter generally has the same IB and OB angles, or the OB angle is slightly larger than the IB angle, as shown in Fig. 2. However, in the five-cut process or the duplex helical method, the pinion cutter generally has a smaller OB angle and a larger IB angle. When the cutter tilt is used to process the pinion, the curvature radius of the pinion OB r_{n1} is increased by an amount Δr_{n1} relative

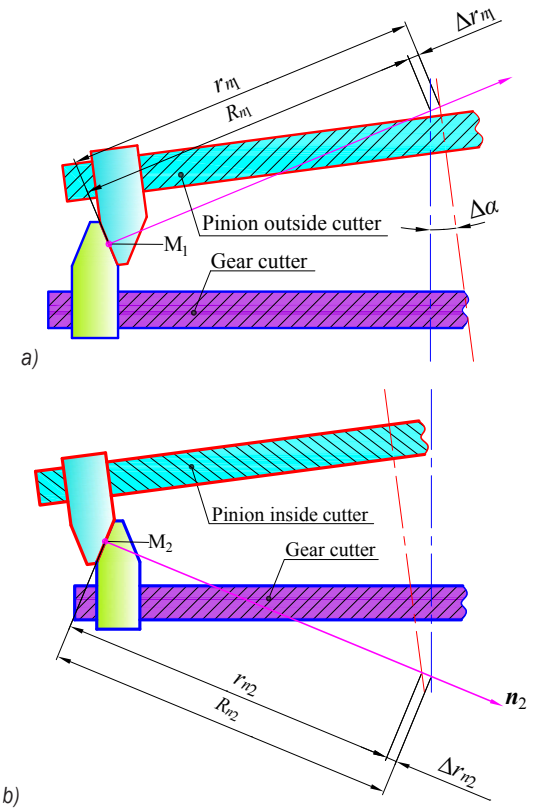

Fig. 2. *Relative position of gear and pinion cutters in five-cut process; a) drive side and b) coast side*

to that of the gear IB R_{n1} on the dive side, that is, $r_{n1}=R_{n1}+\Delta r_{n1}$. The curvature radius of the pinion IB r_{n2} is reduced by an amount Δr_{n2} relative to that of the gear OB R_{n2} on the coast side, that is, $r_{n2}=R_{n2}+\Delta r_{n2}$. The values of Δr_{n1} and Δr_{n2} are determined by the angle $\Delta\alpha$ caused by the tilt of the cutter. Therefore, the cutter tilt in the five-cut process meets precisely the condition that a pair of meshing flanks have a curvature difference. That is, at the reference point, the curvature radius of the concave side must be larger than that of the convex side. In addition, it should be noted that Fig. 2 is drawn under the same mean cutter radius of the gear and the pinion, and the length curvature crowning is performed in the five-cut process (it is equivalent to counter-crowning the cutter radius), which can further reduce the OB radius and increase the IB radius for the pinion, this will cause the curvature difference required for the correct engagement of the two mating flanks to increase further. The above situation is the reason why the OB radius is smaller than the IB radius of the pinion in the five-cut process.

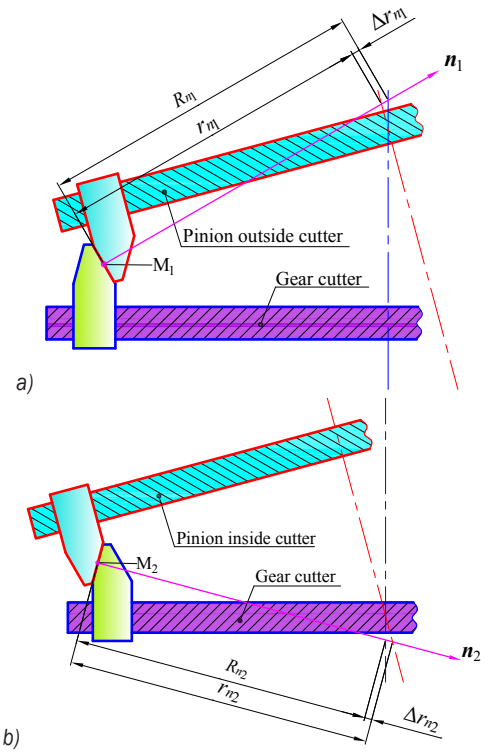

Fig. 3. *Relative position of gear and pinion cutters in duplex helical method; a) drive side and b) coast side*

In the duplex helical method, the spread blade cutter with the smaller IB angle and the larger OB angle are generally chosen to generate the gear and the pinion, and the asymmetry degree between the IB and OB blade angles is larger (the so-called asymmetry degree is the extent to which the IB and OB angles deviate from the mean pressure angle). The reason for this is to control the tooth contact pattern length. A smaller OB angle and a larger IB angle will lengthen the contact pattern, a larger OB angle and a smaller IB angle will shorten the contact pattern. As shown in Fig. 3, when the cutter tilt is used to process the pinion, the curvature radius of the pinion OB r_{n1} is reduced by an amount Δr_{n1} relative to that of the gear IB R_{n1} on the dive side, that is, $r_{n1}=R_{n1}-\Delta r_{n1}$. The curvature radius of the pinion IB r_{n2} is increased by an amount Δr_{n2} relative to that of the gear OB R_{n2} on the coast side, that is, $r_{n2}=R_{n2}+\Delta r_{n2}$. This is equivalent to increasing the concave curvature and reducing the convex curvature for the pinon, and the purpose of effectively reducing the large "natural" length crowning on both sides of the pinion is achieved at the same time, which can satisfy the desirable curvature required for the correct engagement of a gearset.

According to the above analysis, it can be seen that a desirable curvature radius for a pair of mating tooth surfaces can be obtained by the suitable tilt angles and blade angles, and then the different cutter radii required to meet the two processing methods are obtained, which is the essential difference between the five-cut process and the duplex helical method.

2 INFLUENCE RULES OF BLADE ANGLES ON MESHING PERFORMANCE

The selection principle of the blade angles in the five-cut process, and the duplex helical method is significantly different, especially regarding the blade angles of the gear. The tooth contact characteristics are an important indicator of the gearset meshing performance. Therefore, a numerical example of the faced-milled hypoid gearset of the gear ratio 11×45 is considered to investigate the different influences of the blade angle and the cutter radius on meshing performance in the two processing methods. For comparison purposes, the basic design parameters of the hypoid gearset processed by the two methods are as identical as possible, and the HFT (one of the five-cut process, format gear and pinion finished with cutter tilt) and HFDH (one of the duplex helical method, format gear and pinion generated by the duplex helical method) method are used to perform the numerical example, the design parameters are given in Table 1. A computer program is developed to implement the formulation provided above.

Table 1. *Basic design parameters of hypoid gears*

Parameters	Pinion	Gear
Number of teeth	11	45
Module [mm]	-	6
Face width [mm]	44.35	40
Pinion offset [mm]	30	-
Shaft angle [°]	90	-
Mean pressure angle [°]	20	20
Mean spiral angle [°]	48	33.82
Hand of spiral	left	right
Whole depth [mm]	11.89	11.73
Mean cone distance [mm]	125.33	120.98
Outer diameter [mm]	99.68	271.02
Face angle [°]	20.53	74.08
Pitch angle [°]	16.32	73.2
Root angle [°]	15.45	68.87

Based on keeping other machining parameters unchanged (for example, the cutter radius is 114.3 mm), the OB and IB angles of the pinion and gear cutter are changed to investigate the influences of the blade angle on meshing performance in the five-cut process. Fig. 4 shows some of the results of tooth

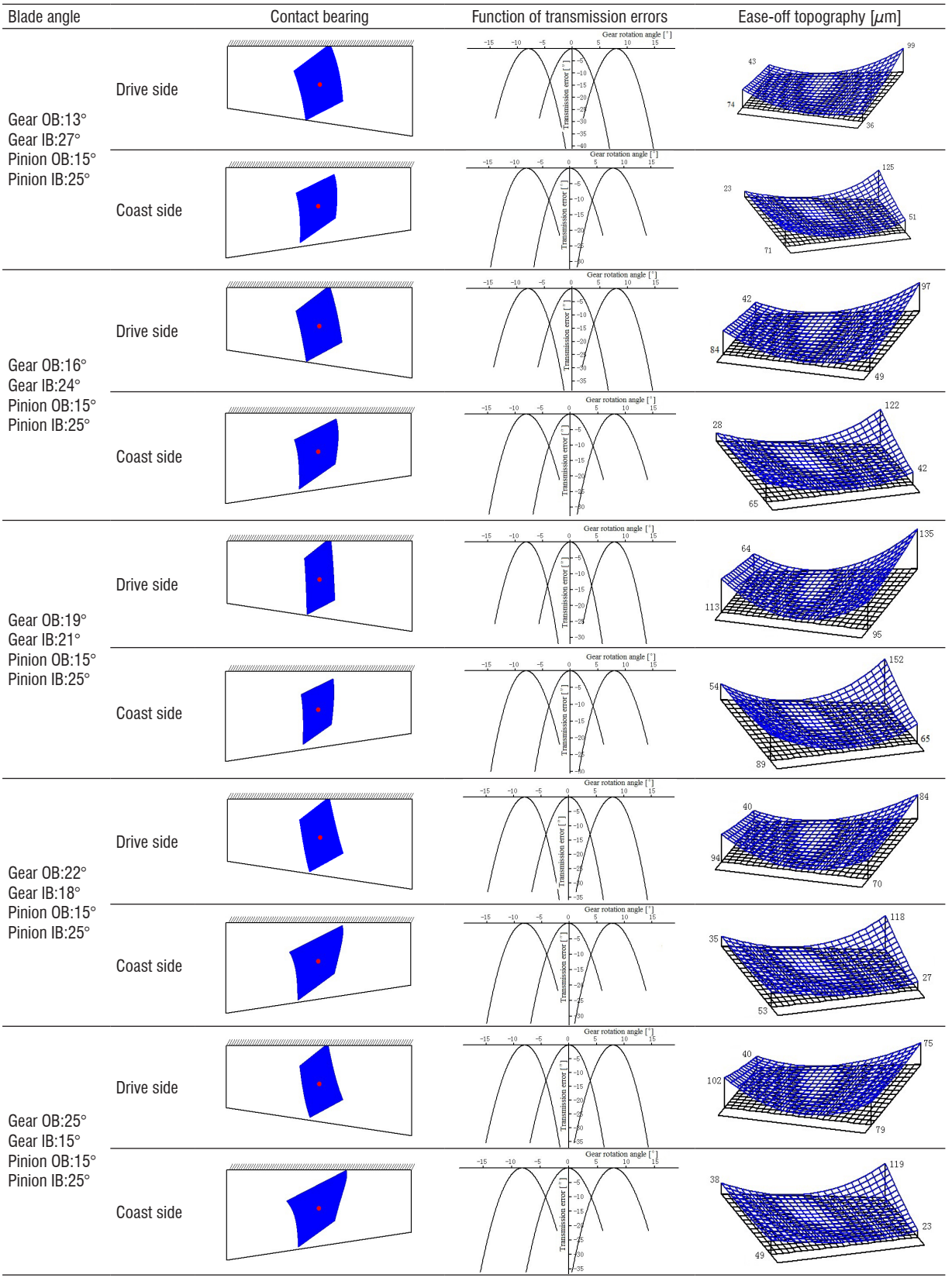

Fig. 4. *TCA results when changing gear blade angles for HFT method*

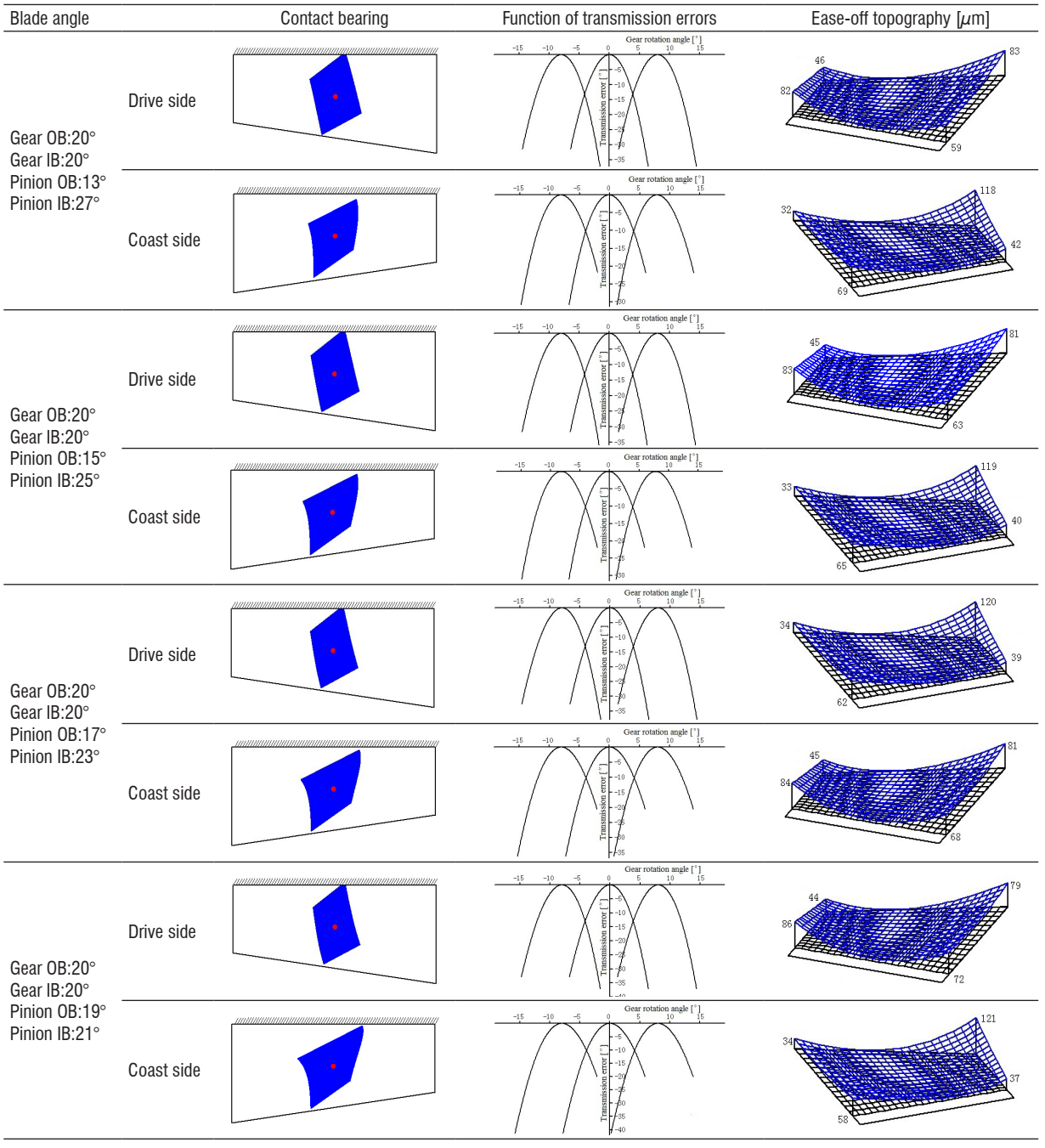

Fig. 5. *TCA results when changing pinion blade angles for HFT method*

surface contact analysis (TCA) when the pinion blade angles remain unchanged, and the gear blade angles change; Fig. 5 shows some of the results of the TCA when the gear blade angles remain unchanged, and the pinion blade angles change. Comparison of results of the TCA in Figs. 4 and 5 have confirmed the following:

(1) As the asymmetry degree of the gear blade angles increases, the length of the contact bearings and the inclination angle of the contact path become larger. The difference of the contact bearing length between the drive side and the coast side becomes significantly larger.

(2) It can be seen from the comparison of different ease-off topographies that the amount of the tooth

surface mismatch increases with the growth of the asymmetry degree for the blade angles.

(3) From the comparison of different transmission error functions, it can be shown that the maximum levels of the transmission error function gradually become larger with the growing of the asymmetry degree for the blade angles, and the maximum levels of the drive side are significantly larger than that of the coast side.

As shown in Figs. 6 and 7, the relationship between the blade angles and the size of the contact bearing is further analysed, it is known that the change of the major axis radius of the contact ellipse has no apparent regularity and the variation tendency of the drive side, and the coast side is different, while the minor axis radius of the contact ellipse has almost no change with the variation of the OB angles for the gear and the unchanged pinion blade angles (OB: 15° and IB: 25°). When the gear blade angles (OB: 20° and IB: 20°) do not change, the major axis radius for the drive side increases, and the coast side decreases substantially with the OB angle of the pinion increasing gradually, while the minor axis radius of the contact ellipse remains approximately unchanged.

The influences of the blade angle on meshing performance in the duplex helical method are investigated with the same analysis method mentioned above, Figs. 8 and 9 show some of the TCA results when the gear and pinion blade angles change respectively, and other head-cutter parameters remain unchanged. Figs. 10 and 11 show the relationship between the contact bearing size and the blade angles. The analysis results obtained are as follows:

(1) Whether with the increase of the OB angles of the gear or the pinion, the length of the contact bearing becomes shorter, which is completely different from the five-cut process and very regular. The slopes of the curves between the drive side and the coast side change only when the OB and IB angles of the gear are 20° (mean pressure angle).

(2) Similar to the five-cut process, the minor axis radius of the contact bearing changes very little, and the minor axis radius of the drive side is larger than that of the coast side.

(3) Compared with the five-cut process, the relationships between the transmission error function, the ease-off topography and the blade angle are more regular. That is, as the OB angle of the gear increases, the maximum level of the transmission error function and the amount of the tooth surface mismatch increase gradually when

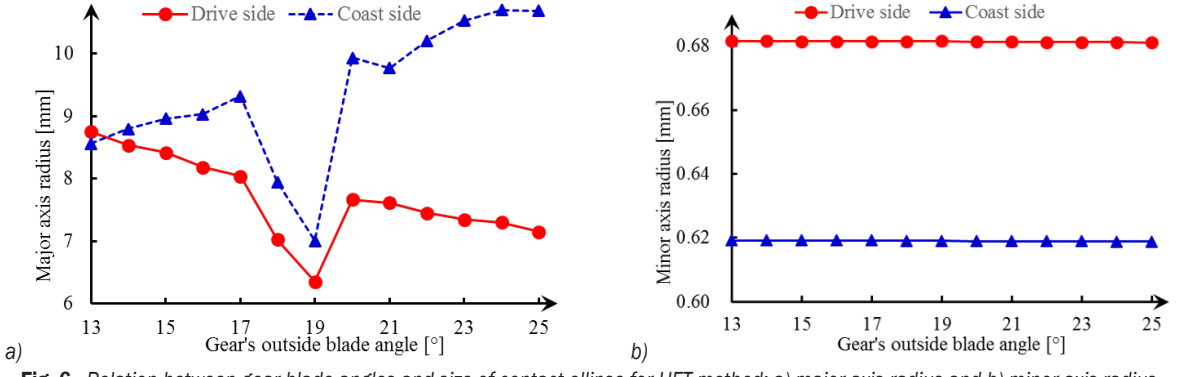

Fig. 6. *Relation between gear blade angles and size of contact ellipse for HFT method; a) major axis radius and b) minor axis radius*

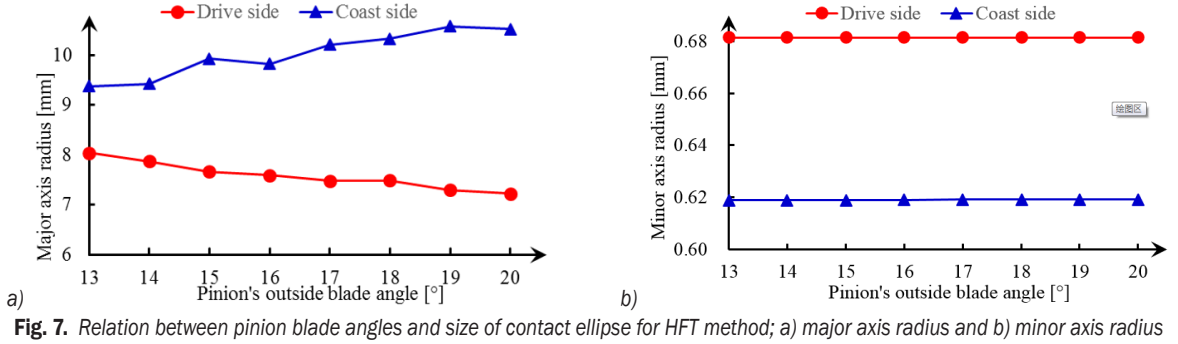

Fig. 7. *Relation between pinion blade angles and size of contact ellipse for HFT method; a) major axis radius and b) minor axis radius*

Blade angle		Contact bearing	Function of transmission errors	Ease-off topography [μm]
Gear OB:13° Gear IB:27° Pinion OB:15° Pinion IB:25°	Drive side	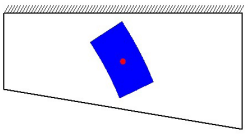	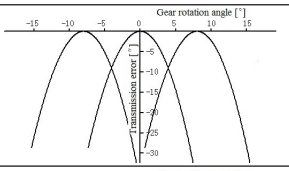	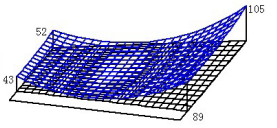
	Coast side	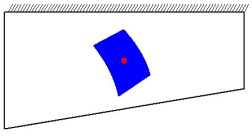	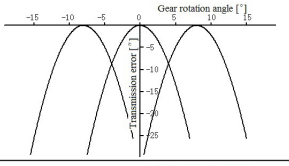	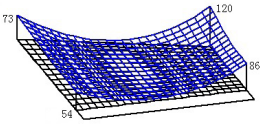
Gear OB:16° Gear IB:24° Pinion OB:15° Pinion IB:25°	Drive side	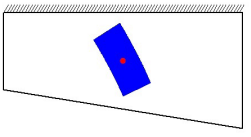	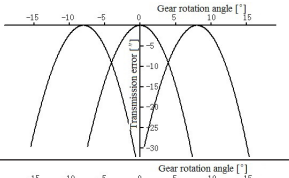	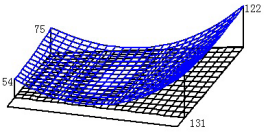
	Coast side	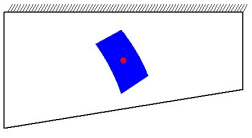	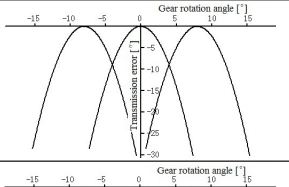	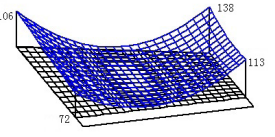
Gear OB:19° Gear IB:21° Pinion OB:15° Pinion IB:25°	Drive side	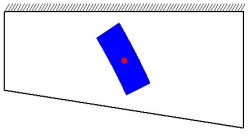	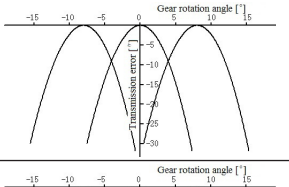	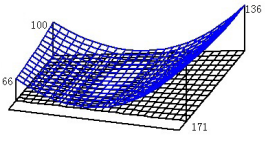
	Coast side	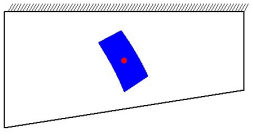	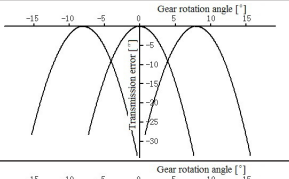	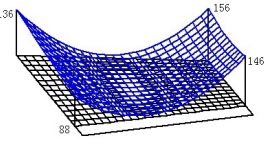
Gear OB:22° Gear IB:18° Pinion OB:15° Pinion IB:25°	Drive side	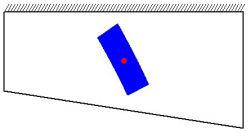	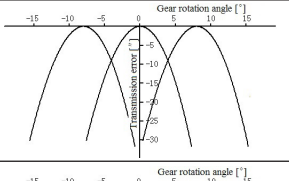	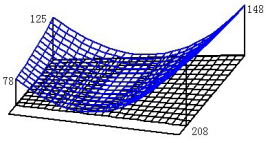
	Coast side	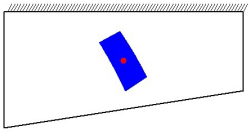	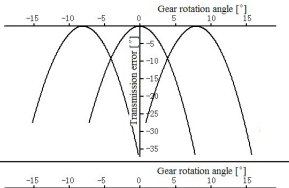	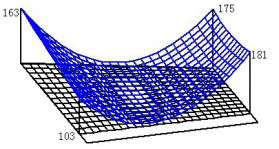
Gear OB:25° Gear IB:15° Pinion OB:15° Pinion IB:25°	Drive side	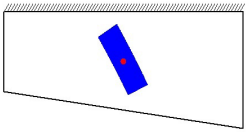	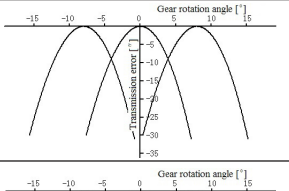	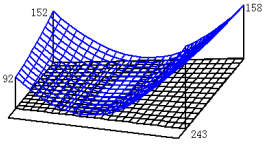
	Coast side	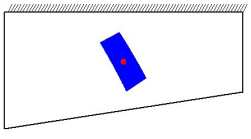	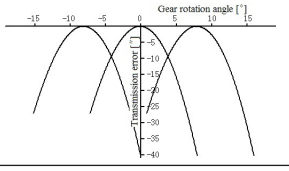	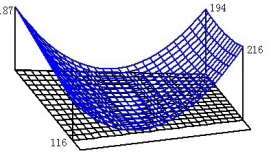

Fig. 8. *TCA results when changing gear blade angles for HFDH method*

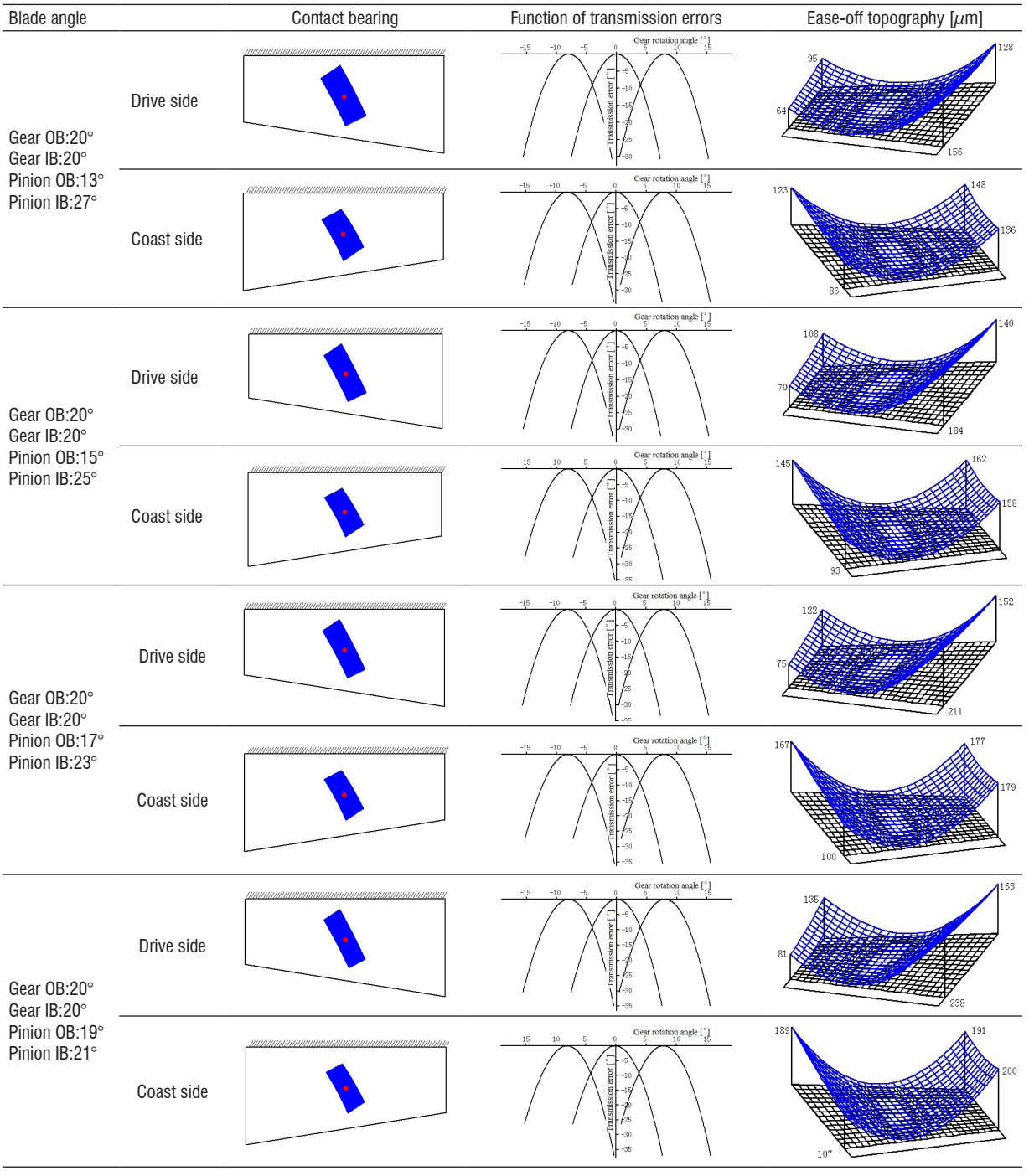

Fig. 9. *TCA results when changing pinion blade angles for HFDH method*

the blade angles of the pinion are constant. The variation trends are similar as above with the increase of the OB angle of the pinion when the blade angles of the gear are unchanged.

Therefore, unlike the five-cut process, the blade angle is an important control parameter for adjusting the size of the contact bearing in the duplex helical method. In general, increasing the asymmetry degree of the IB and OB angles can effectively increase the area of the contact bearing. This is also the reason that the gear and the pinion often can be manufactured by one head-cutter with the same blade angles (for

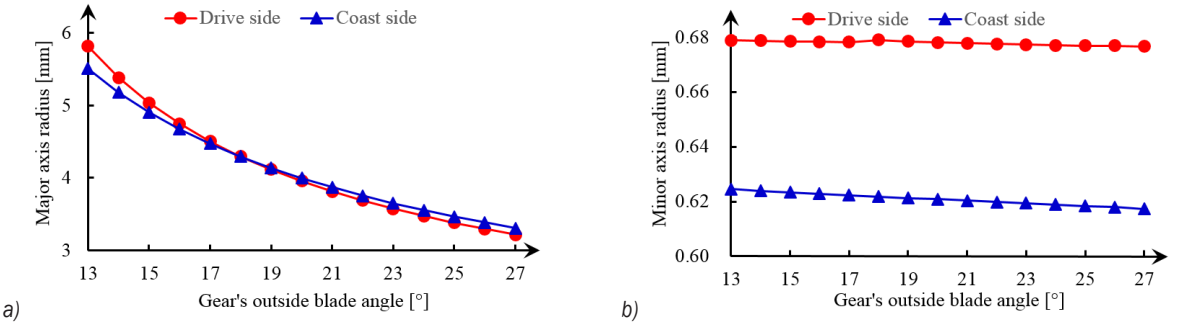

Fig. 10. *Relation between gear blade angles and size of contact ellipse for HFDH method; a) major axis radius and b) minor axis radius*

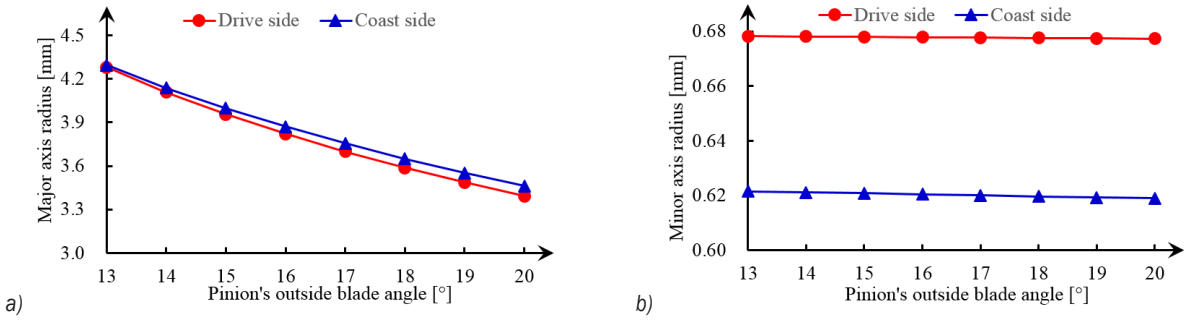

Fig. 11. *Relation between pinion blade angles and size of contact ellipse for HFDH method; a) major axis radius and b) minor axis radius*

example, the OB and IB angle can be 15° and 25° in this numerical example, respectively) and the mean cutter radius.

3 INFLUENCE RULES OF CUTTER RADIUS ON PERFORMANCE

The relationship between the cutter radius and the meshing performance is studied by changing the cutter radius under keeping the blade angles unchanged (Gear OB:20° and IB:20°, Pinion OB:15° and IB:25°) in the two processing methods, respectively. Figs. 12 and 13 show some of the TCA results when the mean cutter radius changes and other head-cutter parameters remain unchanged, Figs. 14 and 15 show the relationship between the contact bearing size and the cutter radius for the five-cut process and the duplex helical method, respectively. The analysis results obtained are as follows:

(1) In the five-cut process, the size, position and direction of the contact bearing and the amount of the tooth surface mismatch have little influence on the cutter radius; only when the cutter radius is less than 114.3 mm does the major axis radius of the contact ellipse become longer with the increase of the cutter radius for the drive side; the coast side is just the opposite, but the minor axis radius of the contact ellipse always changes very little on both surfaces.

(2) In the duplex helical method, the size of the contact bearing increases with the increase of the cutter radius all the time, but the change rates of the drive side and the coast side are different. The amount of the tooth surface mismatch decreases with the increase of the cutter radius.

(3) The influence rules between the maximum level of the transmission error function and the cutter radius are the same in the two processing methods, that is, the maximum level decreases with the increase of the cutter radius, while the coast side is exactly the opposite.

The relationship between the cutter radius and the tooth bending strength is investigated, as shown in Fig. 16; the data in the figure are obtained according to the calculation method of ISO 10300 **[24]**; the comparison and analysis of the tooth bending strength evolution for the two processing methods are as follows:

(1) Except for a few cutter radii, in general, the bending strength of the gear and the pinion decreases with the increase of the cutter radius.

(2) For the gear, the bending strength in the duplex helical method is slightly higher than that in the five-cut process, but the difference between the two methods is very small, which is because the

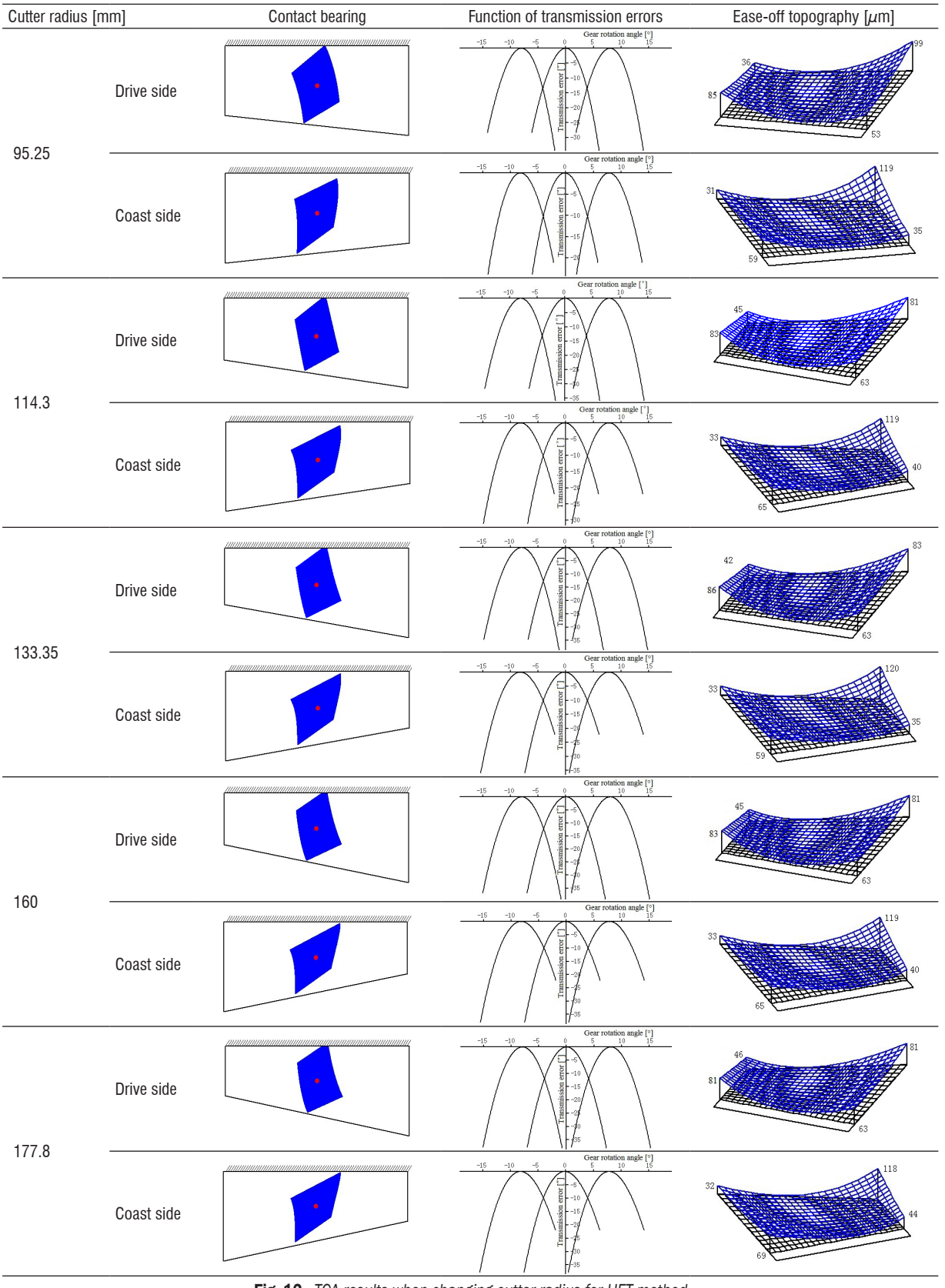

Fig. 12. *TCA results when changing cutter radius for HFT method*

Cutter radius [mm]		Contact bearing	Function of transmission errors	Ease-off topography [μm]
95.25	Drive side	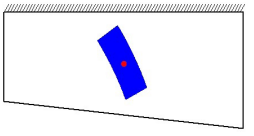	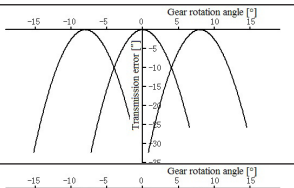	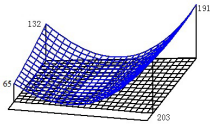
	Coast side	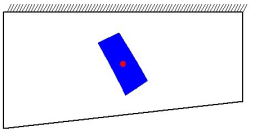	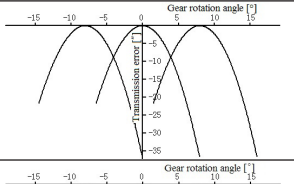	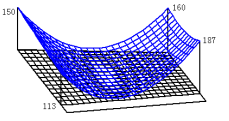
114.3	Drive side	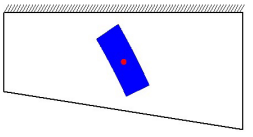	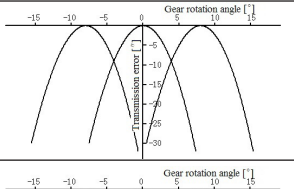	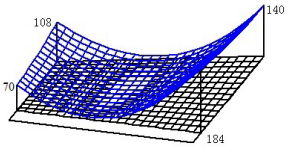
	Coast side	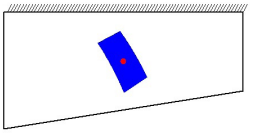	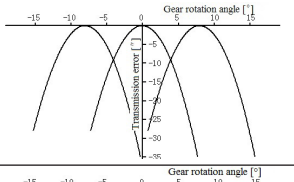	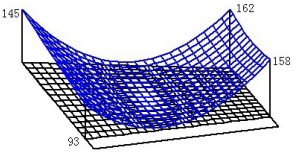
133.35	Drive side	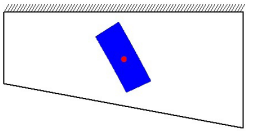	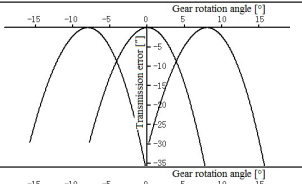	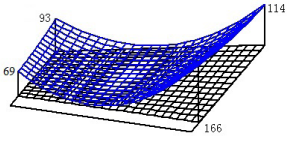
	Coast side	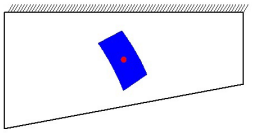	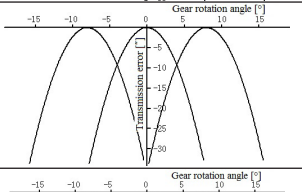	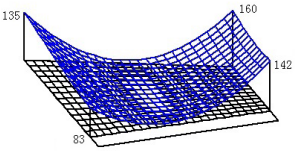
160	Drive side	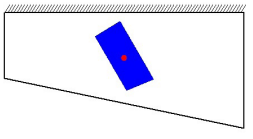	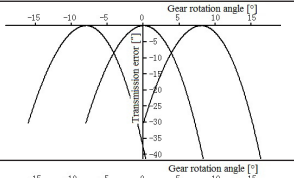	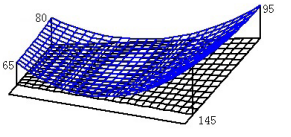
	Coast side	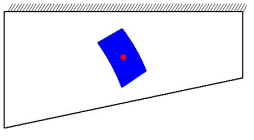	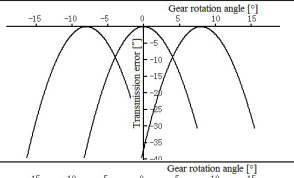	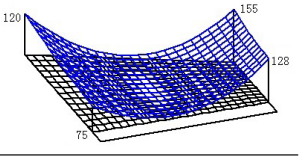
177.8	Drive side	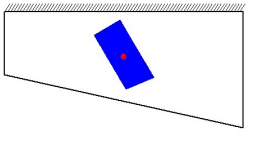	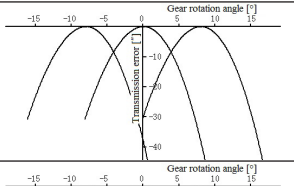	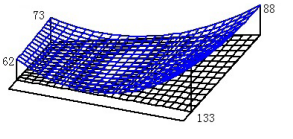
	Coast side	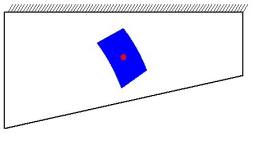	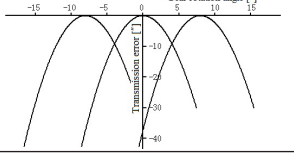	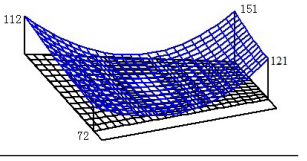

Fig. 13. *TCA results when changing cutter radius for HFDF method*

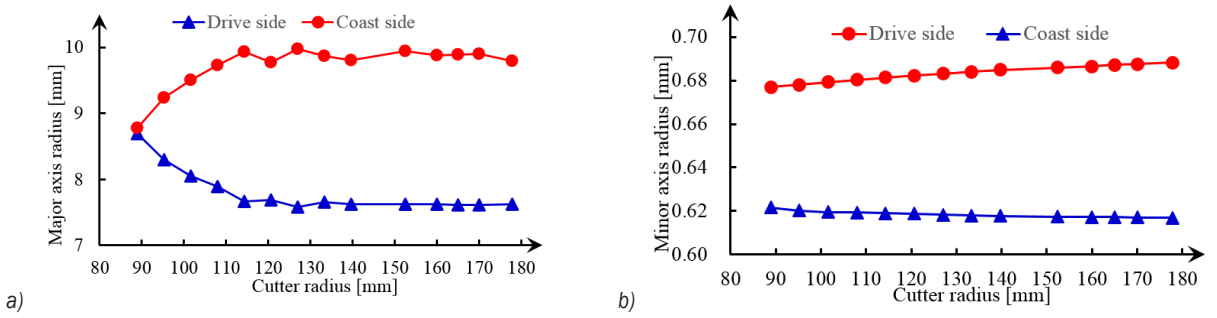

Fig. 14. *Relation between cutter radius and size of contact ellipse for HFT method; a) major axis radius and b) minor axis radius.*

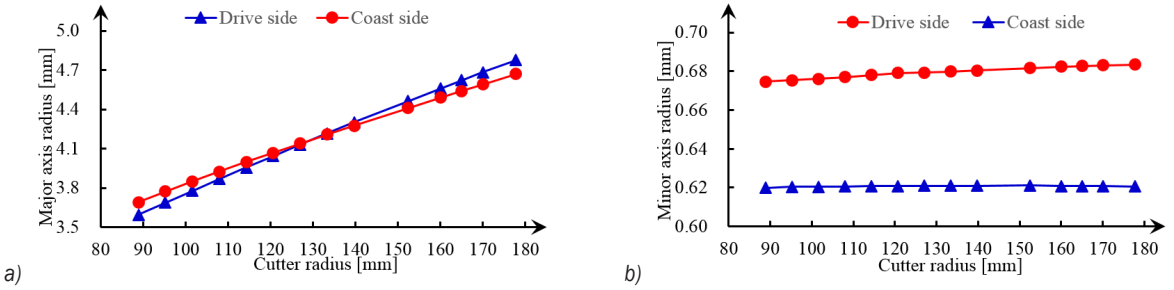

Fig. 15. *Relation between cutter radius and size of contact ellipse for HFDH method; a major axis radius and b) minor axis radius.*

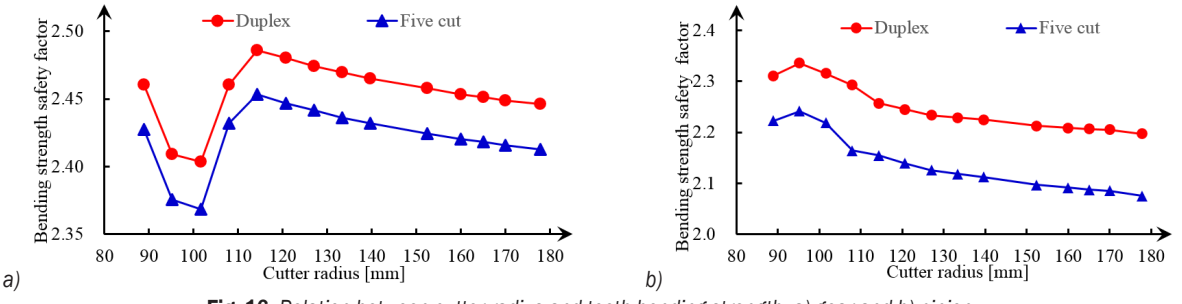

Fig. 16. *Relation between cutter radius and tooth bending strength; a) gear and b) pinion*

gears are all processed by the format in the two processing methods.

(3) For the pinion, the bending strength of the duplex helical method is significantly higher than that of the five-cut process, which is because the slot width has a constant width along lengthwise when the pinion is manufactured with the duplex helical method; the characteristic of the equal slot width ensures that the maximum point width and the maximum cutter edge radius can be used during machining. Therefore, not only the tooth strength can be improved, but also the cutter life can be extended. In addition, both sides of the pinion and gear tooth slots are cut with a single cutter in the duplex helical method; the connection smoothness of the tooth root fillet and the tooth bottom surface is much better than that cut by the five-cut process in actual manufacturing, which also improves the tooth strength of the pinion machined with the duplex helical method.

4 CONCLUSIONS

The following conclusions can be drawn from the performed investigation:

(1) The major idea of the generalized theory for the duplex helical method is revealed by analysing the different working principles of the cutter tilt mechanism in the two processing methods, that is, by changing the OB and IB angles of a spread blade head-cutter simultaneously with the cutter

tilt, the large "natural" length crowning can be reduced, down to the desirable crowning.

(2) Compared with the five-cut process, the influence of the blade angle and the cutter radius on the tooth surface contact characteristics is more regular in the duplex helical method. Therefore, they are often used as important parameters to optimize the meshing performance of spiral bevel and hypoid gears.

(3) In the case of the same design parameters and cutter parameters, the gearset processed by the duplex helical method has higher tooth-bending strength than that processed by the five-cut process; the difference can be up to 2.8 %.

(4) The relationships between the cutter parameters and the contact characteristics of the tooth surface by the five-cut process and the duplex helical method are established and analysed; the research results of this paper provide a theoretical basis for effectively obtaining the optimal machine settings of spiral bevel and hypoid gears.

5 ACKNOWLEDGEMENTS

The authors express their deep gratitude to the National Natural Science Foundation of China (NSFC) (Grant No. 51805555), Hunan Provincial Natural Science Foundation of China (Grant No. 2018JJ2679), Introducing Talent Startup Fund of Central South University of Forestry and Technology of China (Grant No.2016YJ006) for the financial support of the research.

6 REFERENCES

[1] Hu, Z.H., Ding, H., Peng, S.D., Tang, Y., Tang, J.Y. (2019). Numerical determination to loaded tooth contact performances in consideration of misalignment for the spiral bevel gears. *International Journal of Mechanical Sciences*, vol. 151, p. 343-355, **DOI:10.1016/j.ijmecsci.2018.11.014**.

[2] Peng, S.D., Ding, H., Zhang, G., Tang, J.Y., Tang, Y. (2019). New determination to loaded transmission error of the spiral bevel gear considering multiple elastic deformation evaluations under different bearing supports. *Mechanism and Machine Theory*, vol. 137, p. 37-52, **DOI:10.1016/j.mechmachtheory.2019.03.013**.

[3] Zheng, F.Y., Hua, L., Chen, D.F., and Han, X.H. (2016). Generation of noncircular spiral bevel gears by face-milling method. *Journal of Manufacturing Science and Engineering*, vol. 138, no.8, p. 081013, **DOI:10.1115/1.4033045**.

[4] Simon, V.V. (2016). Micro tooth surface topography of face-milled hypoid gears. *Mechanism and Machine Theory*, vol. 104, p. 370-381, **DOI:10.1016/j.mechmachtheory.2016.05.012**.

[5] Wang, J., Kong, L., Liu, B., Hu, X., Yu, X., Kong, W. (2014). The Mathematical Model of Spiral Bevel Gears - A Review. *Strojniški vestnik – Journal of Mechanical Engineering*, vol. 60, no.2, p. 93-105, **DOI:10.5545/sv-jme.2013.1357**.

[6] Davidson, S.R. (2019). Simulation of spiral bevel gear tooth manufacturing to aid in one-piece gear shaft design. *Gear Technology*, no. January/February, p. 70-74.

[7] Stadtfeld, H.J. (2014). *Gleason Bevel Gear Technology*. The Gleason Works, Rochester.

[8] Stadtfeld, H.J. (2015). The basics of gear theory, part 2. *Gear Technology*, no. July, p. 52-58.

[9] Stadtfeld, H.J. (2016). Rules for optimal basic design of bevel gears. *Gear Technology*, no. May, p. 54-62.

[10] Litvin, F.L., Vecchiato, D., Gurovich, E., Fuentes, A., Gonzalez-Perez, I., Hayasaka, K., Yukishima, K. (2005). Computerized developments in design, generation, simulation of meshing, and stress analysis of gear drives. *Meccanica*, vol. 40, no. 3, p. 291-323, **DOI:10.1007/s11012-005-4020-y**.

[11] Fuentes, A., Gonzalez-Perez, I., Litvin, F.L., Hayasaka, K., Yukishima, K. (2007). Determination of basic machine-tool settings for generation of spiral bevel gears from blank data. *Proceedings of the ASME International Design Engineering Technical Conferences and Computers and Information in Engineering Conference*, p. 57-68, **DOI:10.1115/DETC2007-34038**.

[12] Litvin, F.L., Fuentes, A. (2004). *Gear geometry and applied theory (second edition)*. Cambridge University Press, New York.

[13] Fan, Q. (2006). Kinematical simulation of face hobbing indexing and tooth surface generation of spiral bevel and hypoid gears. *Gear Technology*, no. January/February, p. 30-38.

[14] Litvin, F.L., Fuentes, A., Hayasaka, K. (2006). Design, manufacture, stress analysis, and experimental tests of low-noise high endurance spiral bevel gears. *Mechanism and Machine Theory*, vol. 41, no. 1, p. 83-118, **DOI:10.1016/j.mechmachtheory.2005.03.001**.

[15] Fuentes, A., Gonzalez-Perez, I., Litvin, F.L., Hayasaka, K., Yukishima, K. (2005). Design, manufacture, and evaluation of prototypes of low-noise high-endurance spiral bevel gear drives. *Proceedings of ASME International Design Engineering Technical Conferences & Computers and Information in Engineering Conference*, p. 585-595, **DOI:10.1115/DETC2005-84013**.

[16] Simon, V. (2009). Head-cutter for optimal tooth modifications in spiral bevel gears. *Mechanism and Machine Theory*, vol. 44, no. 7, p. 1420-1435, **DOI:10.1016/j.mechmachtheory.2008.11.007**.

[17] Simon, V.V. (2011). Optimal modifications of gear tooth surfaces. *Gear Technology*, no. March/April, p. 62-72.

[18] Ma, Z.H., Han, X.H., Hua, L., Xiong, X.S., Zheng, F.Y. (2016). Influence of cutter diameter on meshing performance in spiral bevel gears. *Journal of Central South University*, vol. 23, no. 1, p. 102-111, **DOI:10.1007/s11771-016-3053-9**.

[19] Gleason Works (1971). *Calculation instructions generated hypoid gears duplex helical method*. The Gleason Works, New York.

[20] Gonzalez-Perez, I., Fuentes, A., Hayasaka, K. (2011). Computerized design and tooth contact analysis of spiral bevel gears generated by the duplex helical method. *ASME International Design Engineering Technical Conferences and*

Computers and Information in Engineering Conference, p. 149-158, **DOI:10.1115/DETC2011-47108**.

[21] Fong, Z.H. (2000). Mathematical model of universal hypoid generator with supplemental kinematic flank correction motions. *ASME Journal of Mechanical Design*, vol. 122, no. 1, p. 136-142, DOI:10.1115/1.533552.

[22] Zhang, Y., Yan, H.Z., Tao, Z. (2015). Computerised design and simulation of meshing and contact of formate hypoid gears generated with a duplex helical method. *Strojniški vestnik - Journal of Mechanical Engineering*, vol. 61, no. 9, p. 523-532, **DOI:10.5545/sv-jme.2015.2627**.

[23] Zhang, Y., Yan, H.Z., Zeng, T., Zeng, Y.Y. (2016). Tooth surface geometry optimization of spiral bevel and hypoid gears generated by duplex helical method with circular profile blade. *Journal of Central South University*, vol. 23, no. 3, p. 544-554, **DOI:10.1007/s11771-016-3101-5**.

[24] ISO 10300-3:2014(E) (2014). *Calculation of Load Capacity of Bevel Gears — Part 3: Calculation of Tooth Root Strength*. International Organization of Standardization, Geneva, **DOI:10.3403/02362607**.

Strojniški vestnik - Journal of Mechanical Engineering 65(2019)6, 366-374
DOI:10.5545/sv-jme.2019.6006
Original Scientific Paper
Received for review: 2019-01-15
Received revised form: 2019-04-13
Accepted for publication: 2019-05-16

Analysis of the Influence Parameters on the Support Structure Stiffness of Large Radial-Axial Bearings

Spasoje Trifković[1] – Nebojša Zdravković[2] – Milomir Gašić[2] – Mile Savković[2] – Goran Marković[2,*]
[1] University of East Sarajevo, Faculty of Mechanical Engineering, Bosnia and Herzegovina
[2] University of Kragujevac, Faculty of Mechanical and Civil Engineering in Kraljevo, Serbia

In certain types of crane and earth-moving machinery, such as portal cranes, loaders and excavators, the transfer of loads to crane tracks or the terrain is accomplished by means of undercarriage frames composed of box-like girders. The hypothesis that all four supports of the undercarriage frame do not lie in the horizontal plane is the basis for the formation of a calculation model. This paper analyses the influence of geometric parameters of box-like girders on the magnitude of additional forces at the supports of those frames when one of the supports is raised or lowered relative to the horizontal plane for the size Δ. Theoretical dependences between moments of inertia and stiffness under bending and torsion of those girders were thus established. Obtained relations leads to more concise forms of expressions for influential coefficients in Maxwell-Mohr integrals and simplifies optimization methods in the design of support structures. With experimental verification of the results, the influences of geometric parameters on the stiffness of the support structure are confirmed, and preconditions are created for further analysis of the connection made by large diameter bearings.

Keywords: support structure, large diameter bearing, box-like girders, geometrical parameters, stiffness, experimental verification

Highlights

- *A calculation method was created for determination of additional forces in the undercarriage frame supports in relation to its geometric parameters and initiative deflection in one support.*
- *The dependence between the ratio of moments of inertia for bending and torsion and the height-width ratio of the box-like cross-section was established.*
- *Dependences were confirmed using the measurement results on the models of undercarriage frames of different geometrical values.*
- *The obtained results lead, to a great extent, to the simplification of optimization methods in the design of carrying structures with box-like girders, and they are the precondition for further analysis of proper functioning of the connection realized by large diameter bearings.*

0 INTRODUCTION

The connections between the undercarriage and upper structure in certain types of cranes and earth-moving machines are accomplished by large diameter bearings, considering the influence of various operational and structural requirements. The purpose of analysing the functioning of these connections in real conditions is to provide an adequate distribution of loads, as well as the reliable and long-lasting operation of large bearings. The main research topics about large slewing bearings are related to empirical investigations and computational analyses of the failure mechanisms and the determination of internal contact load distributions and load capacity **[1]**. Generally, authors use both the analytical and the numerical approach for solving these problems. The detailed review of the former analytical approaches is presented in **[2]** and **[3]**, where both articles offer the calculation models for determination of the contact angle and the carrying capacity of a four contact-point ball bearing.

Modern approaches for computing the load capacity of slewing bearings are based on the finite element method (FEM). These computational methods (**[4]** and **[5]**) include the most influential parameters, such as the raceway/ring deformations, non-parallel ring displacements, and bearing clearances. In general, it has been shown that all of these parameters have a significant role when determining the load capacity of large slewing bearings. Olave et al. **[6]** used two different ways for obtaining the force distribution in four contact-point slewing bearings (FEM analysis and new calculation procedure considering the effect of the structure's elasticity). This analysis shows that the flexibility of the structures must be taken into account during the calculation of load distribution. Authors in **[7]** outline a procedure for the determination of the interferences between balls and raceways in four contact-point slewing bearings due to the manufacturing errors. Therefore, an inadequate hardened raceway depth can cause raceway failure. In contrast, an excessively large hardened raceway depth can increase the overall vibration and production cost.

*Corr. Author's Address: University of Kragujevac, Faculty of Mechanical and Civil Engineering in Kraljevo, Serbia, markovic.g@mfkv.kg.ac.rs

Authors in [8] analysed a three-row roller slewing bearing with a hardened raceway, by using a non-linear spring instead of a solid roller, to quickly obtain the maximum contact load.

Another direction of research leads to the analysis of influences of the undercarriage frame on the slewing bearing operation. Many researchers have found the stiffness of the supporting structure to be a crucial constructional problem of large slewing mechanisms ([9] and [10]). The supporting structure and the bolted connections cannot be ignored when the load distribution and carrying capacity of a slewing bearing are analysed. The effects of supporting structure, bolts number and preload, ball-race contact truncation and bolt-hole backlash on the carrying capacity of the slewing bearing are analysed in [11]. Results show that the fatigue life and carrying capacity of the slewing bearing can be enhanced by appropriately decreasing the supporting structure stiffness. Duval et al. [12] proposed fatigue analysis, taking into account the complex multiaxial stress state and the gradient of material properties, due to the surface treatment of the tracks (induction hardened parts). A method for the fatigue testing of the raceway by using a small sample is presented in [13]. Recent research [14] is directed to additional factors that influence the position of the resultant force exerted by the superstructure on the undercarriage (large excavation or loading forces, the mass of the transported material and ground inclination). Smaller deviations of the centre of the gravity accelerate the wear of the bearing raceway and cause overloading of the bolts that connect the bearing to the supporting elements. For that purpose, the experimental determination of the centre of the gravity of opencast mining machines is presented in [15].

There are not many publications describing the influences of geometrical parameters of the large diameter bearing support structure on its stiffness. Namely, the clearance between one of the undercarriage frame supports and the crane track or the terrain may occur. Hence, the problem of missing contact can appear due to irregularities on the base or, more rarely, errors that arise during manufacturing. As a consequence, there is a redistribution of vertical forces at the supports and the deformation of the carrying structure during exploitation.

In this paper, attention is directed to the creation of a calculation model, used to define theoretical dependences between the geometrical parameters of box-like girders and the magnitude of additional forces at the undercarriage frame supports. Specifically, the magnitude of additional forces directly influences the functioning of large diameter bearings. The research of those relations was carried out to define such stiffness that the deformation of the support surface of the bearing would not exceed recommended values. Along with the experimental verification of the obtained theoretical results, the preconditions for significant simplification of some optimization methods [16] in the design of carrying structures with box-like girders were established.

After the introductory notes and the overview of previous investigations, the calculation model of the undercarriage frame is presented. The next section deals with the box-like section with constant thickness. Firstly, after some approximations, the theoretical dependence between the ratio of bending and torsional stiffness and the height-width ratio of the section is defined. Consequently, after solving the canonical equations and by using MATLAB curve-fitting tools, the influences of change in girders' height-width ratios and change of structure lengths on the additional forces are determined. After this, an experimental verification on a laboratory model of the undercarriage frame is presented. The conclusion section gives the final remarks and the directions for further research.

1 CREATION OF THE CALCULATION MODEL

In the carrying structures of loader bridges, portal cranes and excavators, clearance Δ may occur under one of the supports of undercarriage frames (e.g., under the support C) in relation to the crane track or terrain (Fig. 1). The basic calculation model obtains the form as in Fig. 2b, where we take the reactions X_1 as the force redundant at D and redundant reactions X_2 and X_3 by cutting the structure at an arbitrary interior point. The flexibility coefficients are now interpreted as the relative displacements of the adjacent cross-section.

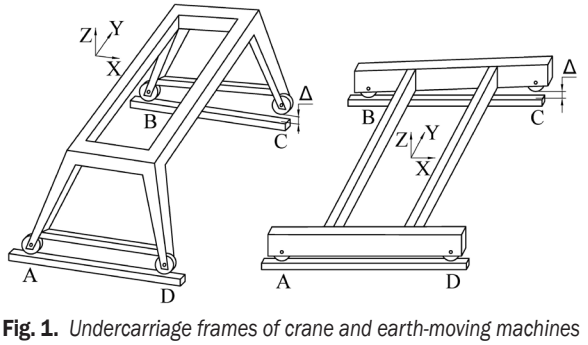

Fig. 1. *Undercarriage frames of crane and earth-moving machines*

The resulting displacements of the primary structure due to the external loading and redundant reactions are expressed as:

$$\sum_{j=1}^{3}\delta_{ij}X_j+\Delta_i=0,\quad i=1,2,3, \tag{1}$$

where δ_{ij} is the flexibility coefficients, X_j the unknown forces and moment, Δ_i the displacement at i due to the external loading in the direction of the restraint at i.

The flexibility coefficients δ_{ij} are determined by the Maxwell-Mohr integral **[17]**:

$$\delta_{ij}=\int_l\frac{M_{ti}M_{tj}}{GI_t}dz+\int_l\frac{M_{xi}M_{xj}}{EI_x}dz+\int_l\frac{M_{yi}M_{yj}}{EI_y}dz+$$
$$+\int_l\frac{N_iN_j}{EA}dz+\int_l\frac{K_xQ_{xi}Q_{xj}}{GA}dz+\int_l\frac{K_yQ_{yi}Q_{yj}}{GA}dz. \tag{2}$$

For the considered case (no axial forces nor horizontal bending, the influence of shear forces is neglected), δ_{ij} has the form:

$$\delta_{ij}=\int_l\frac{M_{ti}M_{tj}}{GI_t}dz+\int_l\frac{M_{xi}M_{xj}}{EI_x}dz, \tag{3}$$

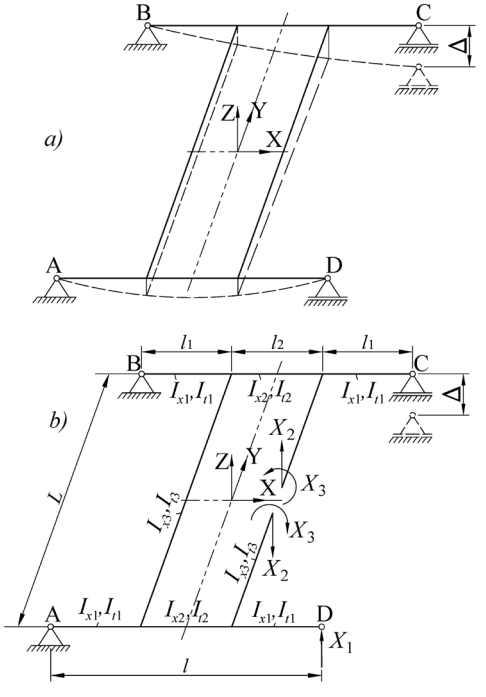

Fig. 2. *Schematic presentation of the undercarriage frame: a) position of the undercarriage frame with the clearance Δ at the support C; b) calculation model of the frame with the unknowns* X_1, X_2 *and* X_3

Integration over the entire contour results in:

$$\delta_{11}=\frac{4l_1^3}{3EI_{x1}}+2\frac{l_1l_2^2}{EI_{x2}}\left(1+l_1/l_2+l_2/3l_1\right)+\frac{l_2^2L}{GI_{t2}},$$
$$\delta_{22}=\frac{2l_2^3}{3EI_{x2}}+\frac{L^3}{6EI_{x3}}+\frac{l_2L^2}{2GI_{t2}},$$

$$\delta_{33}=\frac{2l_2}{EI_{x2}}+\frac{2L}{GI_{t3}},\quad \delta_{12}=\frac{l_2^2\left(3l_1+2l_2\right)}{3EI_{x2}}, \tag{4}$$
$$\delta_{13}=-\frac{l_2\left(2l_1+l_2\right)}{EI_{x2}}-\frac{l_2L}{GI_{t3}},\quad \delta_{23}=-\frac{l_2^2}{EI_{x2}},$$

As can be seen from Eq. (4), bending stiffness (EI) and torsional stiffness (GI_t) figure in some of them. By establishing the theoretical dependence between them, Eq. (4) would obtain a more concise form, which would simplify the analysis below.

2 THEORETICAL DEPENDENCE OF THE RATIO OF BENDING AND TORSIONAL STIFFNESS OF BOX-LIKE GIRDERS

The moment of inertia of the box-like cross-section (Fig. 3) with constant thicknesses of horizontal and vertical plates δ, for the axis x, is defined by the expression:

$$I_x=2\frac{\delta\left(h+\delta\right)^3}{12}+2\left[\frac{\left(b-\delta\right)\delta^3}{12}+\delta\left(b-\delta\right)\frac{h^2}{4}\right]. \tag{5}$$

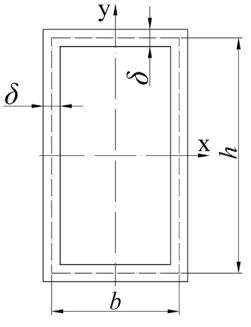

Fig. 3. *Section of the box-like girder with constant plate thickness*

Further, if the height of the box-like girder h is expressed through the width b, i.e., if the coefficient $k=h/b$ is introduced, by neglecting the members in which δ^3 and δ^4 *(δ <<b; δ <<h)*, then the expression for the moment of inertia of the cross-section of the box-like girder Eq. (5) can be written in the form:

$$I_x^{'}=\frac{k^2\delta b^3}{6}(k+3). \tag{6}$$

Since the thicknesses of the plates are equal, the torsional moment of inertia can be written in the following form:

$$I_t = \frac{2b^2h^2\delta^2}{b\delta + h\delta} = \frac{2k^2\delta b^3}{1+k}. \quad (7)$$

Now, the following relation can be formed:

$$\frac{I_x^{'}}{I_t} = i^{'} = \frac{k^2+4k+3}{12}. \quad (8)$$

The same relation with the exact value for I_x (Eq. (5)) is designated as $i = I_x/I_t$. Eq. (8) has a parabola shape. Since the real values for k are within the interval between 1 and 3, it can be approximated with a linear polynomial which gives the lowest deviations. This was obtained with the MATLAB software package and its incorporated tools for approximation. A set of arranged pairs (k, i) is defined with a step 0.5 for k (Table 1). For the given first degree of the polynomial, the following is obtained:

$$i = i(k) = 0.667k - 0.048. \quad (9)$$

The relative deviations at the corresponding points during the approximation by a first degree polynomial are also given in Table 1.

Table 1. *Set of arranged pairs* (k, i)

Reference point	k	$i = i(k)$	Approximation error [%]
1	1.0	0.667	−6.291
2	1.5	0.937	1.481
3	2.0	1.250	2.778
4	2.5	1.604	0.866
5	3.0	2.00	−2.430

By neglecting the free member due to its small value, Eq. (9) obtains the following form:

$$i = i(k) \approx \frac{2}{3}k. \quad (10)$$

The relative error made by this transformation does not exceed 6.5 %. The approximation is confirmed for the cross section of the real box-like girders with characteristics: b = 30 cm; δ = 0.8 cm and 1.0 cm and k = 1.0, 1.5, 2.0, 2.5, 3.0 (Table 2).

It can be shown that even for larger plate thicknesses (over 1 cm), the percentage deviation from exact values of the ratio does not exceed 8 %. By analysing the values from Table 2, it can be concluded that the approximation is acceptable not only for practical but also for theoretical usage.

Regarding the theoretical dependence (Eq. (10)), it is also possible to establish the approximate dependence between bending stiffness (EI_x) and torsional stiffness (GI_t) of the box-like girder:

$$\frac{EI_x}{GI_t} = \frac{2(1+\nu)GI_x}{GI_t} = \frac{2(1+0.3)I_x}{I_t} \approx \sqrt{3}k. \quad (11)$$

The defined ratio of the bending stiffness and the torsional stiffness of box-like girders (Eq. (11)) is important for the optimization of the crane and earth-moving machinery carrying structures. It enables creating the compact analytical models, suitable for application of the optimization methods, which provide the solution with increased bending and torsional stiffness, along with the mass reduction.

2.1 Additional Forces at the Supports of Undercarriage Frames

The solution of the canonical equations (Eq. (1)) contains the value of the additional force X_1 at support D, caused by the lowering of the support C by a value Δ (Fig. 2).

Table 2. *Exact and approximate ratio values*

δ [cm]	k	Exact values			Approximate values			$2k/3$	p [%]
		I_x	I_t	$i = I_x/I_t$	I_x'	I_x'/I_x	$i' = I_x'/I_t$		
		1	2	3	4	5	6	7	8
0.8	1.0	536.7	800.0	0.671	533.3	0.993	0.666	0.666	0.64
	1.5	2354.7	1440.0	0.940	1350.0	0.996	1.250	1.000	−6.29
	2.0	2672.6	2133.3	1.252	2666.6	0.997	1.250	1.333	−6.42
	2.5	4590.6	2857.1	1.606	4583.3	0.998	1.600	1.666	−3.73
	3.0	7208.5	3600.0	2.002	7200.0	0.998	2.000	2.000	0.11
1.0	1.0	673.3	1000.0	0.673	666.6	0.990	0.666	0.666	0.99
	1.5	1696.6	1800.0	0.942	1687.5	0.994	0.937	1.000	-6.09
	2.0	3345.0	2666.6	1.254	3333.3	0.996	1.250	1.333	-6.29
	2.5	5473.3	3571.4	1.608	5729.1	0.997	1.604	1.666	-3.64
	3.0	9016.6	4500.0	2.000	9000.0	0.998	2.000	2.000	0.18

At the same time, due to the symmetry, the reactions at the supports A and C will be decreased by the same value X_1.

In real structures, girders 1 and 2 (Fig. 2) are identical, i.e., $I_{x1} = I_{x2}$, $I_{t1} = I_{t2}$. Further on, the bending moment of inertia of the girder 3 can be expressed in relation to the bending moment of inertia of the girder 2 by coefficient ε: $I_{x3} = \varepsilon I_{x2}$. Considering Eq. (10) and the same value of parameter k for the whole structure, it is also $I_{t3} = \varepsilon I_{t2}$.

Considering Eq. (11) and having in mind that $\Delta_1 = -\Delta$ and $\Delta_2 = \Delta_3 = 0$, the canonical Eqs. (1) obtain the following form:

$$\begin{aligned}
&\left[\frac{4l_1^3}{3}+2l_1l_2^2\left(1+\frac{l_1}{l_2}+\frac{l_2}{3l_1}\right)+l_2^2L\sqrt{3k}\right]\frac{X_1}{\Delta EI_{x2}}+\\
&+\left[\frac{l_2^2(3l_1+2l_2)}{3}\right]\frac{X_2}{\Delta EI_{x2}}-\left[l_2(2l_1+l_2)+\frac{\sqrt{3}l_2Lk}{\varepsilon}\right]\frac{X_3}{\Delta EI_{x2}}=1,\\
&\left[\frac{l_2^2(3l_1+2l_2)}{3}\right]\frac{X_1}{\Delta EI_{x2}}+\left[\frac{2l_2^3}{3}+\frac{L^3}{6\varepsilon}+\frac{l_2L^2\sqrt{3k}}{2}\right]\frac{X_2}{\Delta EI_{x2}}-\\
&-\left[l_2^2\right]\frac{X_3}{\Delta EI_{x2}}=0,\\
&\left[l_2(2l_1+l_2)+\frac{\sqrt{3}l_2Lk}{\varepsilon}\right]\frac{X_1}{\Delta EI_{x2}}-\left[l_2^2\right]\frac{X_2}{\Delta EI_{x2}}+\\
&+\left[2l_2+\frac{2\sqrt{3}Lk}{\varepsilon}\right]\frac{X_3}{\Delta EI_{x2}}=0,
\end{aligned} \tag{12}$$

The further analysis is carried out for the real undercarriage frame structures (Fig. 4), with changeable lengths (L = 4.0 m, 4,5 m, 5.0 m, 5.5 m, 6.0 m) and values of coefficients ε (1.0, 1.5, 2.0) and k (range between 1 and 3).

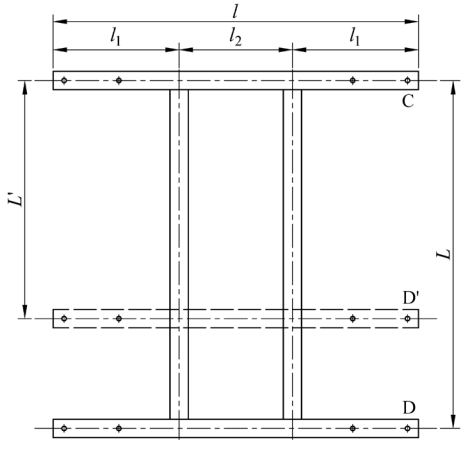

Fig. 4. *Geometrical parameters of undercarriage frames*

Solving of Eqs. (12) leads to the values of additional forces $X_{1(j)}$ and $X_{1(i)}$, whose ratio will be investigated due to the change of length L and mentioned parameters.

Calculated solutions of Eqs. (12) for all cases are given in Table 3 in the form $(X_1/\Delta EI_{x2})10^3$, based on which the further numerical analyses are conducted. Firstly, the results shown in Table 3 are used to establish the dependence of ratio $X_{1(j)}/X_{1(i)}$ as a function of the ratio k_j/k_i, and secondly to establish dependence of ratio $X_{1(j)}/X_{1(i)}$ as a function of the ratio of the length L_i/L_j.

Within the investigation with changeable k, the ratio between additional force reactions for arbitrary cases j and i, regarding Eq. (6), is calculated as:

$$\frac{X_{1(j)}}{X_{1(i)}}=\frac{X_1(k_j)}{X_1(k_i)}=\frac{\left[\dfrac{X_{1(j)}}{\Delta EI_{x2}(k_j)}\right]_{tab}}{\left[\dfrac{X_{1(i)}}{\Delta EI_{x2}(k_i)}\right]_{tab}}\cdot\frac{k_j^2(k_j+3)}{k_i^2(k_i+3)}. \tag{13}$$

For the second analysis with changeable length, there was no need for such conversion since coefficient k is the same for cases j and i, so the ratio of forces is calculated only by the values from Table 3.

After numerical analysis conducted in MATLAB software and its curve fitting tools, with the neglected influence of coefficient ε, the following dependences were established:

$$\frac{X_{1(j)}}{X_{1(i)}}\approx\left(\frac{k_j}{k_i}\right)^{\sqrt{3}}. \tag{14}$$

$$\frac{X_{1(j)}}{X_{1(i)}}=\frac{X_1(L_j)}{X_1(L_i)}\approx\left(\frac{L_i}{L_j}\right)^{0.6739}. \tag{15}$$

3 EXPERIMENTAL ANALYSIS

Experimental analysis was carried out in the laboratory of the Centre for Construction and Transportation Machinery at the Faculty of Mechanical and Civil Engineering in Kraljevo, Serbia. The primary measurements in the experiment were the additional forces at the support D at different deflections Δ at the support C, for two undercarriage frame models (Fig. 4). All activities during the test should be in the field of elastic material behaviour.

3.1 Object of Testing

The testing models of undercarriage frames consist of square pipes of the unique wall thickness of 2.8 mm, with the cross sections $b \times h$ = 60 mm × 60 mm and b

Table 3. *Solutions of canonical Eqs. (12) for different parameters*

k	$(X_1/\Delta EI_{x2})10^3$														
	L=4.0			L=4.5			L=5.0			L=5.5			L=6.0		
	$\varepsilon=1.0$	$\varepsilon=1.5$	$\varepsilon=2.0$	$\varepsilon=1.0$	$\varepsilon=1.5$	$\varepsilon=2.0$	$\varepsilon=1.0$	$\varepsilon=1.5$	$\varepsilon=2.0$	$\varepsilon=1.0$	$\varepsilon=1.5$	$\varepsilon=2.0$	$\varepsilon=1.0$	$\varepsilon=1.5$	$\varepsilon=2.0$
1.000	27.068	24.745	23.914	25.485	23.087	22.214	24.140	21.684	20.780	22.972	20.475	19.547	21.942	19.417	18.473
1.100	25.888	23.471	22.590	24.347	21.872	20.958	23.035	20.519	19.582	21.894	19.352	18.401	20.888	18.331	17.371
1.200	24.829	22.340	21.422	23.325	20.794	19.852	22.042	19.486	18.528	20.927	18.358	17.392	19.942	17.371	16.403
1.250	24.337	21.821	20.888	22.850	20.299	19.347	21.582	19.012	18.047	20.479	17.902	16.932	19.504	16.931	15.961
1.300	23.869	21.328	20.383	22.398	19.830	18.869	21.143	18.563	17.592	20.051	17.470	16.498	19.087	16.514	15.545
1.400	22.993	20.415	19.450	21.554	18.961	17.987	20.324	17.731	16.754	19.254	16.671	15.697	18.309	15.744	14.778
1.500	22.190	19.586	18.608	20.779	18.173	17.191	19.573	16.977	15.998	18.523	15.947	14.976	17.597	15.047	14.087
1.600	21.449	18.828	17.842	20.064	17.453	16.468	18.880	16.289	15.312	17.850	15.287	14.322	16.941	14.413	13.462
1.700	20.762	18.133	17.142	19.402	16.793	15.808	18.240	15.659	14.686	17.229	14.684	13.726	16.337	13.833	12.892
1.750	20.437	17.806	16.814	19.089	16.483	15.499	17.937	15.363	14.393	16.935	14.400	13.447	16.051	13.560	12.626
1.800	20.123	17.492	16.499	18.787	16.185	15.202	17.645	15.079	14.112	16.652	14.128	13.180	15.776	13.299	12.371
2.000	18.969	16.348	15.358	17.677	15.100	14.129	16.573	14.046	13.097	15.613	13.141	12.215	14.768	12.352	11.451
2.100	18.445	15.834	14.849	17.173	14.614	13.650	16.087	13.584	12.644	15.143	12.699	11.785	14.313	11.930	11.042
2.200	17.952	15.354	14.374	16.700	14.160	13.205	15.630	13.152	12.224	14.702	12.288	11.386	13.886	11.536	10.662
2.250	17.716	15.125	14.149	16.473	13.944	12.993	15.412	12.947	12.024	14.492	12.092	11.197	13.682	11.349	10.482
2.275	17.600	15.014	14.039	16.363	13.838	12.890	15.306	12.847	11.927	14.389	11.997	11.105	13.583	11.258	10.394
2.400	17.047	14.481	13.516	15.832	13.335	12.400	14.795	12.370	11.464	13.896	11.542	10.667	13.107	10.824	9.978
2.450	16.836	14.279	13.318	15.630	13.145	12.214	14.601	12.189	11.289	13.709	11.370	10.502	12.926	10.660	9.821
2.475	16.732	14.181	13.221	15.530	13.052	12.124	14.505	12.101	11.204	13.617	11.286	10.421	12.838	10.579	9.744
2.500	16.630	14.083	13.126	15.433	12.960	12.034	14.411	12.014	11.120	13.527	11.204	10.341	12.751	10.500	9.669
2.600	16.235	13.708	12.759	15.054	12.606	11.691	14.048	11.679	10.797	13.177	10.885	10.036	12.414	10.197	9.379
2.625	16.139	13.617	12.671	14.963	12.521	11.608	13.960	11.598	10.719	13.093	10.808	9.962	12.332	10.123	9.309
2.700	15.859	13.353	12.413	14.695	12.272	11.367	13.704	11.362	10.493	12.846	10.584	9.748	12.094	9.910	9.106
2.750	15.678	13.182	12.248	14.522	12.111	11.213	13.538	11.211	10.347	12.686	10.440	9.611	11.941	9.773	8.976
2.800	15.501	13.017	12.087	14.353	11.955	11.062	13.376	11.063	10.205	12.531	10.300	9.477	11.791	9.640	8.849
2.925	15.077	12.621	11.703	13.949	11.583	10.703	12.989	10.711	9.869	12.159	9.967	9.159	11.434	9.322	8.548
3.000	14.834	12.395	11.484	13.717	11.371	10.499	12.767	10.511	9.677	11.947	9.777	8.979	11.230	9.142	8.377

$\times$ h = 60 mm $\times$ 120 mm. The dimensions of the tested models (1200 mm $\times$ 1200 mm and 1200 mm $\times$ 800 mm) are approximately five times smaller than those in real undercarriage frames.

3.2 Test Stand

To carry out the experiment, it was necessary to make a rigid platform (2) (Fig. 5), to which the undercarriage frame (1) is attached. The drilled holes (Ø26 mm) are used for supporting the support brackets (3) and dynamometer (5). Forces at the support D are measured by a dynamometer, due to a deflection at the support C which is set by the presser with a screwed spindle (4). The values of deflection (displacement) at the support C are measured with a comparator (6). Possible height deviations of the upper surfaces of the longitudinal and cross girders can be cancelled by means of the support brackets, which have the possibility of adjusting the upper surfaces of the supporting frames, so that they lie in the horizontal plane. It should be noted that normal, hot-rolled UNP-100 profiles were used for longitudinal and cross girders in acc. to EN 10025:2005 **[18]**.

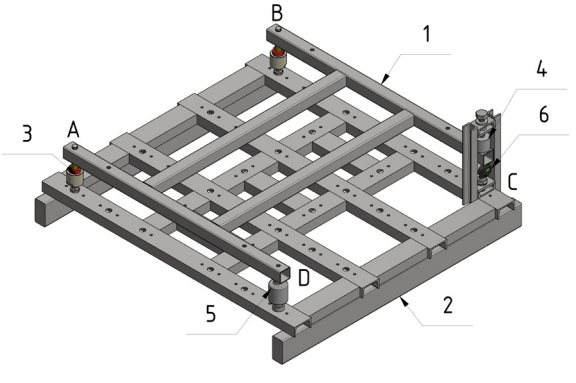

Fig. 5. *Connection between the undercarriage frame model (1) and the rigid platform (2)*

The undercarriage frame supports (Fig. 6a) are designed in such a way as to provide turning of the frame ends, thanks to the extension (3) in the shape of a ball. The body (1) with the nuts (4) is firmly attached to the rigid platform (5). The nuts have the role of levelling the upper surface of the undercarriage frame. The separation of the ball rod from the body of the ball-like support (1) is prevented by a conical sleeve (2).

The support C (Fig. 6b) is compiled of two girders (3) with an upper (1) and a lower traverse (2), thus making a closed type frame. The upper traverse in its middle part has a bushing with a thread, and the presser with a small pitch thread passes through it. By turning the presser (4), via the pad (10), the end of the undercarriage frame (9) at point C is lowered by a given value of clearance Δ.

The lower traverse of the closed frame (2) has an opening for a permanent joint with the rigid platform by means of the threated rod (5), the washer (6) and the nut (7), which, on its upper part, has a drilled hole which serves as the seat of the device (8) for measuring displacements.

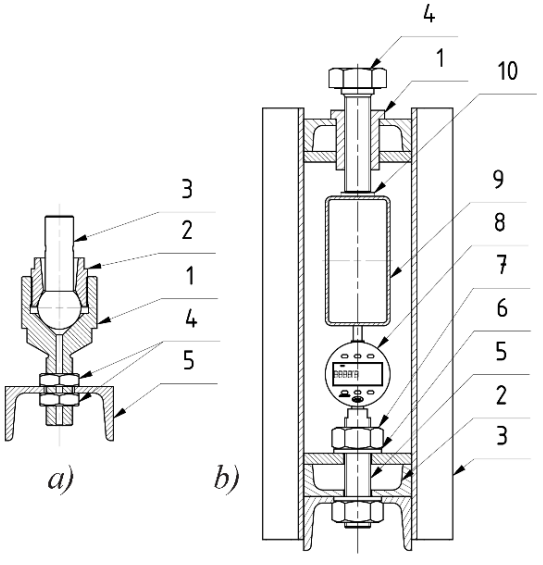

Fig. 6. *Ball-like support of the undercarriage frame and the presser with a screwed spindle*

3.3 Testing Procedures

Registration of force at the support is provided using the force transducer 5, Flintec RC3D30 (with a capacity of 300 kN and sensitivity 2 %) and alphanumeric display 10 (Fig. 7). Displacement of the girder is registered by the standard dial indicator Mitutoyo 2046SB (range 10 mm, accuracy ±13 μm, graduation ±0.01 mm). To obtain accurate measurement results, the testing of the elastic material behaviour of the model and calibration procedure of dial indicator are performed. The girder is exposed by setting the displacement of the support C, which is entered manually for 3 mm. The procedure is repeated several times after which the girder is completely unloaded. That displacement which acts on the force converter, whose intensity is read on the alphanumeric display.

All mentioned activities show that a model of undercarriage frame exhibits elastic material behaviour. Displacements Δ_C (deflection at the support C) were set with a step of 0.5 mm. Measurements were performed on the four models of undercarriage frames:

1. $l \times L = 1200$ mm $\times$ 1200 mm, $l_2 = 400$ mm, $b \times h \times \delta = 60$ mm $\times$ 60 mm $\times$ 2.8 mm ($k = 1$)
2. $l \times L = 1200$ mm $\times$ 1200 mm, $l_2 = 400$ mm, $b \times h \times \delta = 60$ mm $\times$ 120 mm $\times$ 2.8 mm ($k = 2$)
3. $l \times L = 1200$ mm $\times$ 800 mm, $l_2 = 400$ mm, $b \times h \times \delta = 60$ mm $\times$ 60 mm $\times$ 2.8 mm ($k = 1$)
4. $l \times L = 1200$ mm $\times$ 800 mm, $l_2 = 400$ mm, $b \times h \times \delta = 60$ mm $\times$ 120 mm $\times$ 2.8 mm ($k = 2$)

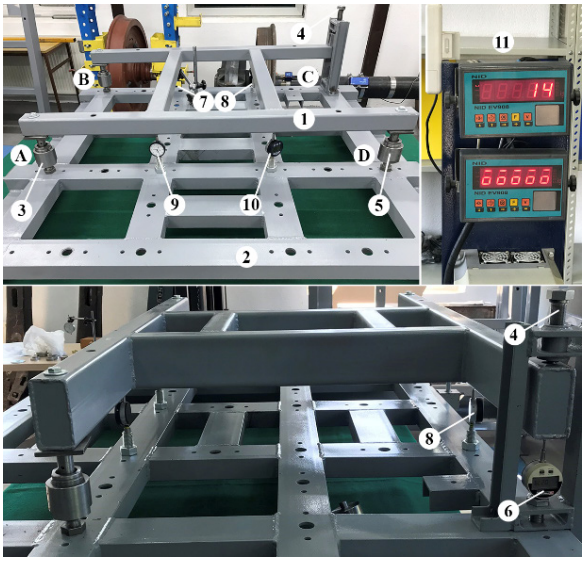

Fig. 7. *Test stand: 1 frame model, 2 rigid platform, 3 ball-like support, 4 presser; 5 force transducer, 6 to 10 comparator; 11 alphanumeric display*

Comparators 7 to 10 are used for some additional deflection measurements and are not included in this research. The testing procedure for all models is repeated 5 times, whereas the repeatability of results for displacements is ±0.01 mm. The final value was obtained as the mean of the measured sizes.

3.4 Measurement Results

The measured values of force X_1 at the support D for all four tested models are shown in Table 4. These measurements were taken for the stepped deflection in support C ($\Delta = 0.5$ mm, 1.0 mm, 1.5 mm and 2.0 mm).

Table 4. *Values of additional force at the supports D for test models with $k = 1$*

Δ [mm]	0.5	1.0	1.5	2.0
X_1' [N]	32	64	96	128
X_1 [N]	26	50	74	101
$l \times L = 1200$ mm $\times$ 1200 mm, $b \times h \times \delta = 60$ mm $\times$ 60 mm $\times$ 2.8 mm $l \times L' = 1200$ mm $\times$ 800 mm; $k_1 = 1$, $\varepsilon = 1$				

Table 5. *Values of additional force at the supports D for test models with $k = 2$*

Δ [mm]	0.5	1.0	1.5	2.0
X_1' [N]	110	224	325	431
X_1 [N]	85	172	249	350
$l \times L = 1200$ mm $\times$ 1200 mm, $b \times h \times \delta = 60$ mm $\times$ 120 mm $\times$ 2.8 mm $l \times L' = 1200$ mm $\times$ 800 mm; $k_2 = 2$, ε=1				

The analysis of the measurement results presented in Tables 4 and 5 provides the following dependences:

- The ratio of the additional forces X_1'/X_1 at the support D, during the change of the coefficient k (k_1=1 and k_2=2), for both values of length is within the range between 3.27 and 3.50; the calculation result of the obtained theoretical dependence from Eq. (14) is 3.32.
- The ratio of the additional forces X_1'/X at the support D, during the change of distance $L = 1200$ mm to $L' = 800$ mm, for both values of parameter k is within the range between 1.23 and 1.31; the calculation result of the obtained theoretical dependence from Eq. (15) is 1.31.

The differences between the numerical and experimental results are less than 6 %. These differences relate to the approximation of moments of inertia and neglecting the influence of the coefficient ε.

4 CONCLUSION

The theoretical and experimental analysis of the influences of geometrical parameters on the value of additional forces at the supports of undercarriage frames indicates the following conclusions:

- The ratio between the bending moment of inertia and the torsional moment of inertia of the box-like section with unique plate thickness depends on the height/width ratio k as defined in Eq. (10).
- As a consequence of the aforementioned, the ratio of bending stiffness and torsional stiffness can be defined by Eq. (11).
- The relation between the force ratio $X_{1(j)}/X_{1(i)}$ and the change of height/width coefficient ratio k_j/k_i is defined by Eq. (14).
- The relation between the force ratio $X_{1(j)}/X_{1(i)}$ and the change of length ratio L_i/L_j is defined by Eq. (15).

The relative error of mentioned approximations does not exceed 6 % in comparison to test results.

The results of the research considerably simplify optimization methods in the design of carrying structures with box-like girders and make the precondition for further investigation of their influence on the functioning of large diameter bearing.

5 ACKNOWLEDGEMENTS

A part of this research is a contribution to the project TR 35038 funded by the Ministry of Education, Science and Technological Development of the Republic of Serbia.

6 REFERENCES

[1] Göncz, P., Potočnik, R., Glodež, S. (2013). Computational model for determination of static load capacity of three-row slewing bearings with arbitrary clearances and predefined raceway deformations. *International Journal of Mechanical Science*, vol. 73, p. 82-92, **DOI:10.1016/j.ijmecsci.2013.04.012**.

[2] Zupan, S., Prebil, I. (2001). Carrying angle and carrying capacity of a large single row ball bearing as a function of geometry parameters of rolling contact and supporting structure stiffness. *Mechanism and Machine Theory*, vol. 36, no. 10, p. 1087-1103, **DOI:10.1016/S0094-114X(01)00044-1**.

[3] Amasorrain, J.I., Sagartzazu, X., Damián, J. (2003). Load distribution in a four contact-point slewing bearing. *Mechanism and Machine Theory*, vol. 38, no. 6, p. 479-496, **DOI:10.1016/S0094-114X(03)00003-X**.

[4] Kania, L., Pytlarz, R., Śpiewak, S. (2018). Modification of the raceway profile of a single-row ball slewing bearing. *Mechanism and Machine Theory*, vol. 128, p. 1-15, **DOI:10.1016/j.mechmachtheory.2018.05.009**.

[5] Deng, B., Guo, Y., Zhang, A., Tang, S. (2017). Finite element analysis of thrust angle contact ball slewing bearing. *IOP Conference Series: Materials Science and Engineering*, vol. 274, art. id. 012096, p. 1-6, **DOI:10.1088/1757-899X/274/1/012096**.

[6] Olave, M., Sagartzazu, X., Damian, J., Serna, A. (2010). Design of four contact-point slewing bearing with a new

load distribution procedure to account for structural stiffness. *Journal of Mechanical Design*, vol. 132, no. 2, **DOI:10.1115/1.4000834**.

[7] Heras, I., Aguirrebeitia, J., Abasolo, M. (2017). Friction torque in four contact point slewing bearings: Effect of manufacturing errors and ring stiffness. *Mechanism and Machine Theory*, vol. 112, p. 145-154, **DOI:10.1016/j.mechmachtheory.2017.02.009**.

[8] He, P., Liu, R., Hong, R., Wang, H., Yang, G., Lu, C. (2018). Hardened raceway calculation analysis of a three-row roller slewing bearing. *International Journal of Mechanical Sciences*, vol. 137, p. 133-144, **DOI:10.1016/j.ijmecsci.2018.01.021**.

[9] Smolnicki, T., Stanco, M., Pietrusiak, D. (2013). Distribution of loads in the large size bearing-problems of identification. *Tehnički vjesnik - Technical Gazette*, vol. 20, no. 5, p. 831-836.

[10] Jerman, B., Hladnik, J., Resman, F., Landschützer, C. (2018). Optimization of the support structure of large axial-radial bearing of overhead type manipulator. *FME Transactions*, vol. 46, no. 3, pp. 386-391, **DOI:10.5937/fmet1803386J**.

[11] Chen, G., Wang, C., Xiao, Z. (2016). Effects of supporting Structure and bolt connection on the fatigue life and carrying capacity of a slewing bearing. *Proceedings of the Institution of Mechanical Engineers, Part J: Journal of Engineering Tribology*, vol. 231, no. 6, p. 1-17, **DOI:10.1177/1350650116677606**.

[12] Duval, R., Bannebach, J., Blasiak, J., Guelbi, A. (2018). Modelling fatigue behavior of slewing rings in crane structures. Identification of influencing parameters on local stresses and fatigue damage calculations. *Procedia Engineering*, vol. 213, p. 323-334, **DOI:10.1016/j.proeng.2018.02.033**.

[13] He, P., Hong, R., Wang, H., Lu, C. (2018). Fatigue life analysis of slewing bearings in wind turbines. *International Journal of Fatigue*, vol. 111, p. 233-242, **DOI:10.1016/j.ijfatigue.2018.02.024**.

[14] Pietrusiak, D., Smolnicki, T., Stańńco, M. (2017). The influence of superstructure vibrations on operational loads in the undercarriage of bulk material handling machine. *Archives of Civil and Mechanical Engineering*, vol. 17, no. 4, p. 855-862, **DOI:10.1016/j.acme.2017.03.001**.

[15] Maslak, P., Przybylek, G., Smolnicki, T. (2017). Comparison of selected methods for the determination of the center of gravity in surface mining machines. *Materials Today: Proceedings*, vol. 4, no. 5, p. 5877-5882, **DOI:10.1016/j.matpr.2017.06.062**.

[16] Gašić, M., Savković, M., Bulatović, R. (2011). Optimization of trapezoidal cross section of the truck crane boom by Lagrange's multipliers and by differential evolution algorithm (DE). *Strojniški vestnik - Journal of Mechanical Engineering*, vol. 57, no. 4, p. 304-312, **DOI:10.5545/sv-jme.2008.029**.

[17] Karnovsky, I.A., Lebed, O. (2010). Advanced Methods of Structural Analysis, Springer New York, London.

[18] EN 10025:2005. *Hot Rolled Products of Structural Steels - Part 1: General Technical Delivery Conditions*. European Committee for Standardization, Brussels., **DOI:10.3403/03152972**.

Strojniški vestnik - Journal of Mechanical Engineering 65(2019)6, 375-385
DOI:10.5545/sv-jme.2019.6057
Original Scientific Paper
Received for review: 2019-03-02
Received revised form: 2019-05-06
Accepted for publication: 2019-05-31

Cutting Forces and Surface Roughness in Face-Milling of SKD61 Hard Steel

Tien Dung Hoang – Nhu-Tung Nguyen* – Đuc Quy Tran – Van Thien Nguyen
Hanoi University of Industry, Vietnam

This experimental study investigated the effects of milling conditions on cutting forces and finished surface roughness. The face-milling processes were performed using heat-treated SKD61 steel at a hardness of 46 HRC. With three controllable factors/levels (cutting speed, axial depth of cut, and feed rate), the most suitable orthogonal array L_{27} was performed with four performance measurements that are amplitudes of cutting forces in three directions (feed, normal, and axial) and surface roughness. With ANOVA analysis, the effect of cutting conditions on the amplitudes of cutting forces and surface roughness were analysed and modelled. The most suitable regression of the cutting force's amplitudes and surface roughness was a quadratic regression with the confidence level is more than 93.74 %, and they were successfully verified via experimental results with very promising results. The relationship between cutting force and surface roughness was also investigated. Furthermore, using the Taguchi and ANOVA methods, the optimization process of surface roughness was performed with very close results (different of surface roughness about 4.58 %). The approach method of the present study can be applied in industrial machining to improve the surface quality in finish face-milling the SKD61 hard steel.

Keywords: surface roughness, cutting force, Taguchi method, ANOVA method, SKD61

Highlights

- *The effect of cutting conditions on cutting forces and surface roughness were investigated in the face-milling of SKD61 hard steel.*
- *The surface roughness and cutting forces were modelled with quadratic regression, and these models were successfully verified with the experimental results.*
- *The relationship between cutting force and surface roughness was also investigated.*
- *The optimization process of surface roughness was performed and can be applied in industrial machining to improve the surface quality.*

0 INTRODUCTION

Milling is one of the most critical processes in the manufacturing industry. In the milling process, a reliable quantitative prediction of cutting forces is critical to predicting the power and torque requirements (choice of electric motor), machine-tool vibrations, surface quality, geometrical accuracy, etc. However, given the power, surface quality, productivity, and stability are limited by milling process defects, such as deflection and chatter regeneration resulting from cutting forces.

The cutting forces were modelled depending on the tool geometry, cutting conditions, and the interaction of tool and workpiece (cutting force coefficients). This method has been used for the modelling of cutting forces in many machining processes, such as turning **[1]**, drilling **[2]**, and milling **[3]** and **[4]**.

In milling processes, with both cutting force modelling theories and experiments, the cutting forces had been modelled and verified for many tool types such as flat-end mill **[5]** to **[7]**, ball-end mill **[8]** and **[9]**, bull-end mill **[10]**, and general-end mill **[11]**. In these research studies, the cutting force values were predicted for each rotation angle of the tool. This method could show details of the cutting forces for each revolution of the tool, but the number of calculations was very large. However, this method could only be applied for short milling processes having several tool revolutions. Furthermore, many coefficients, such as cutting force coefficients and friction coefficients, must be obtained via experimental methods. Therefore, this method consumed a lot of time, effort and money. A simple experimental method is proposed in this paper to investigate the dynamic cutting forces and surface roughness by using the Taguchi method and ANOVA analysis to shorten the processing time.

The Taguchi method and ANOVA analysis have been widely used in industrial engineering analysis. Moreover, the Taguchi method employs a special design of orthogonal array by reducing the number of experiments to investigate the effect of the entire range of machining parameters. Recently, this method has been widely employed in several industrial fields and research work. ANOVA analysis was used to research the effect of main machining parameters

*Corr. Author's Address: Hanoi University of Industry, Number 298, Cau Dien Street, Bac Tu Liem Distric, Ha Noi City, Vietnam, tungnn@haui.edu.vn

such as machining polarity, peak current, pulse duration, among others, on the wire-cut electrical discharge machining (WEDM) characteristics such as material removal rate, surface roughness [12] and [13]. Tsoukalas [14] and Hsu and Do [15] used an L_{27} orthogonal array of Taguchi method to determine the optimum conditions leading to minimum porosity in aluminium alloy die castings. Rao and Padmanabhan [16] applied the Taguchi method and ANOVA in the optimization of process parameters for metal removal rate in electrochemical machining of Al/5%SiC composites. Furthermore, the Taguchi method and ANOVA analysis were also applied to investigate other machining processes, such as abrasive waterjet cutting [17], turning [18] and [19], drilling [20] to [22], and milling [23] to [25].

The surface roughness and cutting force are important machining characteristics for evaluating the productivity of machining processes. In milling processes, by using Taguchi method and ANOVA analysis, the cutting forces and surface roughness could be investigated based on a number of factors, such as depth of cut, feed rate, cutting speed, cutting time, workpiece hardness, etc. Several research works had been conducted in different conditions and had also been applied for different workpieces and tool materials, such as Kıvak [26], Ozcelik and Bayramoglu [27], Turgut et al. [24], Karakas et al. [28], and Jayakumar et al. [29].

However, although there have already been many studies on cutting forces and surface roughness, it seems that the essential values such as the amplitude of cutting forces in milling processes have not been mentioned. These values can be used to predict the power consumption, energy, and the strength of the tool material needed. Besides, the relationship between cutting forces and surface roughness seems not to have been studied in previous research studies.

In this study, the influence of cutting conditions on the surface roughness and the amplitude of cutting force was investigated when face milling the SKD61 hard steel. The main contributions of this study are in three aspects: (1) Evaluate the effect of cutting conditions on surface roughness and cutting force amplitude, (2) Evaluate the tendency of surface roughness and cutting force amplitudes when cutting conditions change, and (3) determine the optimal cutting conditions by different methods.

1 EXPERIMENTAL METHOD

1.1 The Experiment Setup

1.1.1 Workpiece and Tool

During hard milling processes, in order to investigate the influence of machining conditions on the cutting force and surface roughness, a series of face finished milling experiments were performed. The cutter and workpiece were chosen as follows. Cutter: A Sandvik Coromant R390-020A20-11L CoroMill 390 Square Shoulder Milling Cutter, with number of inserts N = 2, a tool cutting edge angle of 90°, a ramping angle maximum of 5.5°, and a diameter of 20 mm. Insert: Sandvik Coromant R390-11 T3 08m-pl 4220 Milling Insert, cutting edge effective length of 10 mm, corner radius of 0.8 mm, Coating (CVD Ti (C, N) + Al_2O_3+TiN).

The workpiece (dimensions of 70 mm × 50 mm × 15 mm) material was SKD61, and its compositions are listed in Table 1. The properties of the SKD61 were: Hardness 46 HRC, Young's modulus = 210 GPa, Density = 7.8 g/cm^3.

Table 1. *Chemical composites of SKD 61*

Element	C	Si	Mn	Cr	Mo	V
Composite [%]	0.32 to 0.42	0.18 to 1.2	≤0.5	4.5 to 5.5	1.0 to 1.5	0.8 to 1.2

1.1.2 Machine Set-Up and Cutting Force Measurements

The experiments were performed at a five-axis vertical machining centre (DMU 50 - 5 Axis Milling). All experiments were performed under dry machining conditions. A dynamometer (Kistler Type 9139AA**:** Force Ranges: (–3 kN to 3 kN), data processing box, and a PC were used to measure cutting forces. The detail is illustrated in Fig 1.

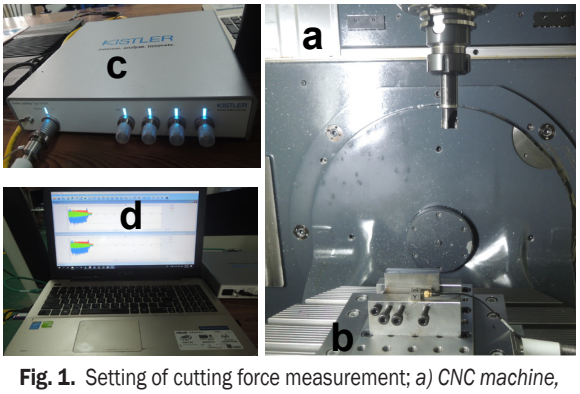

Fig. 1. Setting of cutting force measurement; *a) CNC machine, b) dynamometer, c) processing box, and d) PC and display system*

The amplitudes of cutting forces were measured in three directions (feed, normal, and axial), as shown in Fig. 2. Each measurement was repeated three times following the cutting test repeated three times. The values of the measurements were stored and analysed.

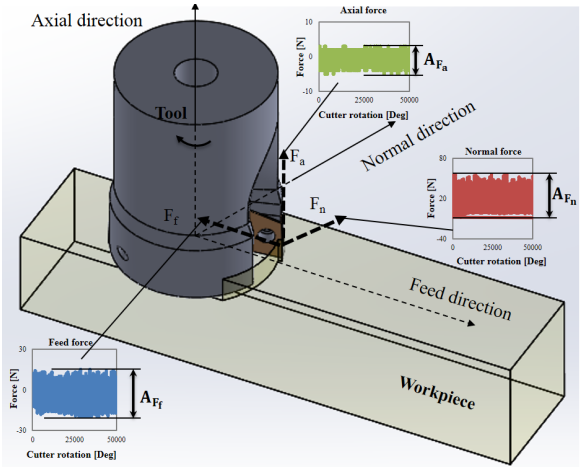

Fig. 2. *Amplitudes of cutting forces in three directions*

1.1.3 Surface Roughness Measurements

The surface roughness (R_a) of the product was measured with a MITUTOYO-Surftest SJ-210 Portable Surface Roughness Tester **(**Japan**)**. The cut-off length and evaluation length were fixed at 0.8 mm and 4 mm, respectively. The surface roughness was measured parallel to the machined surface from three different points and repeated three times following three repeated times of each cutting test. The average values of the measurements were evaluated.

1.2 Taguchi Method and Experiment Design

The Taguchi method was developed by Genuchi Taguchi; it is a statistical method used to improve the product quality and is commonly used in improving industrial product quality due to its proven success. It is an experimental design and also a beneficial technique for high quality system design. In engineering analysis, the Taguchi method is a powerful method that has been widely used around the world. This method dramatically reduces the number of experiments by using orthogonal arrays and minimizes the effects of factors that cannot be controlled **[30]**.

In this research, the cutting speed (V_c), axial depth of cut (a), feed rate (f_t) were selected as control factors, and their levels were expressed in Table 2. In the experimental layout plan, with three factors and three levels, the most suitable orthogonal array (L_{27}) was chosen to analyse the influence of machining parameters on the surface roughness and cutting force **[31]**. The experimental plan was performed with 27 experiments and detailed as in Table 3. Furthermore, the response surface methodology (RSM) technique has been used for the design of experiments and analysis of experimental results **[32]**. RSM is used to model and analyse the response variables that are influenced by several controllable input variables. Then, RSM is generated as an interaction between statistical and mathematical techniques **[33]**.

Table 2. *Milling parameters and their levels*

No.	Machining parameters	Level 1	Level 2	Level 3
1	Cutting speed, V_c [m/min]	80	140	200
2	Axial depth of cut, a [mm]	0.1	0.3	0.5
3	Feed rate, f_t [mm/flute]	0.05	0.10	0.15

Table 3. *The experimental design and results with an orthogonal array of Taguchi L_{27}*

N	Input factors			Performance measures			
	V_c	a	f_t	R_a [μm]	A_{F_f} [N]	A_{F_n} [N]	A_{F_a} [N]
1	80	0.1	0.05	0.166	70.8	36.3	78.3
2	80	0.1	0.10	0.338	97.1	53.6	126.8
3	80	0.1	0.15	0.418	114.9	71.5	214.4
4	80	0.3	0.05	0.215	166.6	91.6	184.4
5	80	0.3	0.10	0.309	212.6	126.4	276.1
6	80	0.3	0.15	0.422	267.6	158.3	317.1
7	80	0.5	0.05	0.185	248.5	134.1	197.7
8	80	0.5	0.10	0.311	364.7	193.8	225.1
9	80	0.5	0.15	0.473	436.1	241.7	266.9
10	140	0.1	0.05	0.174	74.6	37.2	157.1
11	140	0.1	0.10	0.359	105.6	59.2	232.9
12	140	0.1	0.15	0.419	125.8	73.3	314.5
13	140	0.3	0.05	0.168	187.4	87.0	198.7
14	140	0.3	0.10	0.287	240.4	123.9	306.0
15	140	0.3	0.15	0.392	329.0	168.3	400.6
16	140	0.5	0.05	0.183	280.9	135.2	266.8
17	140	0.5	0.10	0.372	376.0	195.2	357.5
18	140	0.5	0.15	0.435	434.2	235.7	446.4
19	200	0.1	0.05	0.192	124.5	58.1	192.9
20	200	0.1	0.10	0.354	153.8	74.2	275.8
21	200	0.1	0.15	0.413	176.8	84.4	341.2
22	200	0.3	0.05	0.200	202.2	94.1	253.1
23	200	0.3	0.10	0.329	291.2	133.2	386.4
24	200	0.3	0.15	0.444	355.7	175.6	447.6
25	200	0.5	0.05	0.305	281.4	122.7	349.5
26	200	0.5	0.10	0.444	466.3	175.4	431.2
27	200	0.5	0.15	0.492	528.9	253.9	574.4

2 RESULTS

2.1 Analysis for Surface Roughness

2.1.1 Analysis of Variance (ANOVA) for Surface Roughness

The experimental results were investigated and listed in Table 3. In this study, ANOVA was used to analyse the influence of cutting speed, axial depth of cut, and feed rate on the surface roughness and amplitudes of cutting forces. This analysis was performed with a 95 % confidence level and a 5 % significance level. This indicates that the obtained models are considered to be statistically significant. The coefficient of determination (R^2) is defined as the ratio of the explained variation to the total variation and is a measure of the fit degree. When R^2 approaches unity, it indicates a good correlation between the experimental and the predicted values.

Table 4. *Results of ANOVA for surface roughness*

Number of obs: 27						R-squared: 0.9881
Root MSE: 0.0209						Adj R-squared: 0.9613
Source	SS	DOF	MS	F-value	Prob > F	Contribution [%]
Model	0.2904	18	0.0161	36.91	0.0000	
V_c	0.0097	2	0.0049	11.13	0.0049	3.30
a	0.0121	2	0.0061	13.88	0.0025	4.12
f_t	0.2545	2	0.1273	291.1	0.0000	86.59
$V_c \times a$	0.0087	4	0.0022	4.99	0.0258	2.96
$V_c \times f_t$	0.0024	4	0.0006	1.35	0.3306	0.82
$a \times f_t$	0.0030	4	0.0008	1.69	0.2445	1.02
Error	0.0035	8	0.0004			1.19
Total	0.2939	26	0.0113			100

In Table 4, the contributions of each factor on surface roughness were listed in the last column. It is clear from the results of ANOVA that the most important factor affecting the surface roughness was feed rate (86.59 %). The other factors differently affect surface roughness. The second factor influencing surface roughness was the axial depth of cut (4.12 %). The third factor influencing on the surface roughness was cutting speed (3.3 %).

2.1.2 Regression and Verification of Surface Roughness Model

The regression analysis was used to model and analyse the relationship between a dependent variable and one or more independent variables. In this study, three dependent variables are surface roughness and amplitudes of cutting force in three directions (axial, feed, normal), whereas the independent variables are cutting speed (V_c), axial depth of cut (a), and feed rate (f_t). By using Intercooled Stata 8.2™ software, the most suitable regression of surface roughness was a quadratic regression, as given in Eq. (1).

$$\begin{cases} R_a = 0.1143 - 0.0018 \times V_c - 0.5515 \times a + 4.9692 \times f \\ \quad +0.0016 \times V_c \times a - 0.0026 \times V_c \times f_t \\ \quad +0.0750 \times a \times f + 0.00007 \times V_c^2 \\ \quad +0.6958 \times a^2 - 11.3333 \times f_t^2, \\ R^2 = 95.85\%, R_{Adj}^2 = 93.66\%, \\ \quad R_{Adj}^2 \text{ is the Adjusted } R^2 \end{cases} \quad (1)$$

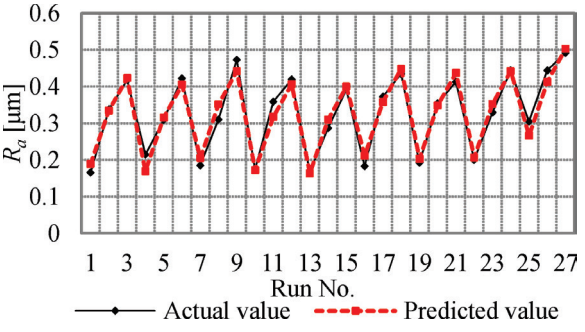

Fig. 3. *Measured and predicted results of surface roughness*

The verification results of the surface roughness model were described in Fig. 3. As seen from this figure, the predicted results were very close to the experimental results. There is a very good relation between predicted values and test values. The R^2 values of the equations obtained by the quadratic regression model for surface roughness were found to be 95.85 %. These results showed that the quadratic regression model was shown to be successfully investigated regarding surface roughness in the face-milling processes of SKD61 hard steel.

2.1.3 Parametric Influence on Surface Roughness

The variation of surface roughness corresponding to the axial depth of cut, feed rate, and cutting speed was described in Fig 4. The consequences of the axial depth of cut and federate on surface roughness for three cutting speed as 80 m/min, 140 m/min, and 200 m/min, respectively. It is very clear that surface roughness increases with increasing feed rate. This trend can be explained that when feed rate increases, that results in an increase in undeformed chip thickness, and undeformed chip thickness is directly proportional to cutting forces. Then, when

the cutting forces increase, the stability and damping characteristics of the machine-tool system will be affected, which makes more vibrations and ultimately affects the surface roughness. This result is similar to the result of the change in the surface roughness that is noted in several works such as [34] and [35].

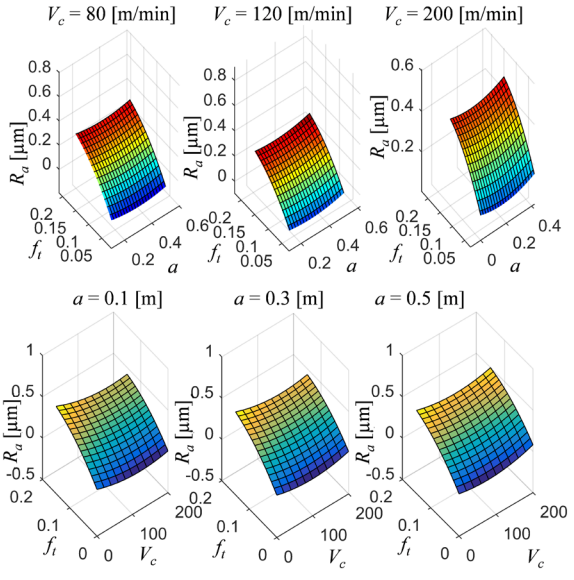

Fig. 4. *Effect of cutting conditions on surface roughness*

The surface roughness values exhibited decreasing tendency with increasing of axial depth of cut from 0 mm to about 0.3 mm, but when the axial depth of cut increases from about 0.3 mm to 0.5 mm, the tendency of surface roughness was reversed. Similarly, the surface roughness decreases with increasing of cutting speed from 0 m/min to about 130 m/min, and with the cutting speed increases from about 130 m/min to 200 m/min, the tendency of surface roughness is also increasing. So, to improve the surface roughness in the face-milling process of SKD61 hard steel, with regard to machining conditions, it was proposed that as the feed rate decreases, the axial depth of cut is about 0.3 mm, and the cutting speed is about 130 m/min.

2.2 Analysis for the Feed Force's Amplitude

2.2.1 Analysis of Variance for the Feed Force's Amplitude

The ANOVA results for the amplitude of the feed force was illustrated in Table 5; the contributions of each factor on the amplitude of feed force were listed in the last column. It seems that the most important factor affecting the amplitude of feed force was the axial depth of cut (72.89 %). The second factor influencing the amplitude of feed force was feed rate (16.78 %). The third factor influencing the surface roughness was cutting speed (4.96 %).

Table 5. *Results of ANOVA for feed force's amplitude*

Number of obs: 27					R-squared: 0.9953	
Root MSE: 15.9447					Adj R-squared: 0.9846	
Source	SS	DOF	MS	F-value	Prob > F	Contr. [%]
Model	427244.87	18	23735.83	93.36	0.0000	
V_c	21301.93	2	10650.97	41.89	0.0001	4.96
a	312903.54	2	156451.77	615.29	0.0000	72.89
f_t	72015.59	2	36007.80	141.63	0.0000	16.78
$V_c \times a$	1122.92	4	280.73	1.10	0.4175	0.26
$V_c \times f_t$	2063.01	4	515.75	2.03	0.1831	0.48
$a \times f_t$	17837.86	4	4459.47	17.54	0.0005	4.16
Error	2033.86	8	254.23			0.47
Total	429278.72	26	16510.72			100

2.2.2 Regression and Verification of the Feed Force's Amplitude Model

The most suitable regression of amplitude of feed force was a quadratic regression as given in Eq. (2). The compared results of measured values and predicted values of feed force's amplitudes were described in Fig. 5. It seems that the predicted results were very close to the measured results. The R^2 values of the equations obtained with the quadratic regression model for feed force's amplitude were found to be 98.74 %. So, the quadratic regression model is the most suitable regression of amplitude of the feed force.

$$\begin{cases} A_{F_f} = 44.3740 - 0.9807 \times V_c + 275.4722 \times a \\ \quad +617.9998 \times f_t + 0.3819 \times V_c \times a \\ \quad +3.3500 \times V_c \times f_t + 3673.333 \times a \times f_t \\ \quad +0.0039 \times V_c^2 - 61.8055 \times a^2 - 4655.555 \times f_t^2 \\ R^2 = 98.74\,\%, \quad R_{Adj}^2 = 98.08\% \end{cases} \quad (2)$$

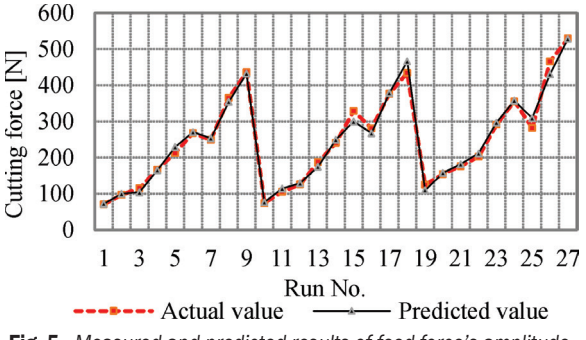

Fig. 5. *Measured and predicted results of feed force's amplitude*

2.2.3 Parametric Influence on Amplitude of Feed Force

The variation of feed force's amplitude corresponding to the axial depth of cut and feed rate is described in Fig 6. This figure shows clearly that the feed force's amplitude increases with the increasing axial depth of cut and feed rate. This can be explained by the fact that when the axial depth of cut and feed rate increase, which increases the volume of chip thickness, and volume of chip thickness is directly proportional to cutting forces. Thus, the cutting forces' amplitude increases.

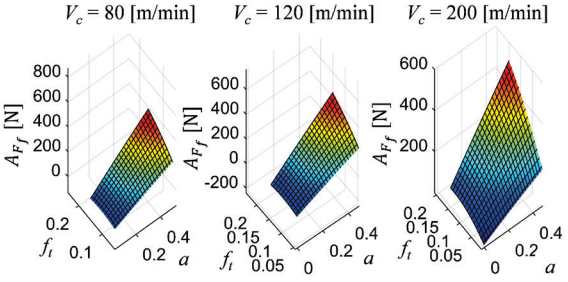

Fig. 6. *Effect of cutting conditions on feed force's amplitude*

2.3 Analysis for Normal Force's Amplitude

2.3.1 Analysis of Variance for Normal Force's Amplitude

The values of Table 6 show that the quadratic model is the most suitable of normal force amplitude and the contributions of each factor on the amplitude of feed force are listed in the last column.

Table 6. *Results of ANOVA for Normal force's amplitude*

Number of obs: 27					R-squared: 0.9958	
Root MSE: 7.3608					Adj R-squared: 0.9864	
Source	SS	DOF	MS	F-value	Prob > F	Contr. [%]
Model	102808.49	18	5711.58	105.42	0.0000	
V_c	273.98	2	136.99	2.53	0.1409	0.27
a	72309.73	2	36154.87	667.29	0.0000	70.04
f_t	24673.77	2	12336.88	227.69	0.0000	23.90
$V_c \times a$	518.74	4	129.69	2.39	0.1365	0.50
$V_c \times f_t$	137.79	4	34.45	0.64	0.6514	0.13
$a \times f_t$	4894.47	4	1223.62	22.58	0.0002	4.74
Error	433.45	8	54.18			0.42
Total	103241.94	26	3970.84			100

Clearly, the most important factor affecting on the amplitude of the normal force was the axial depth of cut (70.04 %). The second factor influencing the amplitude of normal force was the feed rate (23.90 %). The cutting speed has little effect on the amplitude of normal force (0.27 %).

2.3.2 Regression and Verification of Normal Force's Amplitude

The regression of amplitude of the normal force was a quadratic regression, as given in Eq. (3). The compared results of the measured values and predicted values of normal force's amplitudes are described in Fig. 7, which shows that the predicted results were very close to the measured results. The R^2 values of the equations obtained by quadratic regression model for feed force's amplitude were found to be 99.42 %. So, the quadratic regression model is the most suitable regression of amplitude of normal force.

$$\begin{cases} A_{F_n} = 2.7917 - 0.0818 \times V_c + 253.8473 \times a \\ \quad +69.4723 \times f_t - 0.5063 \times V_c \times a \\ \quad +0.8194 \times V_c \times f_t + 2014.1660 \times a \times f_t \\ \quad +0.00075 \times V_c^2 - 112.9167 \times a^2 - 240.0002 \times f_t^2, \\ R^2 = 99.42\,\%, \quad R^2_{Adj} = 99.11\,\% \end{cases} \tag{3}$$

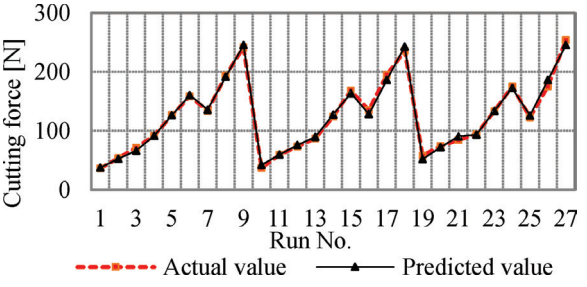

Fig. 7. *Measured and predicted results of normal force's amplitude*

2.3.3 Parametric Influence on Amplitude of Normal Force

The tendency of normal force's amplitude is the same as that of the feed force. The variation of the normal force's amplitude corresponding to the axial depth of cut and feed rate is described in Fig. 8, which shows that the normal force's amplitude increases with increasing of the axial depth of cut and feed rate. This is a result of the fact that when the axial depth of cut and feed rate increase, that results increase in the volume of chip thickness, and if the volume of chip thickness increases, the cutting forces' amplitude will also increase.

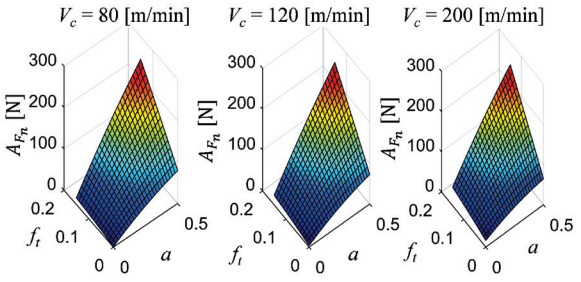

Fig. 8. *Effect of cutting conditions on normal force's amplitude*

2.4 Analysis for Axial Force's Amplitude

2.4.1 Analysis of Variance for Axial Force's Amplitude

The ANOVA results for the amplitude of axial force are described in Table 7. The contributions of each factor on the amplitude of axial force were calculated and listed in the last column. It seems that the influence of each factor on the amplitude of axial force was quite similar (feed rate: 33.74 %, cutting speed: 30.42 %, and axial depth of cut: 23.93 %).

Table 7. *Results of ANOVA for Axial force's amplitude*

Number of obs: 27					R-squared: 0.9698	
Root MSE: 38.5002					Adj R-squared: 0.902	
Source	SS	DOF	MS	F-value	Prob > F	Contr. [%]
Model	381253.26	18	21180.74	14.29	0.0003	
V_c	119568.02	2	59784.01	40.33	0.0001	30.42
a	94068.87	2	47034.43	31.73	0.0002	23.93
f_t	132632.98	2	66316.49	44.74	0.0000	33.74
$V_c \times a$	21406.58	4	5351.65	3.61	0.0577	5.45
$V_c \times f_t$	9411.24	4	2352.81	1.59	0.2676	2.39
$a \times f_t$	4165.57	4	1041.39	0.7	0.6118	1.06
Error	11858.14	8	1482.27			3.02
Total	393111.40	26	15119.67			100

2.4.2 Regression and Verification of Axial Force's Amplitude

The most suitable regression of axial force' amplitude was a quadratic regression as given in Eq. (4). The R^2 values of the equations obtained by quadratic regression model for axial force's amplitude were found to be 93.74 %. The compared results of measured values and predicted values of feed force's amplitudes are described in Fig. 9, which shows that the tendencies and the values of predicted results were very close to the tendencies and the values of measured results. So, the quadratic regression model is the most suitable regression of amplitude of axial force.

$$\begin{cases} A_{F_a} = 40.9349 + 0.1876 \times V_c + 206.9375 \times a \\ \quad -188.6806 \times f_t + 2.6045 \times V_c \times a \\ \quad +9.1569 \times V_c \times f_t + 1099.5830 \times a \times f_t \\ \quad -0.0019 \times V_c^2 - 542.5695 \times a^2 + 1465.5550 \times f_t^2, \\ R^2 = 93.74\,\%, \quad R_{Adj}^2 = 90.42\,\% \end{cases} \tag{4}$$

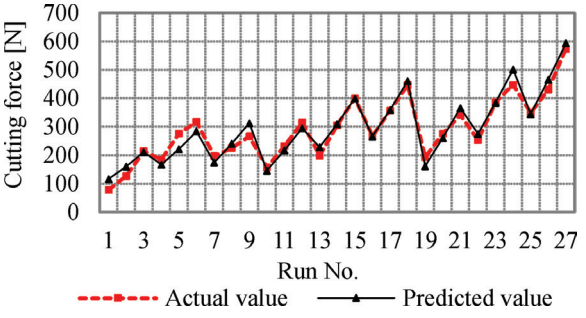

Fig. 9. *Measured and predicted results of axial force's amplitude*

2.4.3 Parametric Influence on Amplitude of Axial Force

The tendency of axial force's amplitude is also the same as that of the feed force. Fig. 10 presents the variation of axial force's amplitude corresponding to axial depth of cut and feed rate. Figure 10 revealed that the axial force's amplitude increases with increase in axial depth of cut and feed rate. The reason for this tendency is the same as for the feed force's amplitude and normal force's amplitude as well.

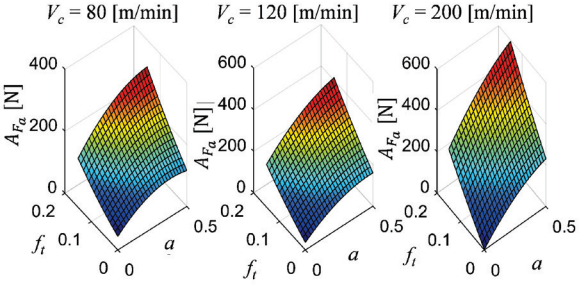

Fig. 10. *Effect of cutting conditions on axial force's amplitude*

2.5 The Relationship of Cutting Force and Surface Roughness in Milling

In this paper, the relationship between cutting force's amplitude and surface roughness was also investigated. It seems that this relationship has not been studied previously. The amplitudes of cutting forces and the surface roughness were drawn in

one diagram, as shown in Fig. 11. It seems that the tendency of the surface roughness is the same as that of the cutting force's amplitudes. As seen from this figure, if the cutting force's amplitudes increase, the surface roughness increases; if the cutting force's amplitudes decrease, the surface roughness also decreases. These could be explained that in finish-face milling processes, at the high stable cutting conditions with small vibrations, the chip thickness is quite stable, it makes the machining surface quite smooth, and so the surface roughness is often small (good surface). Furthermore, in this process, because the chip thickness is quite stable, the cutting forces in all directions are often quite stable, and these make the amplitudes of cutting forces smaller than those at other machining conditions. In the opposite cases, when the milling conditions are unstable cutting with chatter or large vibrations, the chip thickness will be unstable; it makes the surface and cutting force more unstable as well, and so that the amplitudes of cutting forces and surface roughness will be larger than that of other milling conditions. Thus, in this study, it is seen that there is the same tendency of output parameters in machining processes. By this reason, in this study, the optimal value was determined for surface roughness that is one of the most important values to improve the quality of machining product, as presented in Section 2.6.

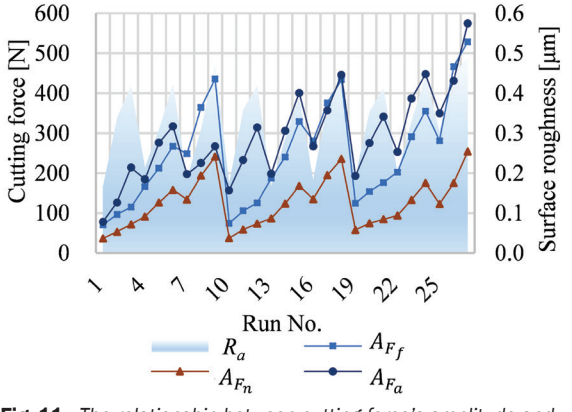

Fig. 11. *The relationship between cutting force's amplitude and surface roughness*

2.6 Optimization of Cutting Conditions

2.6.1 Estimation of Optimum Surface Roughness by ANOVA Method

The lowest value of surface roughness is very important for quality improvement of the machining product and lowering production costs. In this study, the quadratic regression model of surface roughness as presented by Eq. (1) that was used to find the optimized values of surface roughness and machining parameters. By using MATLAB R2013a™ software, the optimized results of machining parameters were obtained as f_{val}=0.1531, x=[113.0595, 0.2636, 0.0500], where f_{val} is the optimal value of the surface roughness as presented by Eq. (1). And, x are the values of variables in Eq. (1) when surface roughness equals to f_{val}.

Thus, with the ANOVA method, the optimal parameters of milling process were determined as cutting speed: V_c = 113.0595 m/min, axial depth of cut: a = 0.2636 mm, feed rate: f_t = 0.0500 mm/flute.

And, the optimization value of surface roughness was R_a = 0.1531 μm.

2.6.2 Analysis of the Signal-to-Noise (S/N) Ratio

Using the Taguchi method, the optimal values of control factor were determined by analysis of the signal-to-noise ratio. The lowest value of surface roughness is very important to improve the machining product, so the smaller-the-better equation was used for calculation of the *S/N* ratio [31]. The values of the *S/N* response for observations of surface roughness were listed in Table 8 and shown in Fig. 12.

Table 8. *The S/N response for surface roughness*

Factor	Mean S/N ratio			Delta
	Level 1	Level 2	Level 3	
V_c	9.8245	10.0299	9.5829	0.4469
a	10.0552	10.2519	9.1301	1.1218
f_t	13.4388	8.5886	7.4099	6.0289

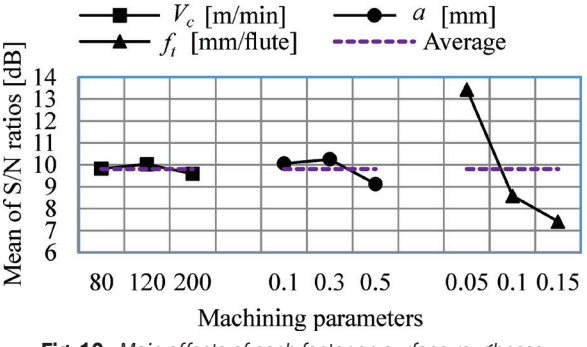

Fig. 12. *Main effects of each factor on surface roughness*

With Taguchi techniques, the best level of each control factor was determined according to the highest *S/N* ratio at the level of that control factor [32]. With these techniques, from the values of Table 7 and Fig. 12, the level and *S/N* ratios for the factors giving the

best R_a value were specified as factor cutting speed (level 2, S/N = 10.029881 dB), factor axial depth of cut (level 2, S/N = 10.251945 dB), factor feed rate (level 1, S/N = 13.438819 dB). So, with the Taguchi method, the optimum value of surface roughness was obtained at a cutting speed of 140 m/min, a depth of cut of 0.3 mm, and a feed rate of 0.05 mm/flute. The value of surface roughness with optimized values is 0.1605 **µm.** The comparison results of the optimization values of the two methods were described in Table 9. The optimized results between the ANOVA method and Taguchi method are quite close together. However, the ANOVA method gave the better result regarding surface roughness. So, this method can be applied to improve the surface quality in finished face milling the SKD61 hard steel.

Table 9. *The optimized results of ANOVA and Taguchi method*

Machining parameters	Optimization values		Differences [%]
	ANOVA method	Taguchi method	
V_c	113.0595	140	19.24
a	0.2636	0.3	12.13
f_t	0.05	0.05	0.00
R_a [µm]	0.1605	0.1531	4.58

3 CONCLUSIONS

In this study, an experimental method was performed to investigate the influence of cutting conditions on the surface roughness and cutting force's amplitudes. Depending on the analysis of experimental results, the conclusions of this study can be drawn as follows.

1. The most important factor affecting the surface roughness was the feed rate (86.594 %), while the most important factor affecting on the cutting force's amplitudes was the axial depth of cut (72.891 % for feed force amplitude and 70.039 % for normal force amplitude). The other factors affect differently on the surface roughness and cutting force's amplitudes.
2. The cutting force's amplitudes increase with the increasing of the axial depth of cut and feed rate. While the surface roughness decreases with the decreasing of the feed rate, with increasing of axial depth of cut from 0 mm to about 0.3 mm, and with the increasing of cutting speed from 0 m/min to about 130 m/min. Furthermore, the surface roughness increases with increasing of feed rate, with increasing of axial depth of cut from about 0.3 mm to 0.5 mm, and with increasing of cutting speed from about 130 m/min to 200 m/min. To improve the surface roughness in the face-milling process of SKD61hard steel, with regards to machining conditions, it was proposed that the feed rate decreases, the axial depth of cut is about 0.3 mm, and the cutting speed is about 130 m/min.
3. The tendency of the surface roughness is the same as that of the cutting force's amplitudes. So, the optimal value was determined for surface roughness, which is one of the most important values to improve the quality of machining product.
4. The Taguchi and ANOVA methods can be used to find the optimal value of surface roughness. In this study, the optimized result from ANOVA method is better than that of the Taguchi method. The optimum value of surface roughness is 0.1531 µm, which was obtained at cutting speed of 113.0595 m/min, at an axial depth of cut of 0.2636 mm, and a feed rate of 0.05 mm/flute.

The cutting force amplitude and surface roughness models can be applied in the adaptive control processes of CNC milling to improve the machining surface and reduce the cutting force and will be the futuristic study of future research.

4 ACKNOWLEDGEMENTS

The authors appreciate the generous assistance from the CNC Lab for the dynamometer in the cutting force measurement experiments. Thanks also extend to the support from the Faculty of Mechanical Engineering, Hanoi University of Industry (HaUI), Vietnam.

5 REFERENCES

[1] Fernández-Abia, A.I., Barreiro, J., López de Lacalle, L.N., Martínez-Pellitero, S. (2012). Behavior of austenitic stainless steels at high speed turning using specific force coefficients. *International Journal Advance Manufacturing Technology*, vol. 62, no. 5-8, p. 505-515, **DOI:10.1007/s00170-011-3846-9**.

[2] Guibert, N., Paris, H., Rech, J. (2008). A numerical simulator to predict the dynamical behavior of the self-vibratory drilling head. *International Journal of Machine Tools and Manufacture*, vol. 48, no. 6, p. 644-655, **DOI:10.1016/j.ijmachtools.2007.11.003**.

[3] Dang, J.-W., Zhang, W.-H., Yang, Y., Wan, M. (2010). Cutting force modeling for flat end milling including bottom edge cutting effect. *International Journal of Machine Tools and Manufacture*, vol. 50, no. 11, p. 986-997, **DOI:10.1016/j.ijmachtools.2010.07.004**.

[4] Rouzrokh, A., Yi-HsuanWei, C., Erkorkmaz, K., Pilliar, R.M. (2010). Machining Porous Calcium Polyphosphate Implants for Tissue Engineering Applications. *International*

Journal of Automation Technology, vol 4, no. 3, p. 291-302, **DOI:10.20965/ijat.2010.p0291**.

[5] Altintas, Y. (2012). *Manufacturing Automation: Metal cutting Mechanics, Machine Tool Vibrations, and CNC Design, 2nd ed.* Cambridge University Press, Cambridge, **DOI:10.1017/CBO9780511843723**.

[6] Wang, M., Gao, L., Zheng, Y. (2014). An examination of the fundamental mechanics of cutting force coefficients. *International Journal of Machine Tools and Manufacture*, vol. 78, p. 1-7, **DOI:10.1016/j.ijmachtools.2013.10.008**.

[7] Kao, Y.-C., Nguyen, N.-T., Chen, M.-S., Su, S.-T. (2015). A prediction method of cutting force coefficients with helix angle of flat-end cutter and its application in a virtual three-axis milling simulation system. *The International Journal of Advanced Manufacturing Technology*, vol. 77no. 9-12, p. 1793-1809, **DOI:10.1007/s00170-014-6550-8**.

[8] Narita, H. (2013) A Determination Method of Cutting Coefficients in Ball End Milling Forces Model. *International Journal of Automation Technology*, vol. 7, no. 1, p. 39-44, **DOI:10.20965/ijat.2013.p0039**.

[9] Tukora, B., Szalay, T. (2011). Real-time determination of cutting force coefficients without cutting geometry restriction. *International Journal of Machine Tools and Manufacture*, vol. 51, no. 12, p. 871-879, **DOI:10.1016/j.ijmachtools.2011.08.003**.

[10] Gao, G., Wu, B., Zhang, D., Luo, M. (2013). Mechanistic identification of cutting force coefficients in bull-nose milling process. *Chinese Journal of Aeronautics*, vol. 26, no. 3, p. 823-830, **DOI:10.1016/j.cja.2013.04.007**.

[11] Gradišek, J., Kalveram, M., Weinert, K. (2004). Mechanistic identification of specific force coefficients for a general end mill. *International Journal of Machine Tools & Manufacture*, vol. 44, no. 4, p. 401-414, **DOI:10.1016/j.ijmachtools.2003.10.001**.

[12] Suresh, P., Venkatesan, R., Sekar, T., Elango, N., Sathiyamoorthy, V. (2014). Optimization of intervening variables in microEDM of SS 316L using a genetic algorithm and response-surface methodology. *Strojniski vestnik - Journal of Mechanical Engineering*, vol. 60, no. 10, p. 656-664, **DOI:10.5545/sv-jme.2014.1665**.

[13] Ponnuvel, S., Senthilkumar, N. (2019). A study on machinability evaluation of Al-Gr-B 4 C MMC using response surface methodology-based desirability analysis and artificial neural network technique. *International Journal of Rapid Manufacturing*, vol. 8, no. 1-2, p. 95-122, **DOI:10.1504/ijrapidm.2019.10017666**.

[14] Tsoukalas, V.D. (2008). Optimization of porosity formation in AlSi9Cu3 pressure die casting using genetic algorithm analysis. *Material & Design*, vol. 29, no. 10, p. 2027-2033, **DOI:10.1016/j.matdes.2008.04.016**.

[15] Hsu, Q.C., Do, A.T. (2013). Minimum porosity formation in pressure die casting by Taguchi method. *Mathematical Problems in Engineering*, art. ID: 920865, p. 1-9, **DOI:10.1155/2013/920865**.

[16] Rao, S.R., Padmanabhan, G. (2012). Application of Taguchi methods and ANOVA in optimization of process parameters for metal removal rate in electrochemical machining of Al/5%SiC composites. *International Journal of Engineering Research and Applications*, vol. 2, no. 3, p. 192-197.

[17] Perec, A., Pude, F., Kaufeld, M., Wegener, K. (2017). Obtaining the selected surface roughness by means of mathematical model based parameter optimization in abrasive waterjet cutting. *Strojniski vestnik - Journal of Mechanical Engineering*, vol. 63, no. 10, p. 606-614, **DOI:10.5545/sv-jme.2017.4463**.

[18] Motorcu, A.R. (2010). The optimization of machining parameters using the Taguchi method for surface roughness of AISI 8660 hardened alloy steel. *Strojniski vestnik - Journal of Mechanical Engineering*, vol. 56, no. 6, p. 391-401

[19] Kumar, P., Chauhan , S.R., Pruncu, C.I., Gupta, M.K., Pimenov, D.Y., Mia, M., Gill, H.S. (2019). Influence of different grades of CBN inserts on cutting force and surface roughness of AISI H13 die tool steel during hard turning operation. *Materials*, vol. 12, no. 1, p. 177, **DOI:10.3390/ma12010177**.

[20] Siddiqueea, A.N., Khan, Z.A., Goel, P., Kumar, M., Agarwal, G., Khan, N.Z. (2014). Optimization of deep drilling process parameters of AISI 321 steel using Taguchi method. *Procedia Materials Science*, vol. 6, p. 1217-1225, **DOI:10.1016/j.mspro.2014.07.195**.

[21] Prasanna, J., Karunamoorthy, L., Raman, V.M., Prashanth, S., Chordia, D.R. (2014). Optimization of process parameters of small hole dry drilling in Ti–6Al–4V using Taguchi and grey relational analysis. *Measurement*, vol. 48, p. 346–354, **DOI:10.1016/j.measurement.2013.11.020**.

[22] Çiçek, A., Kıvak, T., Samtaş, G. (2012). Application of Taguchi method for surface roughness and roundness error in drilling of AISI 316 stainless steel. *Strojniški vestnik - Journal of Mechanical Engineering*, vol. 58, no. 3, p. 165-174, **DOI:10.5545/sv-jme.2011.167**.

[23] Ghani, J.A., Choudhury, I.A., Hassan, H.H. (2004). Application of Taguchi method in the optimization of end milling parameters. *Journal of Materials Processing Technology*, vol. 145, no. 1, p. 84-92, **DOI:10.1016/S0924-0136(03)00865-3**.

[24] Turgut, Y., Çinici, H., Sahin, I., Findik, T. (2011). Study of cutting force and surface roughness in milling of Al/Sic metal matrix composites. *Scientific Research and Essays*, vol. 6, no. 10, p. 2056-2062, **DOI:10.5897/SRE10.496**.

[25] Lin, T.-R. (2002). Experimental design and performance analysis of TiN coated carbide tool in face milling stainless steel. *Journal of Materials Processing Technology*, vol. 127, no. 1, p. 1-7, **DOI:10.1016/S0924-0136(02)00026-2**.

[26] Kıvak. T. (2014). Optimization of surface roughness and flank wear using the Taguchi method in milling of Hadfield steel with PVD and CVD coated inserts. *Measurement*, vol. 50, p. 19-28, **DOI:10.1016/j.measurement.2013.12.017**.

[27] Ozcelik, B., Bayramoglu, M. (2006). The statistical modeling of surface roughness in high-speed flat end milling. *International Journal of Machine Tools and Manufacture*, vol. 46, no. 12-13, p. 1395-1402, **DOI:10.1016/j.ijmachtools.2005.10.005**.

[28] Karakas, M.S., Acır, A., Übeyli, M., Ögel, B. (2006). Effect of cutting speed on tool performance in milling of B4Cp reinforced aluminum metal matrix composites. *Journal of Materials Processing Technology*, vol. 178, no. 1-3, p. 241-246, **DOI:10.1016/j.jmatprotec.2006.04.005**.

[29] Jayakumar, K., Mathew, J., Joseph, M.A. (2013). An investigation of cutting force and tool–work interface

temperature in milling of Al–SiCp metal matrix composite. *Proceedings of the Institution of Mechanical Engineers, Part B: Journal of Engineering Manufacture*, vol. 227, no. 3, p. 362-374, **DOI:10.1177/0954405412472887**.

[30] Montgomery, D.C. (2001). *Design and Analysis of Experiments*. 5th ed., Wiley, New York.

[31] Roy, R.K. (2001). *Design of Experiments Using the Taguchi Approach: 16 Steps to Product and Process Improvement*. John Wiley & Sons, New York.

[32] Noordin, M.Y., Venkatesh, V.C., Sharif, S., Elting, S., Abdullah, A. (2004). Application of response surface methodology in describing the performance of coated carbide tools when turning AISI 1045 steel. *Journal of Materials Processing Technology*, vol. 145, no. 1, p. 46-58, **DOI:10.1016/S0924-0136(03)00861-6**.

[33] Arumugam, S., Sriram, G., Rajmohan, T. (2014). Multi-response optimization of epoxidation process parameters of rapeseed oil using response surface methodology (RSM)-based desirability analysis. *Arabian Journal for Science and Engineering*, vol. 39, no. 3, p. 2277-2287, **DOI:10.1007/s13369-013-0789-5**.

[34] Abbas, A.T., Pimenov, D.Y., Erdakov, I.N., Mikolajczyk, T., El Danaf, E.A., Taha, M.A. (2017). Minimization of turning time for high-strength steel with a given surface roughness using the Edgeworth–Pareto optimization method. *The International Journal of Advanced Manufacturing Technology*, vol. 93, no. 5-8, p. 2375-2392, **DOI:10.1007/s00170-017-0678-2**.

[35] Abbas, A., Pimenov, D., Erdakov, I., Taha, M., El Rayes, M., Soliman, M. (2018). Artificial intelligence monitoring of hardening methods and cutting conditions and their effects on surface roughness, performance, and finish turning costs of solid-state recycled Aluminum alloy 6061 chips. *Metals*, vol. 8, no. 6, p. 394, **DOI:10.3390/met8060394**.

Strojniški vestnik - Journal of Mechanical Engineering 65(2019)6, 386-397

DOI:10.5545/sv-jme.2018.5901 Original Scientific Paper
Received for review: 2018-11-30
Received revised form: 2019-05-15
Accepted for publication: 2019-05-31

Numerical Simulation-Based Effect Characterization and Design Optimization of a Micro Cross-Flow Turbine

Endashaw T. Woldemariam – Hirpa G. Lemu*
University of Stavanger, Faculty of Science and Technology, Norway

In this era of high power demand along with a need for sustainability, small and micro-scale hydro turbines are indispensable, especially for off-grid power generation. These hydro-turbines are more appealing, particularly for small-scale enterprises, hospitals, telecommunication facilities, residential buildings, and other public institutions located in remote areas that have rich hydropower potential. Due to their simple design, manufacturability, and maintainability, micro cross-flow turbines are more feasible and applicable for power generation in undeveloped and developing countries with scattered hydropower resources. Such hydropower generation is environmentally friendly as their construction and operations have no significant effect on the surrounding ecosystem. To extract the highest possible power, however, the power generation efficiency of cross-flow turbines are is yet well optimized. In this paper, a numerical-based investigation on 3D numerical models and a design optimization study that is aimed at improving the turbine's performance has been studied and reported. A numerical simulation-based metamodel assisting optimization approach is deployed to carry out the optimization after the characterization of the design parameters, following a previous experimental study on a similar model. The benefits of the approach with regard to computational costs and outcome of the optimization are discussed. Responses from the optimized design are compared against the original design responses at different magnitudes of design parameters. Published experimental test results based on similar conditions are used to verify the models at each stage. The approach is found effective, and the optimized model shows better performance and efficiency than the original models at similar working condition.

Keywords: crossflow turbine, micro hydro turbine, numerical simulation, metamodel based optimization

Highlights

- *A numerical simulation based investigation of a 3D model of a micro cross-flow turbine is conducted.*
- *A metamodel-assisted optimization approach is deployed to carry out the design optimization.*
- *The benefits of the numerical simulation approach in terms of computational costs and the outcome of the optimization are discussed.*
- *The response of the optimized design is compared with the original design responses at different magnitudes of design parameters.*
- *The model results at each stage of the turbine are compared with similar experimental works.*

0 INTRODUCTION

In an era of increasingly growing energy demands and concern regarding the massive consumption of fossil fuel to satisfy energy needs, any alternative energy source is indispensable. Moreover, the growing concern regarding climate change has brought several nations to a common consensus to pursue cutting the amount of greenhouse gas emissions, which demands an urgent reduction of fossil-fuel consumption as a significant energy source and promoting carbon capture [1]. To balance those concerns, sustainable and renewable energy sources are more critical in this period than at any time before. Since hydropower resources are the most accessible sources of renewable energy, small and micro-scale hydropower generations are undeniably essential to contributing a considerable portion to this effort. In addition, these hydro turbines undisputedly play a significant role in providing off-grid power generation to small-scale enterprises, hospitals, telecommunications facilities, residential buildings and other public institutions located in remote areas and are more feasible particularly for developing and less developed countries. As studies by Kaunda et al. [2] and Paish [3] show, however, the benefits of the application of these kinds of turbines are not limited to developing and less-developed countries only but to some extent also for developed countries. Off-grid power generation contributes to the effort of reducing power loss in the power transmission process, most importantly, for scattered power distribution systems in rural areas. Moreover, unlike large-scale hydropower generators, small scale turbines generate power without significant impact on the ecosystem [3].

A micro-scale turbine type called a cross-flow turbine, also known as Michell-Banki's turbine, is economically efficient and simple design compared to other conventional micro-turbines. Fig. 1 illustrates such a turbine called the International Assistance Mission (IAM) [4]. Apart from its simplicity, this

*Corr. Author's Address: University of Stavanger, Faculty of Science and Technology, Norway, Hirpa.g.lemu@uis.no

turbine type incurs relatively low manufacturing, operation, and maintenance costs [5].

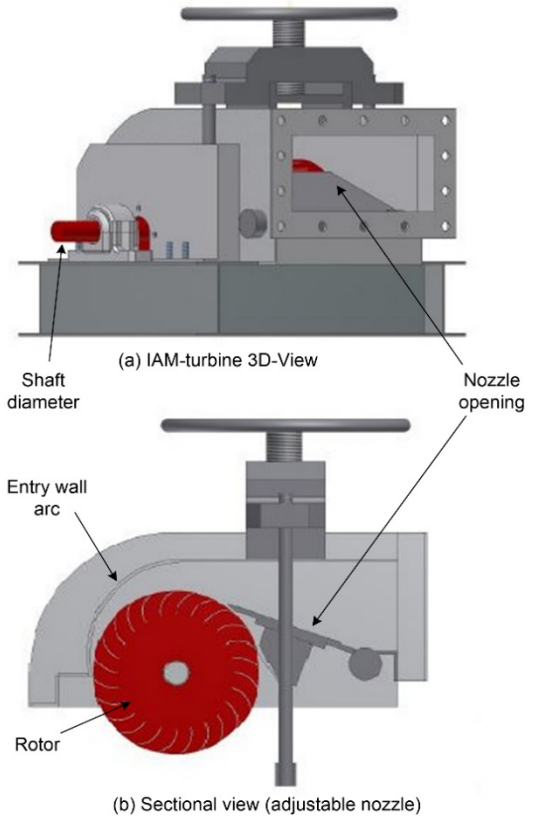

Fig. 1. *IAM turbine assembly drawing adopted from [4]; a) 3D isometric view, and b) sectional view with the adjusting part*

Moreover, its favourable run-of-the-river application and the power generation efficiency at part load conditions attract more research interest. Despite all those benefits over other conventional hydro turbines, however, the power-generating performance and efficiency of the turbine are not yet well optimized. In efficiency research on cross-flow turbines, experimental works dominate earlier studies while recent works mostly adopted numerical methods. This is partly due to the powerful and reliable computational tools and partly due to the accompanying high costs of experimental works. To improve the efficiency, for instance, Olgun [6] conducted an experimental study on effect of geometric parameters of the nozzle and the runner such as diameter ratios, throat-width ratios and gate-opening size on the efficiency and reported that micro cross-flow turbines can be operated with a wider range of gate opening compared with other turbines having maximum efficiency. Acharya et el. [7] conducted numerical research involving the modification of nozzle radius, varying the guide vane angle, and changing the number of runner blades. From this study, it has been observed that the highest efficiency of 76.6 % was obtained with 22 blades.

Similarly, Choi et al. [8] studied the efficiency and flow characteristics numerically by varying the shape of the nozzle and the runner blade. However, most of the reported theoretical studies [9] to [11] and experimental investigations [12] and [13] show massive inconsistency in the results of their efficiency computation. Most theoretical research reports, for instance, in [11], [14], and [15], show that the contribution from the second stage ranges from 18 % to 30 % of the total power generated. An overview of achieved efficiencies by different researchers in [16] show variations from 66 % to 88 %.

In cross-flow turbines, the water jet from a penstock initially passes through a nozzle, which is controlled by a valve. Once the jet exits the nozzle, it then strikes the rotor blades from the outer and inner periphery for first and second stage power generation, respectively. More details on operating principles of cross-flow turbines and the detail description of the main parts are discussed in a previous related work by the authors [17].

The main objective of this paper is to instigate a numerical simulation-based approach to the study of the effects of selected design parameters on the optimized performance, and thus improved the output of the turbine utilizing the parameters. It aims to obtain a turbine with better performance, and thus with better hydraulic efficiency.

Following this introduction section, a brief discussion of the methodology and the approaches employed are presented. Sections 2 and 3 are devoted to the theoretical power computation and numerical models, the chosen governing numerical models and their validation through sensitivity analyses. In Section 4, the optimization approach and brief comparison with other tools are discussed, followed by a discussion of the results in Section 5. Finally, conclusions are drawn in the last section.

1 METHODOLOGIES AND APPROACHES

As stated, this paper presents work carried out on a numerical simulation-based investigation and design optimization, aiming to study the effects of some essential design parameters on the performance and to narrow down the massive inconsistency of efficiency results seen in multiple studies of micro cross-flow turbines. The numerical simulation-based design optimization approach uses a metamodel assisted optimization tool to improve the performance of a

selected micro cross-flow turbine model. In a previous related work [17], a similar approach was discussed but with limited study on a 2D numerical model whose results have been published. This extended version of the work focuses on the 3D model analysis of the turbine for numerical model verification and comparison of the performance against the original model using time-dependent (transient) analyses. The numerical models and computational tools are verified using experimental test results in [4]. The thesis reported in [4] aims to study the fluid flow characteristics and measurements of the relative moment using a laboratory setup that enables collecting relative load responses on the rotor blade design (Fig. 1). The experimental test was carried out at different head and rotational speeds of the rotor. Our numerical simulation based study, however, focuses on a 5-meter net fluid head input at rotational speeds of 250 and 350 revolutions per minute [rpm] because stable experimental test results are obtained in these range of load conditions.

Table 1. *Original turbine geometric parameter values*

Parameter	Description	Value [unit]
R	Outer radius of the rotor	13.5 cm
r	Inner radius of the rotor	9.366 cm
r_c	Entry arc curvature	15.3 cm
β_1	Blade angle at rotor outer circle	30 degrees
β_2	Blade angle at rotor inner circle	90 degrees
r_s	Rotor shaft radius	2.25 cm
b	Depth (width) of the turbine	20.4 cm
N	Number of blades	24

A detailed description of the deployed numerical simulation-based metamodel-assisted optimization (NSBMAO) approach and the alleviated number of function evaluation reports are introduced in Section 4. A commercial ANSYS workbench tool [18] was interfaced with the optimization tool, which served for modelling and computational fluid dynamics (CFD) simulation in both the 2D and 3D analyses. The single objective global optimization (SOGO) algorithm of the metamodel assisted optimization tool, from Optimization Assisted System Integrated Software (OASIS) tool [19], which is designed for computationally expensive black box problems [20], is deployed to perform the optimization. In the investigations, parameters assumed appealing for the turbine performance improvement from previous studies are considered (Table 1). Two of the parameters, i.e. valve angle and the entry wall arc, are assumed to have a significant impact on the 1st stage power generation, while the rotor shaft diameter has an impact mainly at the 2nd stage.

2 THEORETICAL POWER COMPUTATION IN CROSS-FLOW TURBINES

Due to the turbine's configuration and power transfer characteristic condition inside the turbine, crossflow turbines are mostly assumed to be impulse turbines. The theoretical power conversion computation, therefore, is carried out through fluid velocity differences at the rotor's entry and exit blades using Euler's turbomachinery equations. From the given hydraulic head subject to the turbine inlet, Eq. (1), the theoretical power computation, therefore, uses the theoretical fluid jet velocities at four points, two at the first stage, and two at the second stage (Eqs. (2) to (5)).

$$V_{in} = V_1 \approx C_v \sqrt{2gH}, \tag{1}$$

$$V_{u1} = V_1 \cos\alpha_1, \tag{2}$$

$$V_{u2} = V_2 \cos\alpha_2, \tag{3}$$

$$V_{u2} = U_2 = V_{u3}, \tag{4}$$

$$V_{u4} = \varphi V_1 \cos\alpha_1 - \omega \times R(\varphi + 1). \tag{5}$$

The theoretical torque and power calculations then follow Euler's turbomachinery equations (Eqs. (6) to (9)).

$$F = \rho Q \int_2^1 dv = \rho Q(V_1 - V_2), \tag{6}$$

$$T = F \times R = \rho Q(V_1 - V_2)R, \tag{7}$$

$$P_{out} = T \times \omega, \tag{8}$$

$$P_{in} = Q(P_{r\_in} - P_{r\_out}) / \rho, \tag{9}$$

where P_{r_in} and P_{r_out} are the pressure at the inlet due to the head of the water and at the outlet of the turbine model, respectively.

Fig. 2a shows the peripheral velocities tangent to the outer and inner diameters, u_i (i = 1 to 2), the actual fluid velocities, v_j (j = 1 to 4) and the relative velocities, w_k (k = 1 to 4), corresponding to points 1 to 4 on the rotor. In addition, the diagrams in Fig. 2b describe the detail velocity components at the rotor using velocity triangles at each power generation location. Similar to most experimental studies, the theoretical studies also show massive inconsistency in the efficiency analysis studies of similar turbine types [9] to [11]. The inconsistencies raised are mainly due to the uncertainty on the fluid angles at the entry

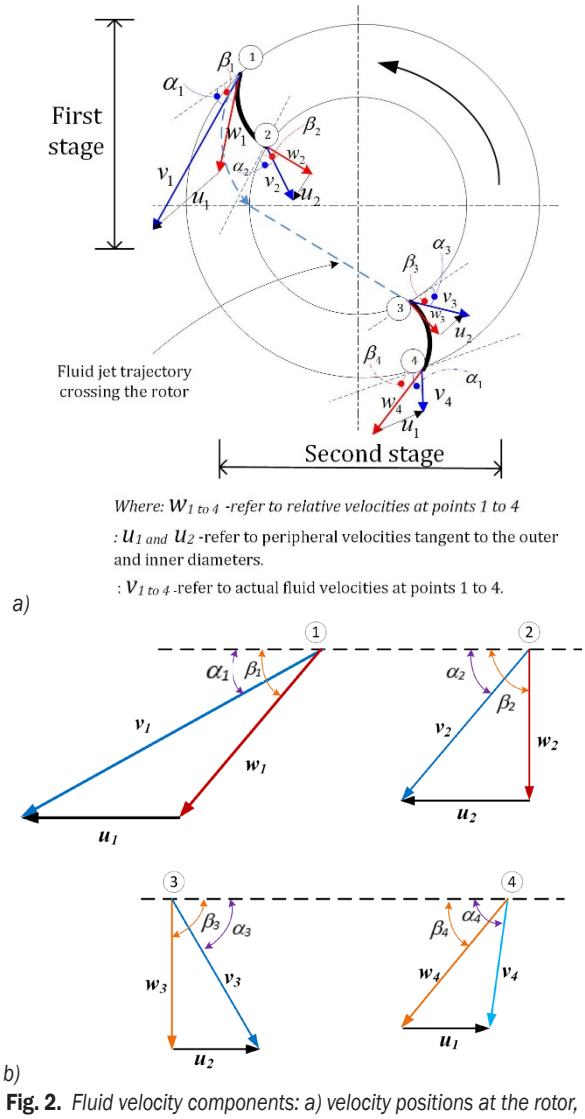

Fig. 2. *Fluid velocity components: a) velocity positions at the rotor, and b) velocity triangles at each points*

and exit of the rotor blades. In the theoretical power calculations, some studies use the entry arc curvature angle, for instance in **[21]**, but others use the nozzle valve angle **[22]** as an attack angle (location illustrated in Fig. 3 of the fluid at the entry.

3 MODEL VALIDATION & SENSETIVITY ANALYSIS

To obtain realistic responses from the numerical simulation, it is essential to validate the model grid, the numerical turbulence model, and the algorithms employed to study both the steady-state and transient analysis and the CFD simulation-based optimisation. For the analyses, 3D numerical models with one-to-one scale as the IAM turbine design, except the depth,

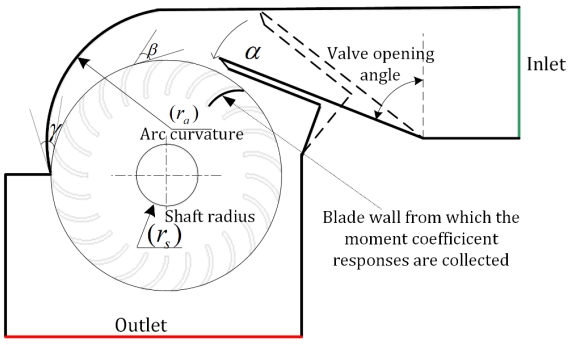

Fig. 3. *2D sketch of IAM turbine with parameters*

are utilized (Fig. 4). One section of the turbine, which is one third of the actual depth of the design, is used considering symmetry in that direction and that it could represent the problem well. Each domain of the models is divided into three zones: (1) housing, (2) rotor, and (3) stationary. The interfacing surfaces between the zones are recognized and coupled automatically in the simulation tool while generating the grid to smoothly transfer results between the moving and other zones at the interfaces. The turbulent Navier Stokes equation (Eq. (10)) is simplified in different viscous models and tested for sensitivity analysis **[18]**.

$$\frac{\partial \rho}{\partial t} + \nabla \cdot (\rho V) = S_m,$$

$$\frac{\partial \rho}{\partial t}(\rho V) + \nabla \cdot (\rho V V^T) = -\nabla P + \nabla \cdot (\bar{\bar{\tau}}) + \nabla \cdot (-\rho \overline{v^i v^{iT}}), \quad (10)$$

$$\bar{\bar{\tau}} = \mu \left[(\nabla V + \nabla V^T) - \frac{2}{3} \nabla \cdot V I \right],$$

where S_m is the source term and $\bar{\bar{\tau}}$ is the stress tensor given in Eq. (10), the term $-\rho v^i v^{iT}$ is the Reynolds stresses term, V is the velocity vector representing the sum of the average and the fluctuating components (i.e., $V = \overline{V} + v^i$), μ and I are the molecular viscosity of the fluid and the unit tensor respectively.

3.1 3D Numerical Model Grid Validation

The grid qualities of all numerical models both in the transient and steady-state analyses are controlled so that the parameters that ensure the quality fall in the acceptable range so as to obtain realistic results. Some of the important parameters considered to ensure the grid qualities are orthogonal skewness, aspect ratio and orthogonal quality of the elements in the grid domain. Table 2 shows the details of the grid node and element sizes of one of the models after the

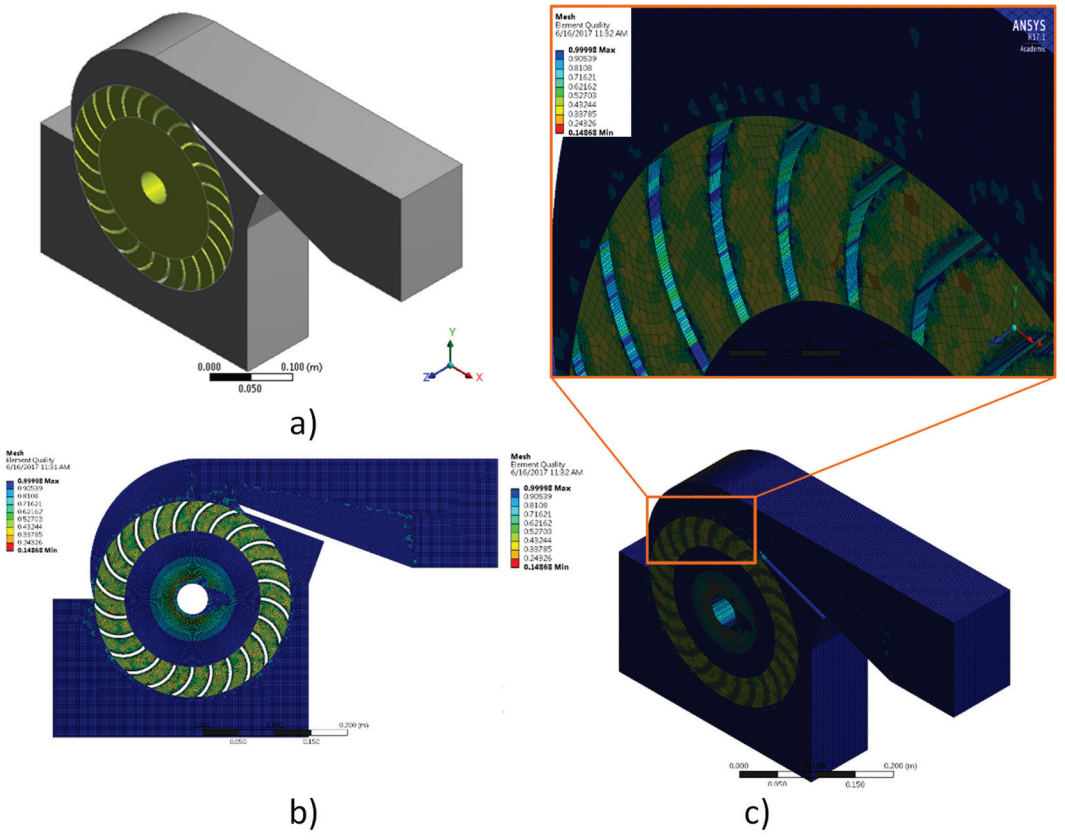

Fig. 4. *IAM cross-flow turbine 3D numerical model and mesh element quality; a) unmeshed model assembly, b) meshed model (front view), and c) meshed model with detailed view*

quality validation that is utilized in the 3D numerical analysis. The model grid qualities are also validated while comparing the trends of the numerical moment coefficient responses from one of the rotor blade's front wall against the relative moment signal from experimental test results of the sensitivity analysis in the following section. The voltage signals from the experimental tests are collected from a mechanical strain gage carefully attached to one of the front walls of the rotor's blade.

Table 2. *Mesh measurements and qualities of the 80 % opened model*

	Housing	Rotor	Stationary	Total
Nodes	633368	1967512	320251	2921131
Elements	594920	1620087	307160	2522167

Responses are collected from the gage while the model is subject to a five-metre water head, and the rotor is controlled at 350 rpm [4]. The numerical moment coefficient responses on the front face of a selected blade are collected at each time step from the transient numerical simulation. The post-processing tool of the research version solver tool used, ANSYS Fluent, computes the moment coefficients after solving the turbulent Navier Stokes equation. The moment coefficient computations use the moment response and the reference values set in the tool.

The total numerical moment response, Eq. (11), is the combined effect of both the pressure force and viscous force, Eq. (12), from the transient numerical simulation analysis result on one of the rotor's blade's wall.

$$M = \vec{r} \times \overrightarrow{F_p} + \vec{r} \times \overrightarrow{F_v}, \tag{11}$$

$$\overrightarrow{F} = \sum_{i=1}^{n} (P - P_{ref}) A \hat{n}, \tag{12}$$

where M is the total moment in [N·m] due to the pressure and viscous forces, $\overrightarrow{F_p}$ and $\overrightarrow{F_v}$ respectively. Both forces are computed based on Eq. (10). $\vec{r}$ is the moment arm from the moment centre of the wall to the rotational axis of the rotor. P and P_{ref} are the total and the reference pressures computed, respectively. A

and $\hat{n}$ are the area and the normal vector to the surface.

Moreover, to compute the hydraulic efficiency (η) of the turbine model from numerical analysis, the output hydraulic power computed from the total moment response and the rotational speed subject on the rotor. While the input power is computed from the hydraulic input head, the numerical flow rate is computed at the inlet of the turbine (Eq. (13)).

$$\eta = \frac{M \cdot \omega}{Q(P_{r\_in} - P_{r\_out})/\rho}, \tag{13}$$

where ω is the rotational speed [rad/s], Q is the mass flow rate; and ρ is the fluid density.

The noisy data collected from the transient analysis per time step at different inputs and boundary conditions are carefully filtered to obtain a smooth average graph without losing the property of the data. After various trials in the MATLAB tool, a cut-off frequency of 80 Hz with 850 Hz data sample frequency with Lowpass Filter gave us a smooth curve that better retain the characteristics of the original data (Fig. 5). Note that all graphs in the paper are generated using the MATLAB programming tool.

3.2 Sensitivity Analysis of Numerical Models for Computational Analysis

To make the sensitivity analysis and investigate the model that better represents the turbulent flow problem inside the turbine, three different well-known viscous models have been tested in the numerical computation:

1. standard *k–epsilon* ($k-\varepsilon$) with scalable wall functions for near wall treatment,
2. *k–omega* ($k-\omega$) with a shear flow correction *k*–omega option, and
3. large eddy simulation (*LES)* with WALE sub-grid-scale model for high turbulence test purposes.

In all the three model tests, the same solution algorithms are employed to solve the pressure-velocity coupling, and the momentum and turbulent kinetic energy in the spatial discretization. The sensitivity test is carried out comparing the trends of the moment coefficient responses from each numerical model against the relative moment signal from the experimental test result on a similar model design at the same valve opening, net inlet fluid head, and rotational speed.

Based on the gradient diffusion hypothesis, the $k-\varepsilon$ model relates the Reynolds stresses to the mean velocity gradients and the turbulent viscosity in solving the kinetic energy and the turbulent dissipation. This model is found to be robust, computationally cheap and widely used even though it performs poorly for complex flows that involve a strong streamline curvature, severe pressure gradient, and separation. In contrast, the $k-\omega$ model allows for better near-wall treatment and performs well in low Reynolds number flows, but it requires intense mesh resolution near walls [23] and [24]. Unlike the other two models, the LES model better allows explicitly solving large eddies and accounts for the selected small eddies using the sub-grid-scale model. It is more popular in simulating highly turbulent flows but gives only a fair enough solution near walls [25].

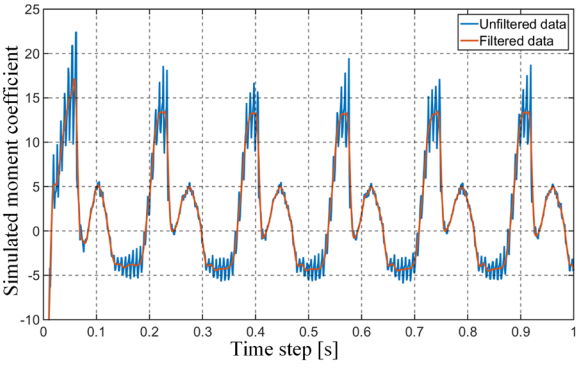

Fig. 5. *Curves from original unfiltered data and filtered data on 80 % opened valve model at 350 rpm*

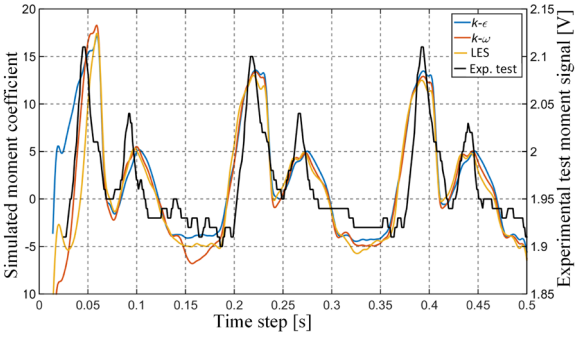

Fig. 6. *Moment coefficient responses' graph from three viscous models vs. experimental test moment signal from strain gages on a blade face*

As observed in Fig. 6, the relative moment test signal from experimental test results [4] and the numerical responses show a good agreement with regard to showing the 1st and 2nd stage power generation regions clearly. Moreover, in all cases, the average period of the responses match the experimental test with insignificant differences. Note that the magnitudes of the numerical responses are not

expected to match with the experimental test as the experimental study signal is not calibrated to give the moment response, hence the objective was to study the relative load at the two stages. However, the setup and the result were later calibrated to obtain the total torque on the rotor, as reported in [26]. In both the transient simulation and the experimental test results, the first stage of power generation has shown a better output than the second stage power output did, as was expected. Since the result from the k-ε model shows a better stable response cycle in both stages compared to the other models (Fig. 6), it is chosen to better represent the problem for further analyses.

3.3 Sensitivity Analysis of Numerical Solution Methods

In this section, two of the widely used solution schemes in CFD, the SIMPLE and the PISO algorithms, are tested. Both algorithms are fundamentally used to drive a pressure correction equation in the Pressure-Velocity Coupling scheme in solving the turbulent Navier-Stokes equation [27]. The fundamental difference between them is that PISO uses the velocity correction from adjacent cells while solving the continuity equation, whereas SIMPLE does not. Thus, SIMPLE leads to a simpler solution procedure that directly uses the pressure correction terms to the velocity correction. Even though the standard SIMPLE algorithm is initially developed for steady analysis, it can provide a realistic solution with smaller time step size in the time discretization. Thus, in both cases, a relatively smaller time step size of 0.001 is used in the transient analyses, as a compromise between the computational cost and accuracy. Second-order upwind methods are employed to solve the momentum, turbulent kinetic energy models and specific dissipation rate in the spatial discretization. Both time-discretized PISO and SIMPLE algorithms gave stable moment coefficient's response cycle and showed a good agreement with experimental test [4] with respect to relative 1st and 2nd stage cycles (Fig. 7). However, the result from the later converged faster than the former without showing a significant difference in the moment coefficient response. Thus, it is used in both the transient and steady-state analyses of the hydraulic efficiency computation.

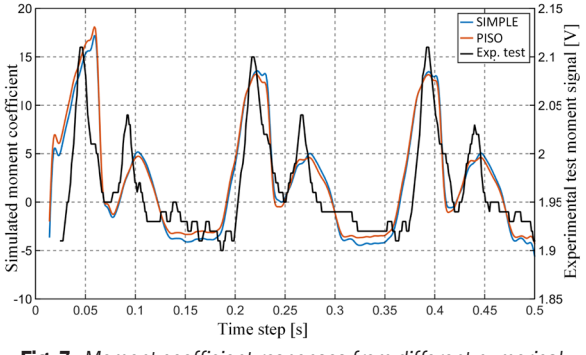

Fig. 7. *Moment coefficient responses from different numerical computational algorithms vs. experimental test moment signal*

4 ALGORITHM EMPLOYED IN THE OPTIMIZATION

In most simulation-based global optimization problems where the objective function is a result of an expensive implicit modelling and analysis tool or black-box function, applying standard optimization tools is computationally expensive and requires extensive tool-interfacing effort. Intelligent algorithms and optimization techniques are, however, being developed and employed to reduce the costs without significantly reducing the accuracy of the outcome. Thus, metamodel-assisted optimization approaches contribute significantly in this regard.

In our numerical simulation-based optimization approach, the objective function returns the average weighted total moment on the rotor walls about the Z-axis passing through the shaft centre from the implicit analysis tool (Workbench 17.1). The selected design variables and objective functions are parametrized prior to the simulation in the design modeller and ANSYS Fluent. Moreover, the design space bounds, the lower bounds (LB) and upper bounds (UB), of each of the three selected design variable are given in Table 3. The bounds are given considering the actual turbine design geometry and their validity on the numerical model.

Table 3. *Lower and Upper bounds of parameters*

Valve opening angle [deg] ([rad])		Curvature radius [cm]		Shaft radius [cm]	
LB	UB	LB	UB	LB	UB
54 (0.942)	70 (1.22)	14.5	19.0	0	4.5

The problem is formulated in a simple form as in Eq. (14). To carry out the optimization, a 2D model is utilized, aiming to further reduce the computational cost. Note that the 2D model is validated using the mesh quality control and response trends before applying the optimization.

A metamodel-assisted design optimization (MADO) approach was employed to interface with the 2D numerical model using the OASIS optimization tool, which was developed mainly to

solve computationally intensive numerical problems. From the different MADO strategies discussed in [28], this tool employs a direct sampling approach. In this approach, the metamodel is used to generate samples toward the optimum value while the metamodel is adaptively updated using each function evaluation results obtained from the black-box function. The most important benefit of the approach is that it is less dependent on the accuracy of the metamodel. The entire NSBMADO framework is shown in Fig. 8.

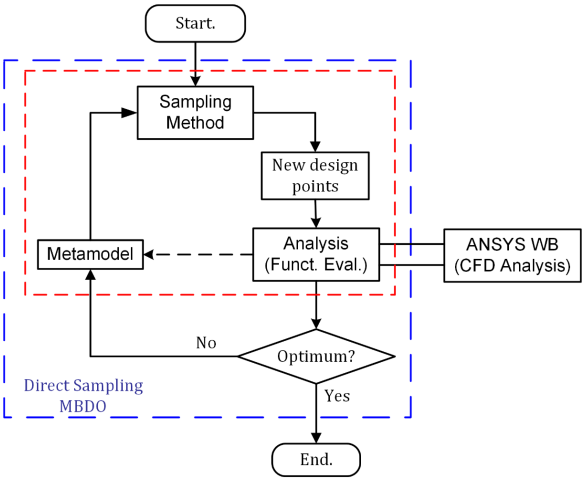

Fig. 8. *An adaptive direct sampling meta-model based design optimization framework using OASIS tool*

For this particular problem, the Single Objective Global Optimization (SOGO) algorithm is employed to solve the numerical simulation-based design optimization problem.

$$\begin{aligned} &\text{Minimize } F(x), \\ &\text{Constraints } g(x) \le 0, \\ &x \in [x_L, x_U], \end{aligned} \tag{14}$$

where the $F(x)$ is the objective function that returns the total moment on the rotor walls including the shaft wall from the simulation tool as a function of $g(x)$, where $x = [\alpha, r_a, r_s]$, is the constraint function and X_L and X_U are the lower and upper bounds of the design variables in the variable vector $\mathbf{X}$.

The optimization was run with a stopping criterion set to 80 function evaluations, which is selected based on the authors' experience on the tool after carrying out optimizations on similar models. Note that since the tool searches minimum values, the output response should be adjusted to give a negative response.

5 RESULTS AND DISCUSSION

5.1 Optimization Results

After establishing a clear interface between the MADO and the simulation tool, the optimization elapsed a total of 18 hours and 55 minutes with an average single function evaluation time of around 14 minutes. The total overhead time of the optimization tool is 2 minutes and 47 seconds. In a simple calculation deploying a regular Genetic Algorithm, the tool would take around 116 hours for 1000 iteration analyses on the same model with a simulation that takes 14 minutes on a similar machine assuming the problem converges at 500 iterations.

The convergence history of the NSBMADO optimization process per number of function evaluation is given in Fig. 9. The corresponding results of the design parameters of the optimized model are also given in Table 4. Note that the shaft size shows the stepped size of the shaft passing through the rotor, some designs have shafts to support at the sides only attached to the side plates.

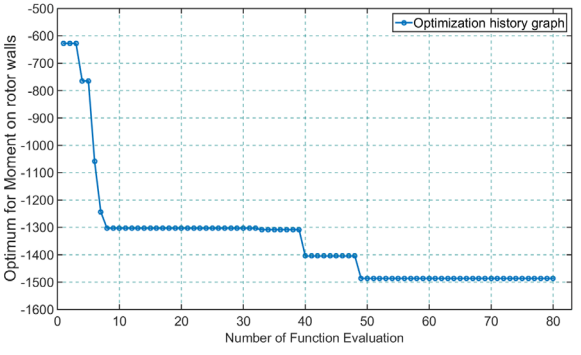

Fig. 9. *Optimum moment's convergence history from OASIS per number of function evaluation*

Table 4. *Values of optimized model parameters*

Valve angle opening [rad]	Shaft diameter [cm]	Entry arc curvature [cm]
1.217	0.136	18.28

5.2 Comparative Analysis with Optimization Results

Both transient and steady simulation on 3D models of the 80 % and 100 % opened nozzle model and model geometry from the optimization are carried out to verify the optimization results at 250 rpm and 350 rpm. The moment response graphs from the transient analyses both at 250 rpm and 350 rpm show that the

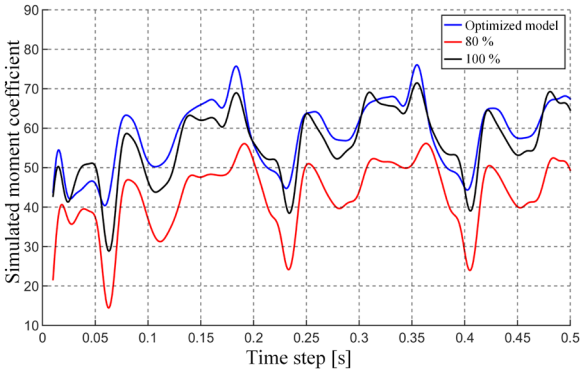

Fig. 10. *Entire rotor's moment response comparison of the optimized, 80 % and 100 % valve opening model at 350 rpm rotation of the rotor*

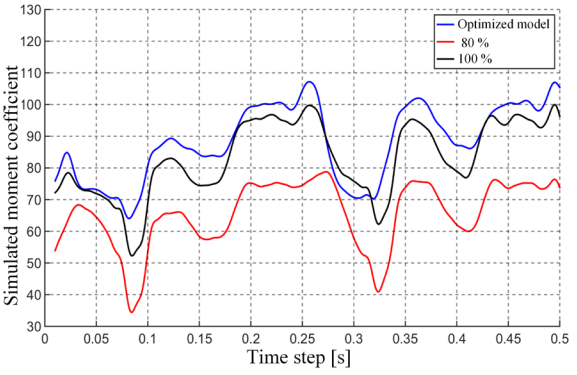

Fig. 11. *Entire rotor's torque response comparison of the optimized, 80 % and 100 % valve opening model at 250 rpm rotation of rotor*

optimum model gives better performance especially at most time steps for 250 rpm rotor speed (Figs. 10 and 11).

The velocity streamline contour diagrams in Figs. 12 and 13, particularly at 100 % opened the valve, also could give a visual understanding of how the shaft

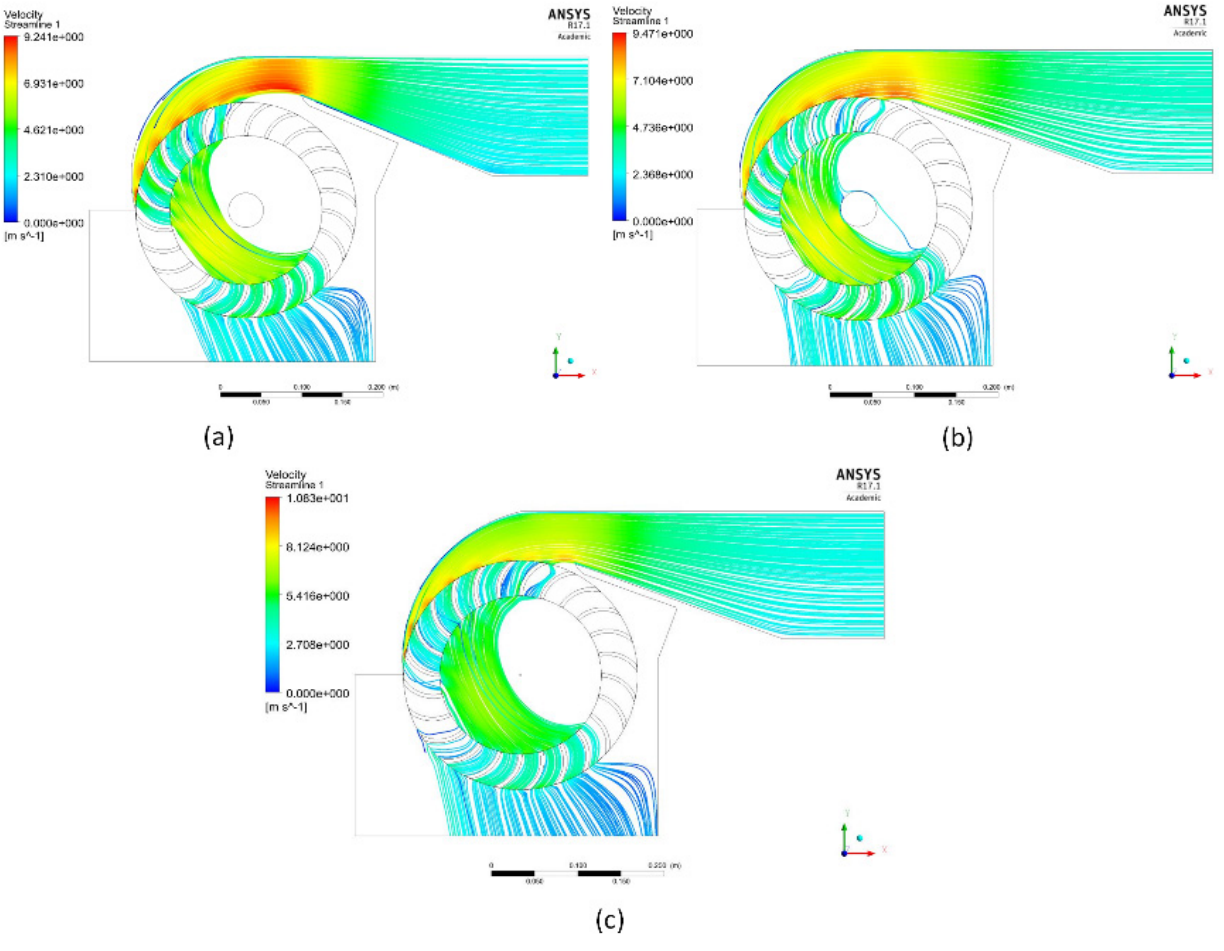

Fig. 12. *Velocity streamlines inside the turbines body at 350 rpm at: a) 80 % valve opening, b) 100 % opening, and c) optimized model*

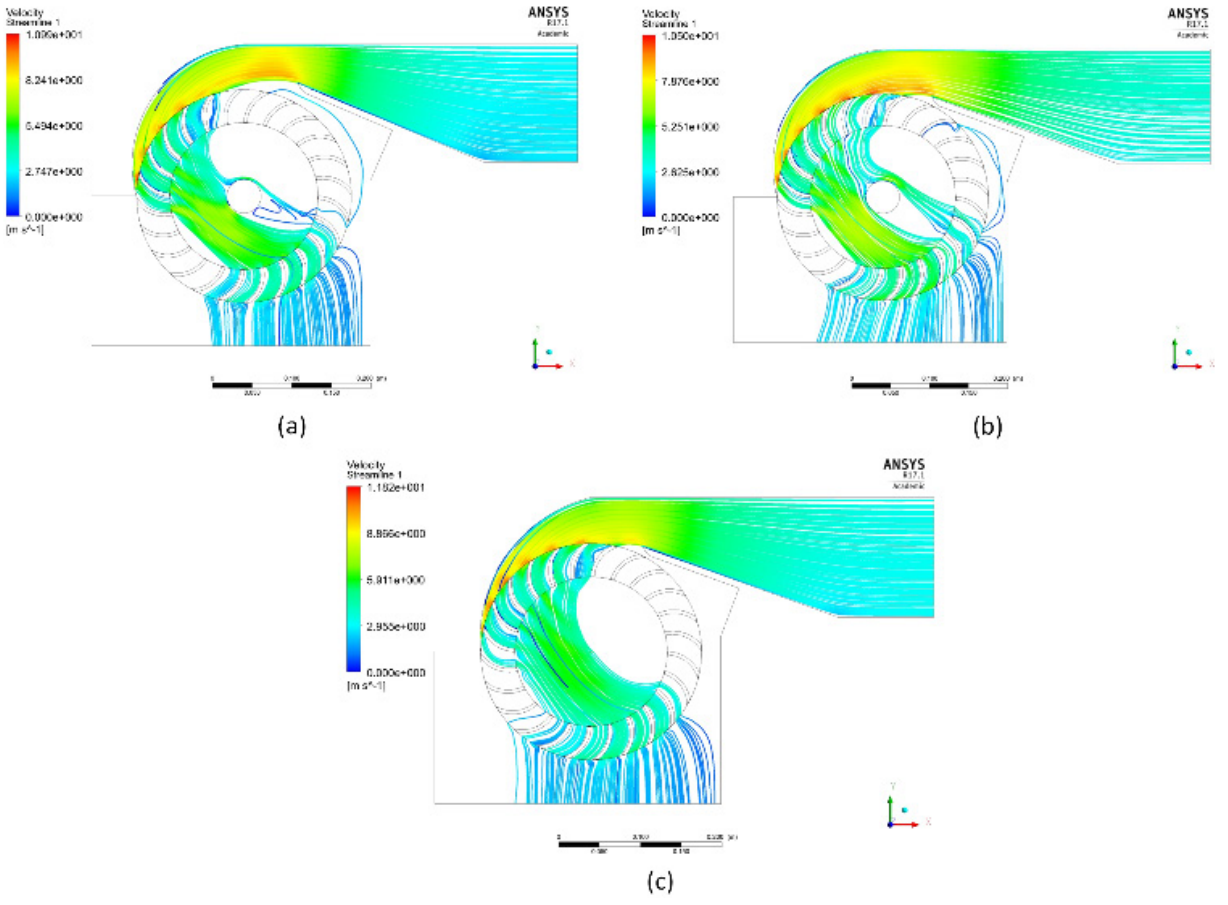

Fig. 13. *Velocity streamlines inside the turbines body at 250 rpm at: a) 80 % valve opening, b) 100 % opening, and c) optimized model*

Table 5. *Numerical steady state analysis response values and hydraulic efficiencies at 350 rpm*

No.	Nozzle opening	Pressure at outlet [N·m]	Mass flow rate [kg/s]	Moment response [N·m]	Numerical efficiency [%]
1	80 %	1541.67	37.76	21.831 (31.78 coeff)	44.60
2	100 %	1998.33	47.91	39.02 (63.70 coeff)	60.85
3	Optimized model	2112.34	44.93	37.16 (60.70 coeff)	61.80

Table 6. *Numerical steady state analysis response values and hydraulic efficiencies at 250 rpm*

No.	Nozzle valve opening	Fluid pressure at outlet [N·m]	Mass flow rate [kg/s]	Moment response [N·m]	Numerical efficiency [%]
1	80 %	878.50	36.09	37.62 (30.51 coeff)	50.62
2	100 %	635.11	34.75	46.56 (76.01 coeff)	71.52
3	Optimized Model	1834.23	49.70	55.01(89.82 coeff)	84.49

at the centre of the rotor could obstruct a significant portion of the fluid passing through the second stage power generation. This obscuring of the shaft would also produce a disturbance on the streamlines of the neighbouring fluids, which would result in more loss on the hydraulic power due to turbulence. Thus, design optimization is required.

From the steady analysis, the efficiency computation results show that the optimized model gives better efficiency than the numerical hydraulic efficiencies obtained from the original models with the valve opened 80 % and 100 % both at 250 rpm and 350 rpm (Tables 5 and 6). Unlike the reported experimental results, the original model gives

maximum numerical hydraulic efficiency at 100 % valve opening in both cases. It is discussed in the results from the experimental test in [4] that the maximum efficiency was obtained from the 80 % opening at 350 rpm.

Moreover, using the average pick values from the transient graphs for a rough estimation of the relative loads, the second stage contributes 23.42 % to 25.89 % of the total power in both cases. However, results from the experiment shown in the range from 36.4 % to 53.7 %. The later shows a massive deviation from most of the theoretical study reports on this kind of microturbine, which ranges from 26 % to 30 % only.

6 CONCLUSION

The numerical simulation based study reported in this article turns out to be effective and appealing for further study on similar turbomachinery. The separate simulation studies, both the transient and steady state, on the numerical models at different parametric values returned valid and sound results. Thus, the investigation significantly attributed in the relative load trend studies on the blades' front wall and the characterization of the flow inside the turbine. It is observed that the entry arc curvature and the nozzle opening angle played a significant role in determining the attack angle of the flow stream at the entry to the first stage. It is also observed, from the velocity streamline diagrams, in three out of four cases, that the shaft diameter obstructed the fluid flow heading to the second stage therewith increasing the turbulence, which results in a relatively lower percentage power contribution from the stage. Thus, the optimization returned a highly reduced shaft size.

The optimized design outperformed the original model at different rotational speeds and valve openings including the 80 % opening at which the experimental test result, utilized for the model validation in the text, observed to have the maximum efficiency. As a result, the overall output power and efficiency are improved with the optimized model. Meanwhile, it is studied that the percentage power generated from the second stage fall close to the range other researchers reported through theoretical analysis unlike the experimental test, whose report showed a huge deviation. Using the optimized model, the efficiency is improved by 17.88 % compared to the maximum efficiency obtained from the original model at 250 rpm. Moreover, the adaptive direct sampling metamodel assisted optimization tool deployed, unlike any other global optimization tools, highly reduced computational cost that would otherwise be incurred. The numerical simulation based analysis and optimization approach could thus be employed for further studies on the same and similar turbomachinery applications. The optimization tool, in particular, is appealing for high dimensional numerical simulation-based optimization problems.

7 NOMECLATURE

H	head of entering fluid at the inlet, [m]
ρ	density of the fluid, [kg/m^3]
C_v	constant coefficient to account loss in the nozzle
g	gravitational acceleration, [m/s^2]
V_{u1}, V_{u2}, V_{u3} and V_{u4}	peripheral velocity components at point 1, 2, 3 and 4 respectively of the rotor, [m/s]
ω	the rotational velocity of the rotor
ϕ	constant empirical coefficient that accounts loss inside rotor blade
R, r	outer and inner radiuses of rotor, [m]
Q	volume flow rate of fluid inside the turbine, [m^3/s]
F	force on blades respectively due to hydraulic power, [N]
T	torques on blades respectively due to hydraulic power, [N·m]
P_{in}, P_{out}	input and output theoretical hydraulic powers respectively, [kW]
α, β	actual and relative velocities angles from the tangents to the periphery

8 REFERENCES

[1] UNFCCC (2014). The Paris Agreement. United Nations Framework Convention on Climate Change, from *http://unfccc.int/paris_agreement/items/9444.php*, accessed on 2018-11-15.

[2] Kaunda, C.S., Kimambo, C.Z., Nielsen, T.K. (2012). Potential of small-scale hydropower for electricity generation in Sub-Saharan Africa. *ISRN Renewable Energy*, vol. 2012, art ID 132606, **DOI:10.5402/2012/132606**.

[3] Paish, O. (2002). Small hydro power: technology and current status. *Renewable and Sustainable Energy Reviews*, vol. 6, no. 6, p. 537-556, **DOI:10.1016/S1364-0321(02)00006-0**.

[4] Walseth E.C. (2009). Investigation of the Flow through the Runner of a Cross-Flow Turbine. MSc Thesis, Norwegian University of Science and Technology, Trondheim.

[5] Anagnostopoulos J.S., Papantonis D.E. (2007). Optimal sizing of a run-of-river small hydropower plant. *Energy Conversion and Management*. vol. 48, no. 10, p. 2663-2670, **DOI:10.1016/j.enconman.2007.04.016**.

[6] Olgun, H. (1998). Investigation of the performance of a cross-flow turbine. *International Journal of Energy Resources*, vol. 22, no. 11, p. 953-964, **DOI:10.1002/(SICI)1099-114X(199809)22:11<953::AID-ER418>3.0.CO;2-1**.

[7] Acharya, N.I., Kim, C.-G., Thapa, B., Lee, Y.-H. (2015). Numerical analysis and performance enhancement of a cross-flow hydro turbine. *Renewable Energy*, vol. 80, p. 819–826, **DOI:10.1016/j.renene.2015.01.064**.

[8] Choi, Y.-D., Lim, J.-I., Kim, Y.-T., Lee, Y.-H. (2008). Performance and internal flow characteristics of a cross-flow hydro turbine by the shapes of nozzle and runner blade. *Journal of Fluid Sciences and Technology*, vol. 3, no. 3, p. 398-409, **DOI:10.1299/jfst.3.398**.

[9] Durgin, W., Fay, W. (1984). Some fluid flow characteristics of a cross-flow type hydraulic turbine. *Small Hydro Power Fluid Machinery: The Winter Annual Meeting of ASME*, New Orleans, p. 77-83.

[10] Khosrowpanah, S., Fiuzat A.A., Albertson, M.L. (1988). Experimental study of cross-flow turbine. *Journal of Hydraulic Engineering*, vol. 114, no. 3, p. 299-314, **DOI:10.1061/(asce)0733-9429(1988)114:3(299)**.

[11] Andrade, J.D., Curiel, C., Kenyery, F., Aguillón, O., Vásquez, A., Asuaje, M. (2011). Numerical investigation of the internal flow in a Banki Turbine. *International Journal of Rotating Machinery*, vol. 2011, Art. ID 841214, **DOI:10.1155/2011/841214**.

[12] Aziz, N.M., Desai, V.R. (1991). An experimental study of the effect of some design parameters on cross-flow turbine efficiency. *Engineering Report*, Department of Civil Engineering, Clemson University, Clemons.

[13] Fiuzat, A.A., Akerkar, B. (1989). The use of interior guide tube in cross flow turbines. *Waterpower. ASCE*, p. 1111-1119.

[14] Balje, O. (1981). *Turbomachines- A Guide to Design, Selection, and Theory*. John Wiley & Sons, New York.

[15] Korpela, S.A. (2011). *Principles of Turbomachinery*. Wiley, Hoboken.

[16] Kaunda, C.S., Kimambo, C.Z., Nielsen, T.K. (2014). A numerical investigation of flow profile and performance of a low cost crossflow turbine. *International Journal of Energy and Environment*, vol. 5, no. 3, p. 275-296.

[17] Woldemariam, E.T., Lemu, H.G., Wang, G.G. (2017). Geometric parameters' effect characterization and design optimization of a micro scale cross-flow turbine for an improved performance. *Proceedings of the International Offshore and Polar Engineering Conference*, San Francisco.

[18] ANSYS Fluent user's Guide. (2011). from *http://148.204.81.206/Ansys/readme.html*, accessed on 2018-11-30.

[19] Empower Operation C (2016). Integrate and Optimize. Empower Operation Corp. from: *http://empoweroperations.com/en/oasis/* accessed on 2018-11-30.

[20] Cheng, G.H., Younis, A., Hajikolaei, K.H., Wang, G.G. (2015). Trust region based mode pursuing sampling method for global optimization of high dimensional design problems. *Journal of Mechanical Design*, vol. 137, no. 2, p. 021407, **DOI:10.1115/1.4029219**.

[21] Sammartano, V., Aricò, C., Carravetta, A., Fecarotta, O., Tucciarelli, T. (2013). Banki-Michell optimal design by computational fluid dynamics testing and hydrodynamic analysis. *Energies*, vol. 6, no. 5, p. 2362-2385, **DOI:10.3390/en6052362**.

[22] Sammartano, V., Filianoti, P., Morreale, G., Sinagra, M., Tucciarelli, T. (2016.) Banki-Michell micro-turbines for energy production in water distribution networks. *Proceedings of the 4th European IAHR Conference*, Liedge, **DOI:10.1201/b21902-159**.

[23] Menter, F.R. (1992). Performance of popular turbulence models for attached and separated adverse pressure gradient flows. *AIAA Journal*, vol. 30, no. 8, p. 2066-2072, **DOI:10.2514/3.11180**.

[24] Menter, F.R. (1994). Two-equation eddy-viscosity turbulence models for engineering applications. *AIAA Journal*, vol. 32, no. 8, p. 1598-1605, **DOI:10.2514/3.12149**.

[25] Kaunda, C.S. (2015). *Crossflow Turbine in Micro Hydropower Technology: Design and Performance Characterization with Respect to Internal Flow Profile*. University of Dar es Salaam, Dar es Salaam, **DOI:10.5406/illinois/9780252038792.003.0003**.

[26] Argyropoulos, C.D., Markatos, N.C. (2015). Recent advances on the numerical modelling of turbulent flows. *Applied Mathematical Modelling*, vol. 39, no. 2, p. 693-732, **DOI:10.1016/j.apm.2014.07.001**.

[27] Patankar, S.V., Spalding, D.B. (1983). A calculation procedure for heat, mass and momentum transfer in three-dimensional parabolic flows. *Numerical Prediction of Flow, Heat Transfer, Turbulence and Combustion*, p. 54-73. **DOI:10.1016/B978-0-08-030937-8.50013-1**.

[28] Wang, G.G., Shan, S. (2007). Review of metamodeling techniques in support of engineering design optimization. *Journal of Mechanical Design*, vol. 129, no. 4, p. 370-380, **DOI:10.1115/1.2429697**.

Vsebina

Strojniški vestnik - Journal of Mechanical Engineering
letnik 65, (2019), številka 6
Ljubljana, junij 2019
ISSN 0039-2480

Izhaja mesečno

Razširjeni povzetki (extended abstracts)

Strojniški vestnik - Journal of Mechanical Engineering 65(2019)6, SI 43

Prejeto v recenzijo: 2019-01-04
Prejeto popravljeno: 2019-04-14
Odobreno za objavo: 2019-05-07

Študija sledenja trajektorije goseničnega vozila na osnovi modelnega prediktivnega vodenja

Lin Zhou – Guoqiang Wang* – Kangkang Sun – Xin Li
Univerza Jilin, Šola za strojništvo in letalsko tehniko, Kitajska

V današnjem času potekajo obsežne raziskave avtonomnih vozil, ki so osredotočene predvsem na kolesna vozila, manj pa je raziskav na področju samodejne vožnje goseničnih vozil. Večina raziskav sledenja trajektorije goseničnih vozil uporablja kinematične modele ter ne upošteva delovanja motorja in elektromehanske sklopitve.

Metode modelnega prediktivnega vodenja se pogosto uporabljajo pri sledenju kolesnih vozil, manj pa je primerov uporabe pri goseničnih vozilih. V članku je predstavljen poskus uporabe metode MPC pri goseničnih vozilih in preverjanje, ali metoda dosega želene rezultate sledenja.

Namen je dodajanje elektromagnetne sklopitve goseničnega vozila v proces sledenja trajektorije. V članku je najprej postavljen kinematični model, nato pa še dinamični model vozila. Nato so dodane lastnosti motorja in je vzpostavljen model dinamike elektromehanske sklopitve.

Za preizkus učinkovitosti vodenja goseničnega vozila po metodi MPC je bilo opravljenih nekaj simulacij v okolju Simulink, vključno s sledenjem linearne in spiralne trajektorije. Poleg tega je bilo postavljeno nekaj eksperimentalne opreme in uporabljen je bil pomanjšani model goseničnega vozila za izvedbo preizkusov v realnem okolju.

Za uporabo algoritma MPC za sledenje trajektorije pri goseničnih vozilih z električnim pogonom je bil postavljen model dinamike elektromagnetne sklopitve vozila in opravljena simulacija algoritma za vodenje MPC v programski opremi za simulacije, nato pa je bilo opravljenih še nekaj eksperimentov v realnem okolju. V simulacijah sta bili upoštevani kinematika in dinamika na osnovi predlaganega algoritma vodenja, delovanje pa je bilo preverjeno za ravno in spiralno trajektorijo.

V članku je predstavljena uporaba metode MPC za vodenje goseničnih vozil z električnim pogonom po trajektoriji pri razmeroma majhnih hitrostih vozila in brez upoštevanja pojava zdrsavanja.

Metoda MPC je primerna za sledenje trajektorije pri goseničnih vozilih. Z matematičnimi izpeljavami je bilo mogoče določiti model elektromehanske sklopitve za gosenično vozilo. V nadaljnjih simulacijah in eksperimentih je bilo ugotovljeno, da lahko metoda MPC v kratkem času popravi smer vozila za odpravo trenutne napake in ohranitev trajektorije do cilja, tako pri linearni kot pri spiralni trajektoriji. Ko je vozilo na ciljni trajektoriji, se obdrži na njej.

Pri premikanju goseničnih vozil po netlakovanem vozišču in med obračanjem prihaja do zdrsov. Zdrsavanje gosenic vpliva na natančnost sledenja trajektorije, kar pa ni bil predmet obravnave tega članka. V prihodnje raziskave sledenja trajektorije bi bilo treba vključiti tudi zdrsavanje.

Poleg tega sta bili uporabljeni le razmeroma preprosti trajektoriji – ravna in spiralna. V prihodnjih raziskavah bo mogoče preveriti tudi učinkovitost vodenja pri zahtevnejših trajektorijah ter pri višjih hitrostih vozila.

Novost predstavljene študije je uvedba elektromehanske sklopitve v vodenje sledenja trajektorije ter uporaba metode MPC, ki je pogostejša pri kolesnih vozilih, pri vodenju goseničnega vozila. Na osnovi rezultatov simulacij so bili opravljeni tudi eksperimenti v realnem okolju, kar je na tem raziskovalnem področju razmeroma redko.

Rezultati predstavljene raziskave so uporabni v praksi in v znanosti ter bodo lahko pripomogli k implementaciji avtonomnih tehnologij v goseničnih vozilih.

Ključne besede: sledenje trajektorije, gosenično vozilo, modelno prediktivno vodenje, elektromehanska sklopitev, goseničar, avtonomno vozilo, strojni vid

*Naslov avtorja za dopisovanje: Univerza Jilin, Šola za strojništvo in letalsko tehniko, Kitajska, linzhou17@mails.jlu.edu.cn

Strojniški vestnik - Journal of Mechanical Engineering 65(2019)6, SI 44

Prejeto v recenzijo: 2019-01-15
Prejeto popravljeno: 2019-05-10
Odobreno za objavo: 2019-05-31

Motnje zaradi zaostalih napetosti pri laserskem spajanju s lojev nikljevih superzlitin v prahu

Özgür Poyraz[1,*] - Melih Cemal Kuşhan[2]
[1]TEI, Tusaş Engine Industries Inc., Turkey
[2]Univerza Eskişehir Osmangazi, Fakulteta za inženirstvo, Oddelek za strojništvo, Turkey

Cilj predstavljene študije je oblikovanje modela za hitre termomehanske simulacije postopka laserskega spajanja slojev praškastega materiala in izvedba eksperimentalne izdelave preizkušancev z novimi prahovi nikljevih superzlitin.

Ena od glavnih težav pri laserskem spajanju slojev praškastih materialov so zaostale napetosti in deformacije, ki se pojavijo pri segrevanju finih kovinskih prahov do tališča, ki mu sledi hitro ohlajevanje na začetno temperaturo. Deformacije zaradi zaostalih napetosti prinašajo težave z mehansko integriteto in geometrijo končnega izdelka, nad določeno mejo pa obstaja tudi tveganje prekinitev proizvodnega procesa zaradi drgnjenja med izdelkom in sistemom za nanos prahu.

Kot rešitev omenjenega problema je predlagan model za hitre termomehanske simulacije po metodi končnih elementov, ki omogoča napovedovanje deformacij zaradi preostalih napetosti. Najprej je bil za termodinamične simulacije privzet model premikajočega se toplotnega vira z Gaussovo porazdelitvijo na srednji skali za določitev vnosa energije na enoto površine. Nato je bil uporabljen ekvivalenten vnos energije v celotne plasti kot površinski vir toplote med procesom gradnje po plasteh. Upoštevano je bilo tudi dodajanje slojev s tehniko popravljanja mreže.

Predstavljeni model je bil eksperimentalno verificiran z laserskim spajanjem prahu zlitine Inconel 718, ki mu je sledila meritev izdelka z laserskim skenerjem na koordinatnem merilnem stroju. Rezultati modela deformacij so dosegli primerljivo stopnjo konvergence (< 10 %) z eksperimentalnimi rezultati. Rezultati za asimetrične preizkušance so razkrili, da imajo od geometrije izdelka odvisni učinki večji vpliv na deformacije zaradi zaostalih napetosti kot pa učinki, ki so odvisni od priprave, npr. nanašanje plasti prahu ali smer pihanja plina.

Nadaljnje študije bodo lahko usmerjene v podrobne meritve zaostalih napetosti z rentgensko difrakcijsko analizo (XRD), raziskave drugih nikljevih superzlitin kot je Hastelloy-X, parametrične simulacije reprezentativnih delov geometrije in vključitev drugih tehnik skeniranja oz. vodenja žarka, kot je vzporedno skeniranje s fiksnim kotom ali cik-cak skeniranje.

V članku je predstavljena uvedba modela za hitre termomehanske simulacije in eksperimenti s preizkušanci iz nikljevih superzlitin. Rezultati študije so nova spoznanja o deformacijah zaradi zaostalih napetosti in prispevek v bazo znanstvenega znanja z novo zasnovo preizkušancev ter metodologijo izdelave in vrednotenja za preučevanje deformacij.

Ključne besede: dodajalna tehnologija, analiza po metodi končnih elementov, Inconel 718, lasersko spajanje slojev praškastega materiala, zasnova preizkušanca, termomehanske simulacije

*Naslov avtorja za dopisovanje: TEI, Tusaş Engine Industries Inc., 26210 Eskişehir, Turčija, ozgur.poyraz@tei.com.tr

Strojniški vestnik - Journal of Mechanical Engineering 65(2019)6, SI 45

Prejeto v recenzijo: 2018-12-21
Prejeto popravljeno: 2019-05-05
Odobreno za objavo: 2019-05-10

Vpliv parametrov rezkarja na kontaktne lastnosti površin zob, obdelanih po postopku petih prehodov in po metodi Duplex Helical

Yu Zhang[1,*] – Hongzhi Yan[2] – Zhiyong Wang[1] – Qing Zhao[1]

[1] Gozdarska in tehniška univerza srednjega juga, Inštitut za sodobne tehnologije mehanskih prenosov, Kitajska
[2] Univerza srednjega juga, Državni laboratorij za visokozmogljivo kompleksno obdelavo, Kitajska

Danes se za čelno rezkanje stožčastih zobnikov s spiralnimi zobmi in hipoidnih zobnikov uporabljata dve glavni metodi. Prva je tradicionalna metoda čelnega rezkanja v petih prehodih oz. s fiksno nastavitvijo. Druga metoda se imenuje Duplex Helical in ponuja številne prednosti, kot so večja učinkovitost obdelave, nižji proizvodni stroški, višja trdnost zob in možnost suhe obdelave. Metoda Duplex Helical zato postopoma izriva obdelavo v petih prehodih. Med posplošenimi teorijami obeh metod obstajajo pomembne razlike in korelacije. Raziskovalci zobniških prenosnikov so posvetili veliko pozornosti posplošeni teoriji stožčastih zobnikov s spiralnimi zobmi in hipoidnih zobnikov, izdelanih po metodi petih prehodov. Avtorjem pa niso znane objave o posplošeni teoriji metode Duplex Helical ter o razlikah in povezavah med obema teorijama. Glavni znanstveni problemi metode Duplex Helical še niso razrešeni, kar gotovo ne koristi uveljavljanju in uporabi te metode.

Najprej so podrobno analizirana različna načela delovanja mehanizma za nagibanje rezkarja pri obeh metodah. Rezkar pri metodi Duplex Helical zahteva manjši notranji in večji zunanji radij rezila za dostop notranjega in zunanjega rezila glave do pastorka. Primerjava radijev rezkarjev pri obeh metodah pokaže, da zagotavljata pravo debelino zoba in zelo velik dolžinski profil na obeh straneh pastorka. Pri obdelavi stožčastih zobnikov s spiralnimi zobmi in hipoidnih zobnikov z istočasno spremembo kota rezila in nagiba rezkarja je mogoče zmanjšati veliko »naravno« dolžinsko profiliranje. To je tudi glavna zamisel posplošene teorije metode Duplex Helical. Primeren radij ukrivljenosti (radij ukrivljenosti je razdalja med referenčno točko na rezilu in osjo rezkarja, pravokotno na rezalni rob) v referenčni točki je mogoče spremeniti s prilagoditvijo kota rezila in nagibnih kotov rezkarja za ustrezno dolžinsko ukrivljenost na obeh straneh pastorka.

Predstavljena je primerjava in numerična analiza vpliva radija rezkarja na lastnosti ubiranja površine zoba pri obeh metodah obdelave. Vpliv kota rezila in radija rezkarja na kontaktne lastnosti površine zoba pri metodi Duplex Helical je ugodnejši kot pri postopku obdelave v petih prehodih. Parametra se zato pogosto uporabljata za optimizacijo ubiranja stožčastih zobnikov s spiralnimi zobmi in hipoidnih zobnikov.

Končno je bila opravljena tudi primerjava in numerična analiza vpliva kota rezila na lastnosti ubiranja površine zob pri obeh metodah obdelave. Rezultati analize so:

(1) Pri postopku obdelave v petih prehodih imajo velikost, položaj in smer nosilnega kontakta ter vrednost neujemanja površin zob le majhen vpliv na radij rezkarja, radij glavne osi kontaktne elipse se poveča s povečanjem radija rezkarja na dejavni strani, medtem ko je na nedejavni strani ravno nasprotno; sprememba radija manjše osi kontaktne elipse je majhna na obeh površinah.
(2) Pri metodi Duplex Helical se velikost nosilnega kontakta povečuje z večanjem radija rezkarja, hitrost sprememb na dejavni in na nedejavni strani pa je različna. Vrednost neujemanja površin zob se zmanjšuje s povečevanjem radija rezkarja.
(3) Pri enakih konstrukcijskih parametrih in parametrih rezkarjev imajo zobniki, ki so izdelani po metodi Duplex Helical, večjo upogibno trdnost zob kot zobniki, ki so izdelani po metodi petih prehodov. Razlika lahko znaša do 2,8 %.

Predstavljeno raziskovalno delo predstavlja prispevek na področju posplošene teorije metode Duplex Helical ter ima svoj teoretični in tehnični pomen kot osnova za učinkovito izbiro optimalnih nastavitev strojev za izdelavo stožčastih zobnikov s spiralnimi zobniki in hipoidnih zobnikov.

Ključne besede: metoda Duplex Helical, stožčasti zobniki s spiralnimi zobniki in hipoidni zobniki, posplošena teorija, parameter rezkarja

*Naslov avtorja za dopisovanje: Gozdarska in tehniška univerza srednjega juga, Inštitut za sodobne tehnologije mehanskih prenosov, Shaoshan South Road, No. 498, Changsha 410004, Hunan, Kitajska, zhyu@csuft.edu.cn

Strojniški vestnik - Journal of Mechanical Engineering 65(2019)6, SI 46

Prejeto v recenzijo: 2019-01-15
Prejeto popravljeno: 2019-04-13
Odobreno za objavo: 2019-05-16

Analiza vplivnih parametrov na togost podporne konstrukcije velikih radialnoaksialnih ležajev

Spasoje Trifković[1] – Nebojša Zdravković[2] – Milomir Gašić[2] – Mile Savković[2] – Goran Marković[2,*]

[1] Univerza v Vzhodnem Sarajevu, Fakulteta za strojništvo, Bosna in Hercegovina
[2] Univerza v Kragujevcu, Fakulteta za strojništvo in gradbeništvo v Kraljevu, Srbija

Pri nekaterih vrstah žerjavov in gradbenih strojev, kot so portalni žerjavi, nakladalniki in bagri, se obremenitve prenašajo na žerjavno progo oz. na podlago preko okvirja podvozja, ki je narejen iz škatlastih nosilcev. Pri takih nosilnih konstrukcijah lahko pride do privzdigovanja ene ali več podpor od žerjavne proge oz. od terena.

Izguba stika s podlago je lahko posledica neravne podlage ali pa, kar je bolj redko, napak pri izdelavi. Posledično prihaja med delom do prerazporejanja vertikalnih reakcijskih sil v podporah in do dodatnih deformacij nosilne konstrukcije. Togost velikih radioaksialnih ležajev je majhna in dodatne deformacije nosilne konstrukcije zato neposredno vplivajo na njihovo delovanje. Od togosti je odvisna tudi nagnjenost ležajnih podpornih konstrukcij k deformacijam. V strokovni literaturi ni veliko objav o vplivih geometrijskih parametrov na togost okvirjev podvozij._

V članku je opisana raziskava, ki je bila opravljena z namenom ustvarjanja analitičnega modela značilnega okvirja podvozja za bagre. Model opredeljuje teoretične odvisnosti med geometrijskimi parametri škatlastih nosilcev in velikostjo dodatnih sil v podporah okvirja, ko je ena od podpor izpostavljena določeni začetni deformaciji. Te dodatne sile so značilne za celotno togost podporne konstrukcije velikega radialnoaksialnega ležaja.

Statično nedoločena konstrukcija je bila razrešena po metodi sil. Za natančnejšo obliko zapisa vplivnih koeficientov v Maxwell-Mohrovih integralih je bila določena teoretična odvisnost med upogibnimi in torzijskimi vztrajnostnimi momenti škatlastega nosilca. Izkazalo se je, da relativna napaka aproksimacije pri večini običajnih množic geometrijskih parametrov ne presega 6,5 %. Na osnovi te aproksimacije je bil opredeljen količnik upogibne in torzijske togosti škatlastega nosilca. Na ta način je bila pridobljena množica strnjenih enačb, v katerih je ena od neznank dodatna sila v eni od podpor okvirja. Velikost dodatnih sil je v vseh podporah enaka zaradi simetrije modela. Sistem enačb je bil razrešen za različne parametre realnih konstrukcij okvirja podvozja. Podani so rezultati za različne vrednosti dolžine okvirja L (4,0 mm; 4,5 mm; 5,0 mm; 5,5 mm; 6,0 mm), razmerja med višino h in širino b škatlastega prereza $k = h/b$ (območje 1 do 3) in razmerja med upogibnim vztrajnostnim momentom vzdolžnih in prečnih nosilcev ε (1,0; 1,5; 2,0).

Po numerični analizi z orodji za iskanje krivulj najboljšega prilega v programskem paketu Matlab z zanemarjenim vplivom koeficienta ε je bila določena sprememba togosti okvirja v odvisnosti od spremembe dolžine ogrodja L in parametra k, izražena z razmerjem dodatnih sil.

Rezultati analitičnega modela so bili tudi eksperimentalno preverjeni, za izvedbo eksperimentov pa je bilo zasnovano in izdelano posebno preizkuševališče. Preizkusni modeli okvirja podvozja so bili narejeni iz kvadratnih cevi z enotno debelino stene 2,8 mm in prerezom $b \times h = 60$ mm $\times$ 60 mm oz. $b \times h = 60$ mm $\times$ 120 mm. Dimenzije preizkušenih modelov (1200 mm × 1200 mm in 1200 mm× 800 mm) so približno petkrat manjše kot pri realnih okvirjih podvozja. Relativna napaka predstavljenega analitičnega modela v primerjavi z rezultati preizkusov ne presega 6 %.

Določeno razmerje med upogibno in torzijsko togostjo škatlastih nosilcev je pomembno za nadaljnje raziskave nosilnih konstrukcij žerjavov in gradbenih strojev, saj znatno poenostavlja analitične modele. To razmerje omogoča ustvarjanje kompaktnih modelov, ki so primerni za uporabo optimizacijskih metod ter zagotavljajo rešitve s povečano upogibno in torzijsko togostjo, kakor tudi zmanjšanje mase. Ugotovljene odvisnosti med geometrijskimi parametri okvirja podvozja in njegovo togostjo omogočajo inženirjem, da poskrbijo za primerno togost konstrukcij, ki je potrebna za pravilno delovanje in dolgo življenjsko dobo velikih radialnoaksialnih ležajev.
Ključne besede: ravninski nosilni okvirji, upogibna in torzijska togost, veliki radialnoaksialni ležaji, deformacije, dodatne sile v podporah, eksperimentalna verifikacija

*Naslov avtorja za dopisovanje: Univerza v Kragujevcu, Fakulteta za strojništvo in gradbeništvo v Kraljevu, Srbija, markovic.g@mfkv.kg.ac.rs

Strojniški vestnik - Journal of Mechanical Engineering 65(2019)6, SI 47

Prejeto v recenzijo: 2019-03-02
Prejeto popravljeno: 2019-05-06
Odobreno za objavo: 2019-05-31

Študija rezalnih sil in površinske hrapavosti pri čelnem rezkanju trdega jekla SKD61

Tien Dung Hoang – Nhu-Tung Nguyen* – Đuc Quy Tran – Van Thien Nguyen
Tehniška univerza v Hanoju, Vietnam

Cilj predstavljene študije je preučitev vpliva rezalnih parametrov na površinsko hrapavost in amplitude rezalnih sil. Namen raziskave je iskanje načinov za izboljšanje kakovosti površine po čelnem rezkanju z različnimi optimizacijskimi metodami.

Rezalni parametri postopkov čelnega rezkanja, kot so rezalna hitrost, globina rezanja in podajanje, pogosto vplivajo na obdelano površino in na rezalno silo. S preučitvijo vpliva rezalnih parametrov na hrapavost površine in rezalno silo ter analizo odvisnosti med rezalno silo in hrapavostjo površine lahko izboljšamo kakovost obdelanih površin in zmanjšamo porabo moči.

Za eksperimentalno čelno rezkanje je bilo izbrano toplotno obdelano jeklo SKD61 s trdoto 46 HRC. Za tri nadzorovane dejavnike v treh ravneh (rezalna hitrost, aksialna globina rezanja in podajanje) je bilo izbrano najprimernejše ortogonalno polje L_{27} z meritvami štirih zmogljivosti – amplitude rezalnih sil v treh smereh (podajanje, normalna smer in aksialna smer) in površinske hrapavosti. Vpliv pogojev rezanja na amplitude rezalnih sil in površinsko hrapavost je bil analiziran in modeliran po metodi ANOVA. Optimalna vrednost površinske hrapavosti je bila določena po metodah Taguchi in ANOVA.

Najpomembnejši dejavnik vpliva na površinsko hrapavost je podajanje (86,594 %), najpomembnejši dejavnik vpliva na amplitudo rezalnih sil pa aksialna globina rezanja (72,891 % amplitude podajalne sile in 70,039 % amplitude normalne sile). Ostali dejavniki imajo drugačen vpliv na površinsko hrapavost in na amplitudo rezalnih sil. Amplitude rezalnih sil se povečujejo s povečevanjem aksialne globine rezanja in podajanja. Površinska hrapavost se zmanjšuje z zmanjševanjem podajanja, s povečanjem aksialne globine rezanja z 0 mm na 0,3 mm in s povečanjem rezalne hitrosti z 0 m/min na približno 130 m/min. Površinska hrapavost se povečuje s povečanjem podajanja, s povečanjem aksialne globine rezanja z 0,3 mm na 0,5 mm in s povečanjem rezalne hitrosti s 130 m/min na 200 m/min. Trend površinske hrapavosti je enak trendu amplitude rezalnih sil. Določena je bila optimalna vrednost površinske hrapavosti, ki spada med najpomembnejše vrednosti za izboljšanje kakovosti obdelanega izdelka. Najprimernejša regresijska krivulja za amplitude rezalnih sil in površinsko hrapavost je bila kvadratna krivulja s stopnjo zaupanja nad 93,74 %, kar so potrdili tudi rezultati eksperimentov. Proces optimizacije hrapavosti površine je bil opravljen po metodah Taguchi in Anova, rezultati pa so bili zelo podobni (razlika površinske hrapavosti je približno 4,58 %). Optimizirani rezultati metode ANOVA so bili boljši od rezultatov metode Taguchi. Optimalna vrednost površinske hrapavosti 0,1531 μm je bila ugotovljena pri rezalni hitrosti 113,0595 m/min, aksialni globini rezanja 0,2636 mm in vrednosti podajanja 0,05 mm/utor.

Modeli amplitude rezalnih sil in površinske hrapavosti do zdaj še niso bili uporabljeni za izboljšanje obdelanih površin in zmanjšanje rezalnih sil v CNC-sistemih za adaptivno vodenje rezkanja, zato je to ena od možnih smeri za prihodnje raziskave.

Glavni prispevki študije so: (1) vrednotenje vpliva rezalnih parametrov na hrapavost površine in amplitudo rezalnih sil, (2) vrednotenje trendov površinske hrapavosti in amplitude rezalnih sil pri spremembi rezalnih parametrov, in (3) določitev optimalnih pogojev rezanja po različnih metodah. Predstavljeni pristop je mogoče uporabiti v industriji za izboljšanje kakovosti površine trdega jekla SKD61 po čelnem rezkanju.

Ključne besede: hrapavost površine, rezalna sila, metoda Taguchi, ANOVA, SKD61, optimizacija, čelni rezkar

*Naslov avtorja za dopisovanje: Tehniška univerza v Hanoju, Number 298, Cau Dien Street, Bac Tu Liem Distric, Ha Noi City, Vietnam, tungnn@haui.edu.vn

Strojniški vestnik - Journal of Mechanical Engineering 65(2019)6, SI 48

Prejeto v recenzijo: 2018-11-30
Prejeto popravljeno: 2019-05-15
Odobreno za objavo: 2019-05-31

Karakterizacija vplivov in optimizacija konstrukcije mikroturbine s prečnim tokom na osnovi numeričnih simulacij

Endashaw T. Woldemariam – Hirpa G. Lemu
Univerza v Stavangru, Znanstvena in tehniška fakulteta, Norveška

V članku je predstavljena študija, katere cilj je bil preučitev zmogljivosti mikroturbine s prečnim tokom z numeričnimi simulacijami, izboljšanje pregleda nad vplivom izbranih konstrukcijskih parametrov na zmogljivost in optimizacija zasnove. Cilj je turbina z izboljšano zmogljivostjo kot funkcijo konstrukcijskih parametrov in posledično izboljšanim hidravličnim izkoristkom. Študija poleg tega uvaja optimizacijski okvir na osnovi numeričnih simulacij, ki bo na voljo za podobne aplikacije.

Uporabljen je bil pristop s podporo metamodela na osnovi numeričnih simulacij za optimizacijo zasnove vodne turbine s konstrukcijskimi parametri, kot so kot ventila, ukrivljenost vstopnega loka in premer osi rotorja, ki pomembno vplivajo na učinkovitost proizvodnje električne energije. Uporabljeno je bilo optimizacijsko orodje s podporo metamodela, ki je namenjeno računsko zahtevnim problemom vrste črna škatla, in sicer globalni optimizacijski algoritem z enim ciljem. Komercialno orodje ANSYS je bilo povezano z optimizacijskim orodjem za modeliranje in izvedbo simulacij računalniške dinamike fluidov (CFD) po 2D- in 3D-modelu. Odzivi optimizirane zasnove so bili primerjani z odzivi izvirne zasnove pri različnih vrednostih konstrukcijskih parametrov. Nato so bili uporabljeni objavljeni rezultati eksperimentalnih preizkusov s podobnimi začetnimi pogoji za preverjanje modelov v posameznih stopnjah turbine. Uporabljena je bila tudi analiza občutljivosti za preverjanje numeričnih rešitev CFD, oz. algoritma SIMPLE in PISO pri enačbi za popravek tlaka v sklopitvi tlak/hitrost pri reševanju Navier-Stokesovih enačb za turbulentni tok.

Ugotovljeno je bilo, da imata ukrivljenost vstopnega loka in kot odprtja šobe pomembno vlogo pri določanju kota natoka vode na vstopu v prvo stopnjo. Analiza tokovnic je tudi pokazala, da premer osi ovira tok fluida proti drugi stopnji in povečuje turbulenco, zaradi česar je prispevek moči od te stopnje razmeroma majhen. Os je bila zato med optimizacijo močno stanjšana. Časovno diskretizirani algoritmi so v analizi dali stabilen odzivni cikel za koeficient momenta in dobro ujemanje s trendom odziva eksperimentalnih preizkusov v obeh stopnjah cikla, zato so bili uporabljeni v izračunih hidravličnega izkoristka za analizo prehodnih in stacionarnih stanj. Rezultati izračunov izkoristka v analizi stacionarnega stanja so pokazali, da je izkoristek optimiziranega modela večji od numeričnih hidravličnih izkoristkov, določenih za izvirne modele pri 80 % in 100 % odprtem ventilu za izbrani vrtilni hitrosti 250 vrt./min in 350 vrt./min. S predlaganim pristopom se je močno skrajšal računski čas.

Članek obravnava numerični pristop k optimizaciji zasnove vodne turbine s prečnim tokom. Rezultati tovrstnih simulacij zahtevajo eksperimentalno verifikacijo, zato so bili kot sekundarni vir uporabljeni objavljeni rezultati eksperimentov. Čeprav so bili v simulacijah uporabljeni enaki parametri kot v eksperimentih, bo potrebna še dodatna eksperimentalna validacija in verifikacija modelov.

V predstavljeni analizi in optimizaciji turbine s prečnim tokom na osnovi numeričnih simulacij so bila kombinirana orodja za reševanje razmeroma kompleksnih problemov. Pristop se je izkazal za učinkovitega, optimizirani model pa zagotavlja boljšo zmogljivost in izkoristek kot originalni model v podobnih delovnih pogojih. Razvita metoda bo uporabna tudi za prihodnje raziskave turbostrojev s podobnimi delovnimi karakteristikami. Optimizacijsko orodje je še posebej zanimivo za optimizacijske probleme na osnovi visokodimenzijskih numeričnih simulacij, saj zmanjšuje računsko zahtevnost iskanja optimalne zasnove kompleksnih sistemov.

Ključne besede: turbina s prečnim tokom, mikro vodna turbina, numerična simulacija, optimizacija na osnovi metamodela

*Naslov avtorja za dopisovanje: Univerza v Stavangru, Znanstvena in tehniška fakulteta, Norveška, Hirpa.g.lemu@uis.no

Information for Authors

All manuscripts must be in English. Pages should be numbered sequentially. The manuscript should be composed in accordance with the Article Template given above. The maximum length of contributions is 10 pages. Longer contributions will only be accepted if authors provide juastification in a cover letter. For full instructions see the Information for Authors section on the journal's website: http://en.sv-jme.eu .

SUBMISSION:

Submission to SV-JME is made with the implicit understanding that neither the manuscript nor the essence of its content has been published previously either in whole or in part and that it is not being considered for publication elsewhere. All the listed authors should have agreed on the content and the corresponding (submitting) author is responsible for having ensured that this agreement has been reached. The acceptance of an article is based entirely on its scientific merit, as judged by peer review. Scientific articles comprising simulations only will not be accepted for publication; simulations must be accompanied by experimental results carried out to confirm or deny the accuracy of the simulation. Every manuscript submitted to the SV-JME undergoes a peer-review process.

The authors are kindly invited to submit the paper through our web site: http://ojs.sv-jme.eu. The Author is able to track the submission through the editorial process - as well as participate in the copyediting and proofreading of submissions accepted for publication - by logging in, and using the username and password provided.

SUBMISSION CONTENT:

The typical submission material consists of:

- A **manuscript** (A PDF file, with title, all authors with affiliations, abstract, keywords, highlights, inserted figures and tables and references),
- Supplementary files:
  - a **manuscript** in a WORD file format
  - a **cover letter** (please see instructions for composing the cover letter)
  - a ZIP file containing **figures** in high resolution in one of the graphical formats (please see instructions for preparing the figure files)
  - possible **appendicies** (optional), cover materials, video materials, etc.

Incomplete or improperly prepared submissions will be rejected with explanatory comments provided. In this case we will kindly ask the authors to carefully read the Information for Authors and to resubmit their manuscripts taking into consideration our comments.

COVER LETTER INSTRUCTIONS:

Please add a **cover letter** stating the following information about the submitted paper:

1. Paper **title**, list of **authors** and their **affiliations**.
2. **Type of paper**: original scientific paper (1.01), review scientific paper (1.02) or short scientific paper (1.03).
3. A **declaration** that neither the manuscript nor the essence of its content has been published in whole or in part previously and that it is not being considered for publication elsewhere.
4. State the **value of the paper** or its practical, theoretical and scientific implications. What is new in the paper with respect to the state-of-the-art in the published papers? Do not repeat the content of your abstract for this purpose.
5. We kindly ask you to suggest at least two **reviewers** for your paper and give us their names, their full affiliation and contact information, and their scientific research interest. The suggested reviewers should have at least two relevant references (with an impact factor) to the scientific field concerned; they should not be from the same country as the authors and should have no close connection with the authors.

FORMAT OF THE MANUSCRIPT:

The manuscript should be composed in accordance with the Article Template. The manuscript should be written in the following format:

- A **Title** that adequately describes the content of the manuscript.
- A list of **Authors** and their **affiliations**.
- An **Abstract** that should not exceed 250 words. The Abstract should state the principal objectives and the scope of the investigation, as well as the methodology employed. It should summarize the results and state the principal conclusions.
- 4 to 6 significant **key words** should follow the abstract to aid indexing.
- 4 to 6 **highlights;** a short collection of bullet points that convey the core findings and provide readers with a quick textual overview of the article. These four to six bullet points should describe the essence of the research (e.g. results or conclusions) and highlight what is distinctive about it.
- An **Introduction** that should provide a review of recent literature and sufficient background information to allow the results of the article to be understood and evaluated.
- A **Methods** section detailing the theoretical or experimental methods used.
- An **Experimental section** that should provide details of the experimental set-up and the methods used to obtain the results.
- A **Results** section that should clearly and concisely present the data, using figures and tables where appropriate.
- A **Discussion** section that should describe the relationships and generalizations shown by the results and discuss the significance of the results, making comparisons with previously published work. (It may be appropriate to combine the Results and Discussion sections into a single section to improve clarity.)
- A **Conclusions** section that should present one or more conclusions drawn from the results and subsequent discussion and should not duplicate the Abstract.
- **Acknowledgement** (optional) of collaboration or preparation assistance may be included. Please note the source of funding for the research.
- **Nomenclature** (optional). Papers with many symbols should have a nomenclature that defines all symbols with units, inserted above the references. If one is used, it must contain all the symbols used in the manuscript and the definitions should not be repeated in the text. In all cases, identify the symbols used if they are not widely recognized in the profession. Define acronyms in the text, not in the nomenclature.
- **References** must be cited consecutively in the text using square brackets [1] and collected together in a reference list at the end of the manuscript.
- **Appendix(-icies)** if any.

SPECIAL NOTES

Units: The SI system of units for nomenclature, symbols and abbreviations should be followed closely. Symbols for physical quantities in the text should be written in italics (e.g. *v*, *T*, *n*, etc.). Symbols for units that consist of letters should be in plain text (e.g. ms^{-1}, K, min, mm, etc.). Please also see: http://physics.nist.gov/cuu/pdf/sp811.pdf .

Abbreviations should be spelt out in full on first appearance followed by the abbreviation in parentheses, e.g. variable time geometry (VTG). The meaning of symbols and units belonging to symbols should be explained in each case or cited in a **nomenclature** section at the end of the manuscript before the References.

Figures (figures, graphs, illustrations digital images, photographs) must be cited in consecutive numerical order in the text and referred to in both the text and the captions as Fig. 1, Fig. 2, etc. Figures should be prepared without borders and on white grounding and should be sent separately in their original formats. If a figure is composed of several parts, please mark each part with a), b), c), etc. and provide an explanation for each part in Figure caption. The caption should be self-explanatory. Letters and numbers should be readable (Arial or Times New Roman, min 6 pt with equal sizes and fonts in all figures). Graphics (submitted as supplementary files) may be exported in resolution good enough for printing (min. 300 dpi) in any common format, e.g. TIFF, BMP or JPG, PDF and should be named Fig1.jpg, Fig2.tif, etc. However, graphs and line drawings should be prepared as vector images, e.g. CDR, AI. Multi-curve graphs should have individual curves marked with a symbol or otherwise provide distinguishing differences using, for example, different thicknesses or dashing.

Tables should carry separate titles and must be numbered in consecutive numerical order in the text and referred to in both the text and the captions as Table 1, Table 2, etc. In addition to the physical quantities, such as *t* (in italics), the units [s] (normal text) should be added in square brackets. Tables should not duplicate data found elsewhere in the manuscript. Tables should be prepared using a table editor and not inserted as a graphic.

REFERENCES:

A reference list must be included using the following information as a guide. Only cited text references are to be included. Each reference is to be referred to in the text by a number enclosed in a square bracket (i.e. [3] or [2] to [4] for more references; do not combine more than 3 references, explain each). No reference to the author is necessary.

References must be numbered and ordered according to where they are first mentioned in the paper, not alphabetically. All references must be complete and accurate. Please add DOI code when available. Examples follow.

Journal Papers:

Surname 1, Initials, Surname 2, Initials (year). Title. Journal, volume, number, pages, DOI code.

[1] Hackenschmidt, R., Alber-Laukant, B., Rieg, F. (2010). Simulating nonlinear materials under centrifugal forces by using intelligent cross-linked simulations. *Strojniški vestnik - Journal of Mechanical Engineering*, vol. 57, no. 7-8, p. 531-538, DOI:10.5545/sv-jme.2011.013.

Journal titles should not be abbreviated. Note that journal title is set in italics.

Books:

Surname 1, Initials, Surname 2, Initials (year). Title. Publisher, place of publication.

[2] Groover, M.P. (2007). *Fundamentals of Modern Manufacturing*. John Wiley & Sons, Hoboken.

Note that the title of the book is italicized.

Chapters in Books:

Surname 1, Initials, Surname 2, Initials (year). Chapter title. Editor(s) of book, book title. Publisher, place of publication, pages.

[3] Carbone, G., Ceccarelli, M. (2005). Legged robotic systems. Kordić, V., Lazinica, A., Merdan, M. (Eds.), Cutting Edge Robotics. Pro literatur Verlag, Mammendorf, p. 553-576.

Proceedings Papers:

Surname 1, Initials, Surname 2, Initials (year). Paper title. Proceedings title, pages.

[4] Štefanić, N., Martinčević-Mikić, S., Tošanović, N. (2009). Applied lean system in process industry. *MOTSP Conference Proceedings*, p. 422-427.

Standards:

Standard-Code (year). Title. Organisation. Place.

[5] ISO/DIS 16000-6.2:2002. *Indoor Air – Part 6: Determination of Volatile Organic Compounds in Indoor and Chamber Air by Active Sampling on TENAX TA Sorbent, Thermal Desorption and Gas Chromatography using MSD/FID.* International Organization for Standardization. Geneva.

WWW pages:

Surname, Initials or Company name. Title, from http://address, date of access.

[6] Rockwell Automation. Arena, from *http://www.arenasimulation.com*, accessed on 2009-09-07.

EXTENDED ABSTRACT:

When the paper is accepted for publishing, the authors will be requested to send an **extended abstract** (approx. one A4 page or 3500 to 4000 characters). The instruction for composing the extended abstract are published on-line: http://www.sv-jme.eu/information-for-authors/ .

COPYRIGHT:

Authors submitting a manuscript do so on the understanding that the work has not been published before, is not being considered for publication elsewhere and has been read and approved by all authors. The submission of the manuscript by the authors means that the authors automatically agree to transfer copyright to SV-JME when the manuscript is accepted for publication. All accepted manuscripts must be accompanied by a Copyright Transfer Agreement, which should be sent to the editor. The work should be original work by the authors and not be published elsewhere in any language without the written consent of the publisher. The proof will be sent to the author showing the final layout of the article. Proof correction must be minimal and executed quickly. Thus it is essential that manuscripts are accurate when submitted. Authors can track the status of their accepted articles on http://en.sv-jme.eu/.

PUBLICATION FEE:

Authors will be asked to pay a publication fee for each article prior to the article appearing in the journal. However, this fee only needs to be paid after the article has been accepted for publishing. The fee is 380 EUR (for articles with maximum of 6 pages), 470 EUR (for articles with maximum of 10 pages), plus 50 EUR for each additional page. The additional cost for a color page is 90.00 EUR. These fees do not include tax.

Strojniški vestnik -Journal of Mechanical Engineering
Aškerčeva 6, 1000 Ljubljana, Slovenia,
e-mail: info@sv-jme.eu

ISSN 0039-2480

http://www.sv-jme.eu

Contents

Papers